Title	Development of a Parallel Plate Waveguide Terahertz Spectroscopy System for the Evaluation of Ultrathin Conductive Films
Author(s)	Razanoelina, Manjakavahoaka
Citation	大阪大学, 2016, 博士論文
Version Type	VoR
URL	https://doi.org/10.18910/55963
rights	
Note	

Doctoral Dissertation

Development of a Parallel Plate Waveguide Terahertz Spectroscopy System for the Evaluation of Ultrathin Conductive Films

(導電性極薄膜評価のための平行平板導波路型テラヘルツ分光システムの開発)

Razanoelina Manjakavahoaka

January 2016

Department of Electrical, Electronic and Information Engineering
Graduate School of Engineering
Osaka University, Japan

Abstract

Development of techniques for characterization of extremely thin films is an important challenge in terahertz (THz) science and applications. Spectroscopic measurements of materials on the nanometer scale or of atomic layer thickness (2D materials) require a sufficient terahertz wave-matter interaction length, which is challenging to achieve in conventional transmission geometry. Waveguide-based THz spectroscopy offers an alternative method to overcome this problem. In this work, I investigate a new parallel-plate waveguide (PPWG) technique for measuring dielectric properties of ultrathin conductive films, in which we mount the thin-film sample at the center of the waveguide.

First, I describe in details the theory of THz wave propagation in parallel plate waveguide with conductive layer located halfway between the plates. The dispersion equations for transverse magnetic (TM) and transverse electric (TE) modes which are utilized for dielectric parameters extraction are provided. The derivation of these dispersion equations is my theoretical contribution in PPWG approach in THz time domain spectroscopy (TDS). The strategy of parameters extraction in case of single mode and multimode propagation is further discussed.

Second, I present the THz-TDS experimental system used during the realization of this work. The experimental setup is a homemade system based on transmission type THz-TDS. I discuss in details the principles and the practical applications of the main components of the system. I also describe the design of the PPWG as well as the design of the entire experimental setup.

The THz-PPWG-TDS technique is first applied to a series of gold films exhibiting a thickness dependence electromagnetic properties. This application aims to demonstrate the possibilities as well as the limitations of the technique. In contrast to other waveguide methods, our approach enables comparison of the material response with different electromagnetic field distribution without significantly changing the experimental setup. In particular, I show that the TE mode offers a better sensitivity than TM mode for characterization of 2D conductive materials.

The second application focus on probing low density carriers in a single atomic layer. Here, the sample used is graphene which is a real 2D material. I demonstrate that a carrier density of ~2 × 10^{11} cm^{-2}, which induces less than 1% absorption in conventional THz transmission spectroscopy, exhibits ~30% absorption in this waveguide geometry. The amount of absorption exponentially increases with both the sheet conductivity and the waveguide length. Therefore, the minimum detectable conductivity of this method sensitively increases by simply increasing the length of the waveguide along which the THz wave propagates, enabling us to detect low-conductivity carriers in a straightforward, macroscopic configuration that is compatible with any

standard time-domain THz spectroscopy setup. These results are promising for further studies of charge carriers in a diverse range of emerging 2D materials.

In the last application, I utilize the THz-PPWG-TDS to analyze the coupling of terahertz radiation to ultrathin electric split ring resonators which are located halfway between the waveguide plates. Observations determine that the magnetic response dominates largely over the frequency bandwidth of the system. The experimental results are confirmed by the simulations, emphasizing the importance of the proposed approach for further investigations of magnetic coupling in the metamaterials in terahertz regime.

ACKNOLEDGEMENTS

There is a long list of people that I am very grateful to have had working with and whose contributions to the realization of my PhD thesis deserve special mention.

First of all, I would like to express my full gratitude to my supervisor, Professor Masayoshi Tonouchi at Institute of Laser Engineering, Osaka University for accepting me to be a PhD student in his laboratory. I am extremely thankful to have been introduced in community of terahertz research by a person who had continuously supported and advised me throughout my PhD work. His invaluable encouragement and intellectual support have contributed, in important part, the completion of this work.

I am very thankful to Professor Toshimichi Ito at Department of Electrical, Electronic and Information Engineering, Osaka University, for his guidance, important advices and suggestions to this thesis.

I would like to express my gratitude to Professor Yusuke Mori, Professor Mitsuhiro Katayama, Professor Tetsuya Yagi, Professor Masanori Ozaki, Professor Toshiaki Suhara, Professor Masahiko Kondow, Professor Nobuya Mori, Professor Noriaki Miyanaga and Professor Hiroaki Nishimura for their valuable instructions on my researches.

I gratefully acknowledge Associate Professor Hironaru Murakami for his exceptional help, support and advices from the beginning of this work. I am especially grateful for his guidance about the waveguide design and fabrication from the very early stage of this research. I would like to express my special thanks to him for all the contributions he had been provided to this thesis.

I am also very grateful to Associate Professor Iwao Kawayama for his incessant support, valuable advices and suggestions. I am honored to have been under his supervision during the last three years of my PhD research and one year as research student.

I would like to express my full gratitude to Prof. Daniel Mittleman at School of Engineering, Brown University for his extraordinary guidance and very rich discussion about THz parallel plate waveguides. He had exceptionally enriched my intellectual development by introducing me to the methodological ideas of my research.

I am very thankful to Professor Junichiro at Department of Electrical and Computer Engineering, Rice University and at Institute of Laser Engineering, Osaka University for his precious

contribution to my understanding of two – dimensional materials. I am very lucky and also much honored to closely work with him.

I address special thanks to Ryuhei Kinjo and Kazuhisa Takayama, former members of Tonouchi Laboratory for their precious contributions in experiments. I am very grateful for their unprecedented support, without which this thesis would never have come to be completed.

I would like to express a special word of thanks to all members of Tonouchi laboratory for their kindly help and assistance.

Finally, I am fully grateful to my family for their constant and precious support.

TABLE OF CONTENTS

Chapter 1. **INTRODUCTION**

1.1 MOTIVATION

Characterization of the electromagnetic properties of thin films has been an important topic in spectroscopy for a long time. In recent years, this has become even more relevant with the growing interest in two-dimensional materials including graphene, molybdenum disulfide (MoS_2), Hexagonal boron nitride (hBN), single layer black phosphorous (BP), transition metal dichalcogenides (e.g, WSe) and other nanosheet materials [1– 3]. In the terahertz (THz) range, such materials have been recognized as important building blocks for future optoelectronic devices [4, 5]. However, characterizing such extremely thin films using conventional THz spectroscopy is often challenging for several reasons. First and most obvious reason, the extremely thin film offers a very limited interaction length with THz waves in the conventional normal-incidence transmission geometry. As a result, only a very small, essentially unmeasurable change is induced by material. In this work, this challenge is our main motivation for developing an alternative approach to characterize the electromagnetic properties of such thin materials. Second, fabricating films with atomic-scale uniformity over an area larger than the diffraction-limited focal spot of THz beam is very challenging in many cases [6].

Historically, the main efforts in THz technology have been focused in the development of THz pulse generation, THz detection and the spectroscopic applications. The progress of THz emitters and detectors have been simultaneously accompanied by the development of ultrafast laser technology and the state - of - the art for semiconductors devices. It is common use to situate the THz frequency range between 100 GHz to 30 THz [4]. In terms of photon energy (or wavelength), THz is roughly located between 0.4 meV to 124 meV (10 μm – 3 mm). Another widely accepted definition of THz radiation is also the “bridge” between microwave and optical radiation. The THz frequency range has long been considered as a “gap” since generation and detection technique of the electromagnetic radiation within this spectrum were less available, or at least less practical, until early 70’s [5]. Since then, THz technology has become to be known as an outstanding progress technology enabling breakthrough in fields of telecommunications [6], imaging [7], defense and security [8], etc.

Amongst variety of applications, THz time-domain spectroscopy is of utmost important. THz radiation can probe systems having characteristic life time of picosecond order or low energetic transition [9] including semiconductors [10], strong correlated electrons systems [11], biological molecules [12], nanostructured system [13] and a vast range of materials. Pioneered by Grischkowsky et *al*. [14], THz-TDS is basically a contactless characterization method utilizing a coherent detection technique. In frequency domain, THz-TDS is a phase resolved measurement of the complex - valued transmission. This technique allows detecting the amplitude and phase of the transmitted (or reflected) THz electric field. The real and imaginary part of the dielectric constant of the sample under analysis can be extracted directly without using Kramers -Kronig relation. Additionally, one of the merits of THz TDS is the high rejection noise efficiency that leads to a high sensitive system. For example, the signal to noise ratio (SNR) of an optimized experimental THz-TDS setup can be more than 10^4. This value was obtained at the spectrum peak of a system using a gated photoconductive antenna detector and free space electro-optic sampling detection scheme [15].

THz-TDS is an excellent tool to rapidly, non-destructively and sensitively elucidate electronic properties of materials. It is particularly efficient for characterization of materials with thickness eventually comparable or more than the operating THz wavelength (1THz = 300 μm). In conventional or standard THz-TDS system, one usually operate with the transmission geometry. Then, with relatively thick materials, the extraction of optical constant is easy, since: (*i*) the material response can be distinguished unambiguously with respect to any reference; (*ii*) THz-TDS enables the possibility of eliminating Fabry-Perot reflections which is not feasible with incoherent technique. These extraordinary capabilities are also associated with the limitations of the technique. When the samples thickness is less, even far less than the wavelength, the conventional approach is less valuable. The change in absorption of THz radiation travelling through a sample of thickness L takes the form exp ($-\alpha_S L$), where α_S is the absorption coefficient. If it is assumed that the sample has low absorption and moreover L is very small, the reference and the sample signal tend to overlap (exp ($-\alpha_S L$) $\rightarrow$ 1), and the optical parameters extraction become very challenging. In this particular case, the technique is mainly limited by the SNR of the experimental setup. If the change imposed by the sample is below the SNR achievable in experiment, the conventional technique is no longer reliable. Withayachumnankul et *al* have quantitatively studied the lower bound of common material thickness which can be characterized in transmission – type THz-TDS [16, 17]. The determination of the minimum thickness is based on the standard deviation of the phase of the reference spectrum or/and the standard deviation of the amplitude spectrum. For example, the minimum thickness for photoresist is 0.61 μm if the calculation is performed with the standard deviation of the phase while this thickness increases to 1.15 μm with the standard deviation of amplitude calculation [17].

The new emerging classes of two – dimensional materials and heterostructures are a part of samples which are challenging to characterize with conventional THz-TDS. However, such new materials exhibit unconventional electronic properties and offer new possibilities in many field of technology. Graphene is one famous example of real 2D-material with its zero gap band structure at the Dirac points [18]. Metallic nanostructures also host different carrier transport compared to their counterpart [19]. Transition metal dichalcogenide MoS_2 turns out to be direct band gap semiconductor in its 2D form, in contrast to bulk MoS_2 which is an indirect band gap semiconductor [20]. Many examples of 2D materials or ultrathin film with their properties and applications can be found in literatures [21]. However, the few cases above- mentioned illustrate the importance of such materials for fundamental sciences and applications in the near future. The common factor which characterizes these ultrathin materials is their dimensions or their thickness. Most of newly discovered or fabricated 2D materials are atomic thick layer or roughly less than tens of nanometer. The thickness of such samples is at least four orders of magnitude less than the wavelength of the THz wave (which justify the designation of “2D” or “ultrathin”). Then, the aforementioned drawbacks of the conventional THz-TDS become much dramatic for characterization of ultrathin materials. Here, the most dominant criterions which limit the conventional method are:

- Extreme subwavelength thickness: the interaction path of THz radiation – materials is extremely short. Then, the change induced by the sample is not measurable.
- Low conductivity: the absorption coefficient is very small. As a result, the investigation on the carrier dynamics of the materials is further challenging since the conventional approach does not provide accurate parameters.

As an example, Fig. 1.1 shows the transmittance of graphene on silicon substrate measured by transmission geometry THz-TDS. The reference is the transmitted THz pulse through bare silicon and the sample is graphene on silicon. The error bars indicate that the amplitude of the transmission fluctuates around the value 0.97. In other words, the absorption of the material is very weak. Therefore, spectroscopic information extracted from this measurement is not relevant.

In light of the foregoing, the challenge which mainly motivate us is to seek for a new strategy to overcome the limitations of conventional method for 2D and ultrathin conductive materials characterization. The work presented here aims to be an alternative or eventually a complementary method when the standard THz-TDS fails or tends to be a hard task for proper characterization. In this context, we intend to develop an approach which maintains the advantages of THz-TDS but also which requires some conditions such as:

- High sensitivity: The method should provide enough SNR to distinguish the THz response of the ultrathin conductive materials with respect to the reference.
- Compatibility with any standard THz-TDS system : the method should be appropriate or could be adapted to any conventional THz-TDS
- Nondestructive method: All external factors which influence the inherent properties of the samples under investigations should be avoided.
- Proper complex parameters extraction: The parameters extraction formalism should enable obtaining optical constants in a straightforward manner.

All of these requirements will be addressed along this work with concrete example of applications.

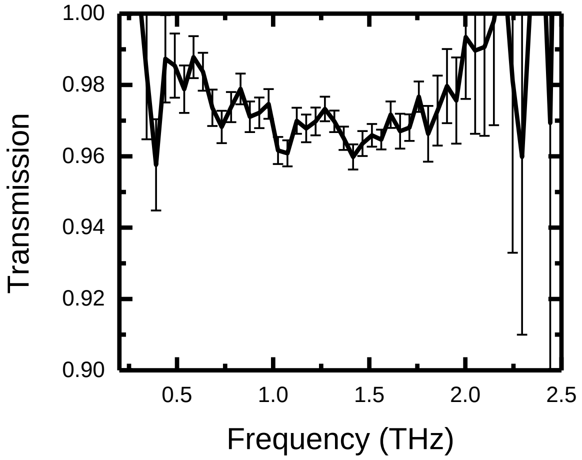

Fig. 1.1 Transmission amplitude of graphene on silicon substrate with conventional THz TDS. The mean value of the transmission is fluctuating around 0.97.

1.2 ALTERNATIVE AND OBJECTIVE OF THE WORK

Owing to these limitations factors, it is obvious that the characterization of ultrathin conductive materials requires high sensitivity techniques in order to provide reliable information which reveals the basic characteristics of the sample. Various alternative approaches have been demonstrated for the study of thin films using THz-TDS. These include attenuated total internal reflection (ATR) spectroscopy [22] and time domain measurement of surface plasmon polaritons at metal-dielectric interfaces[23]. Both methods involve planar geometry where the THz wave propagates in plane of the materials surface. Pioneered by Tanaka et *al.* of Kyoto University, time domain ATR spectroscopy is based on the interaction of the sample with the THz evanescent wave of a coupling prism. Fig. 1.2 shows a schematic view of the main part of the system reproduced from Ref [22]. In this early work, dielectric constant of a 22 μm-thick n-type (100)

InAs crystal was successfully extracted in the wavelength region from 1 THz to 2.5 THz. Similar concept have been also employed in [23] by making use of surface plasmon polaritons propagation on a metallic film coated by dielectric thin material. In contrast to ATR spectroscopy, the THz input and output coupling are performed by razors blade placed directly above the metallic film. The main disadvantage of both methods is the efficiency of free space THz radiations coupling to the samples. For example, it has been reported that the maximum coupling (including input and output coupling) efficiency for ATR is less than 3.5 %. Furthermore, to the best of my knowledge, both techniques were not applied to ultrathin or 2D materials characterization. However, these works have already included the general concept for overcoming the limitation of conventional THz-TDS. Propagation of THz wave (evanescent or guided) along the materials surface yields a longer interaction path.

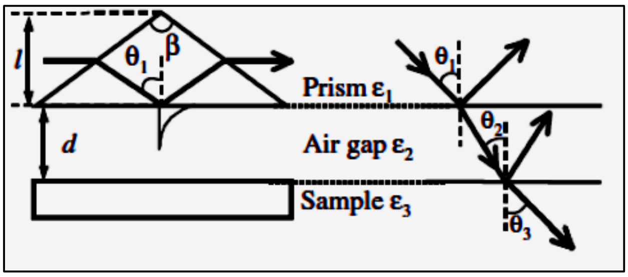

Fig. 1.2 Schematic diagram of time domain attenuated reflection spectroscopy. The THz wave is coming from the left to the right of the image. Fig. reproduced from Ref .[22]

One approach of note is the use of parallel plate waveguide (PPWG)-based spectroscopy pioneered by Grischkowsky and co-workers [24, 25]. Here, a thin dielectric polycrystalline solid is deposited on one plate of metal parallel-plate waveguide (PPWG), providing a long interaction length and therefore high sensitivity to, e.g., vibrational absorption bands in polycrystalline films [26]. Fig. 1.3 reproduces a typical THz-PPWG-TDS. The THz radiation is coupled to the PPWG with hyperhemispherical lens resulting to a coupling efficiency about 20%. In most cases, the PPWG operates at transverse electromagnetic mode which is the fundamental propagating mode of waveguide. This mode is free of dispersion and thus provides a broadband characterization. One disadvantage of this approach is that the sensitivity depends on the thickness of the thin layer relative to waveguide plate spacing, so a very thin (e.g., less than 10 nm) layer would give rise to a tiny signal [27]. A more compelling problem is that the technique is unsuitable to the study of conductive layers, since the thin sample concerned becomes essentially indistinguishable from the metal substrate.

The objective of this work is to develop a new waveguide-based THz spectroscopy approach which maintains the advantage of long interaction length between the thin film and the propagating THz wave, but which is suitable for conducting films. We still rely on the PPWG, but in our approach, the ultrathin conductive layer is situated half-way between the two metal waveguide plates, rather than in contact with one of them. In the earlier approach, the studies all made use of lowest-order transverse magnetic mode of the waveguide, since the transverse-electric (TE) mode amplitude vanishes at the metal plate surfaces (which eliminates the interaction with the sample). However, recent work has shown that TE modes can also prove useful for highly sensitive waveguide-based sensing [28, 29]. In this work, I compare the response for both transverse-magnetic and transverse-electric excitation of the waveguide. I investigate the sensitivity of our approach, and develop a new formalism for extracting quantitative dielectric parameters of the thin film from our experimental measurements.

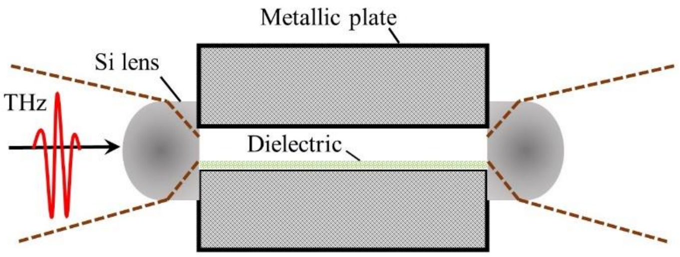

Fig. 1.3 Standard use of PPWG in THz-TDS. The dielectric sample is drop casted directly to the bottom plate of the waveguide. The analysis is performed with TEM mode.

In few words, the advantages of our PPWG based approach can be summarized as follow: (i) long path interaction leading to a sensitivity improvement; (ii) characterization of 2D conductive materials with different electromagnetic polarization by making use of waveguide modes: transverse magnetic and transverse electric modes; (iii) compatibility with any standard THz-TDS system.

This work is divided as follows:

- Chapter 2 reviews the basics of thin film characterization by conventional transmission THz TDS system. The general concept and parameters extractions will be presented. The chapter starts with thick film analysis to ultrathin conductive layer characterization.
- Chapter 3 develops the theoretical basis of our PPWG – based spectroscopy approach. In the first part, we review the basic theory framework of wave guiding in PPWG device. We extend the theory to ultrathin conductive films located halfway between the PPWG. Details of the derivation of the characteristic equations will be shown. The parameters extraction is based on these characteristic equations. Single mode and multimode analysis

are presented. The last part of this chapter is focused on the practical aspect of parameters extraction.

- Chapter 4 describes the experimental system we have used during this work. Detailed explanations of generating, detecting and reshaping THz beam are provided. The experimental setup is a modification of standard THz-TDS by incorporating PPWG.
- Chapter 5 is focused on the applications of the method. The first application is performed with gold ultrathin film. Here I demonstrate the validity of our approach by investigating on the insulator metal transition state of the gold. The second application report the primary advantage of using PPWG method on low carrier density graphene analysis. In the last part of the application, we investigate on the THz magnetic response of metamaterials. This application is an additional demonstration of the capability of THz-PPWG.
- Chapter 6 concludes this work by reviewing the main finding. Here, I emphasize the importance of the work. Some perspectives and extension of the work are also provided.

REFERENCES:

[1] L. Ren, Q. Zhang, J. Yao, Z. Sun, R. Kaneko, Z. Yan, S. Nanot, Z. Jin, I. Kawayama, M. Tonouchi, J. M. Tour, and J. Kono, “Terahertz and infrared spectroscopy of gated large-area graphene.,” *Nano Lett.*, vol. 12, no. 7, pp. 3711–5, 2012.

[2] S. Ge, X. Liu, X. Qiao, Q. Wang, Z. Xu, J. Qiu, P.-H. Tan, J. Zhao, and D. Sun, “Coherent longitudinal acoustic phonon approaching THz frequency in multilayer molybdenum disulphide.,” *Sci. Rep.*, vol. 4, p. 5722, 2014.

[3] S. Z. Butler, S. M. Hollen, L. Cao, Y. Cui, J. A. Gupta, H. R. Gutiérrez, T. F. Heinz, S. S. Hong, J. Huang, A. F. Ismach, E. Johnston-Halperin, M. Kuno, V. V Plashnitsa, R. D. Robinson, R. S. Ruoff, S. Salahuddin, J. Shan, L. Shi, M. G. Spencer, M. Terrones, W. Windl, and J. E. Goldberger, “Progress, challenges, and opportunities in two-dimensional materials beyond graphene.,” *ACS Nano*, vol. 7, no. 4, pp. 2898–926, 2013.

[4] M. Tonouchi, “Cutting-edge terahertz technology,” *Nat. Photonics*, vol. 1, pp. 97–105, 2007.

[5] D. M. Mittleman, "*Sensing with Terahertz Radiation*," Springer series in optical sciences 2003.

[6] N. J. Karl, R. W. Mckinney, Y. Monnai, R. Mendis, and D. M. Mittleman, “Frequency-division multiplexing in the terahertz range using a leaky-wave antenna,” *Nat Photonics*, vol. 9, pp. 717 - 720,. 2015.

[7] X. C. Zhang, “Terahertz wave imaging: horizons and hurdles.,” *Phys. Med. Biol.*, vol. 47, no. 21, pp. 3667–3677, 2002.

[8] K. Kawase, Y. Ogawa, Y. Watanabe, and H. Inoue, “Non-destructive terahertz imaging of illicit drugs using spectral fingerprints,” *Opt. Express*, vol. 11, no. 20, pp. 2549–2554, 2003.

[9] P. Uhd Jepsen, D. G. Cooke, and M. Koch, “Terahertz spectroscopy and imaging – Modern techniques and applications,” *Laser Photonics Rev.*, vol. 5, no. 1, pp. 124–166, 2011.

[10] T.-I. Jeon and D. Grischkowsky, “Nature of Conduction in Doped Silicon,” *Phys. Rev. Lett.*, vol. 78, pp. 1106–1109, 1997.

[11] N. Kida, H. Murakami, and M. Tonouchi, “Terahertz optics in strongly correlated electron systems,” in *Terahertz Optoelectronics*, vol. 97, 2005, pp. 271–330.

[12] M. Nagai, H. Yada, T. Arikawa, and K. Tanaka, “Terahertz time-domain attenuated total reflection spectroscopy in water and biological solution,” *Int. J. Infrared Millimeter Waves*, vol. 27, no. 4, pp. 505–515, 2006.

[13] J. Lloyd-Hughes and T. Jeon, “A review of the terahertz conductivity of bulk and nano-

materials," *J. Infrared, Millimeter, Terahertz Waves,* vol. 33, no. 9, pp. 871 - 925, 2012.

[14] M. Van Exter, C. Fattinger, and D. Grischkowsky, "Terahertz time-domain spectroscopy of water vapor," *Opt. Lett.*, vol. 14, no. 20, p. 1128, 1989.

[15] Y. Cai, I. Brener, J. Lopata, J. Wynn, L. Pfeiffer, J. B. Stark, Q. Wu, X. C. Zhang, and J. F. Federici, "Coherent terahertz radiation detection: Direct comparison between free-space electro-optic sampling and antenna detection," *Appl. Phys. Lett.*, vol. 73, no. 4, p. 444, 1998.

[16] J. F. O'Hara, W. Withayachumnankul, and I. Al-Naib, "A review on thin-film sensing with terahertz waves," *J. Infrared, Millimeter, Terahertz Waves*, vol. 33, pp. 245–291, 2012.

[17] W. Withayachumnankul, "Limitation in thin-film detection with transmission-mode terahertz time-domain spectroscopy," *Opt. Express,* no 22, pp 972 - 986, 2014.

[18] K. S. Novoselov, A. K. Geim, S. V Morozov, D. Jiang, Y. Zhang, S. V Dubonos, I. V Grigorieva, A. A. Firsov, "Electric Field Effect in Atomically Thin Carbon Films," *Science.*, vol. 306, no. 5696, pp. 666–669, 2004.

[19] M. Walther, D. G. Cooke, C. Sherstan, M. Hajar, M. R. Freeman, and F. a. Hegmann, "Terahertz conductivity of thin gold films at the metal-insulator percolation transition," *Phys. Rev. B - Condens. Matter Mater. Phys.*, vol. 76, no. 12, pp. 1–9, 2007.

[20] M. Chhowalla, H. S. Shin, G. Eda, L.-J. Li, K. P. Loh, and H. Zhang, "The chemistry of two-dimensional layered transition metal dichalcogenide nanosheets," *Nat. Chem.*, vol. 5, no. 4, pp. 263–275, 2013.

[21] F. Xia, H. Wang, D. Xiao, M. Dubey, and A. Ramasubramaniam, "Two-dimensional material nanophotonics," *Nat. Photonics*, vol. 8, no. 12, pp. 899–907, 2014.

[22] H. Hirori, K. Yamashita, M. Nagai, and K. Tanaka, "Attenuated Total Reflection Spectroscopy in Time Domain Using Terahertz Coherent Pulses," *Jpn. J. Appl. Phys.*, vol. 43, no. No. 10A, pp. L1287–L1289, 2004.

[23] J. Saxler, J. Gómez Rivas, C. Janke, H. P. M. Pellemans, P. Haring Bolívar, H. Kurz, and P. Bolívar, "Time-domain measurements of surface plasmon polaritons in the terahertz frequency range," *Phys. Rev. B*, vol. 69, no. 15, p. 155427, 2004.

[24] J. S. Melinger, N. Laman, S. S. Harsha, and D. Grischkowsky, "Line narrowing of terahertz vibrational modes for organic thin polycrystalline films within a parallel plate waveguide," *Appl. Phys. Lett.*, vol. 89, no. 25, p. 251110, 2006.

[25] G. Gallot, G. Gallot, S. P. Jamison, S. P. Jamison, R. W. Mcgowan, R. W. Mcgowan, D. Grischkowsky, and D. Grischkowsky, "Terahertz waveguides," *J. Opt. Soc. Am. B Opt. Phys.*, vol. 17, no. 5, pp. 851–863, 2000.

[26] N. Laman, S. S. Harsha, D. Grischkowsky, and J. S. Melinger, “High-resolution waveguide THz spectroscopy of biological molecules.,” *Biophys. J.*, vol. 94, no. 3, pp. 1010–1020, 2008.

[27] J. Zhang and D. Grischkowsky, “Waveguide terahertz time-domain spectroscopy of nanometer water layers.,” *Opt. Lett.*, vol. 29, no. 14, pp. 1617–1619, 2004.

[28] R. Mendis, V. Astley, J. Liu, and D. M. Mittleman, “Terahertz microfluidic sensor based on a parallel-plate waveguide resonant cavity,” *Appl. Phys. Lett.*, vol. 95, no. 17, pp. 1–4, 2009.

[29] K. S. Reichel, K. Iwaszczuk, P. U. Jepsen, R. Mendis, and D. M. Mittleman, “In situ spectroscopic characterization of a terahertz resonant cavity,” *Optica*, vol. 1, no. 5, pp. 272–275, 2014.

Chapter 2. **TERAHERTZ-TIME DOMAIN SPECTROSCOPY FOR THIN FILMS**

2.1 INTRODUCTION

Since the first experimental realization of terahertz time domain spectroscopy (THz-TDS) pioneered by Auston et *al.* [1] and Grischkowsky et *al.*,[2], the technique has gained maturity and continue to attract attention from a broad community of the scientists. By definition, THz-TDS is a coherent time domain detection method enabling to obtain simultaneously amplitudes and phases of the electric field spectrum. This coherent nature of detection greatly facilitates the extraction of electromagnetic properties of materials under analysis. In this chapter, I describe the principles of conventional THz-TDS techniques. The first paragraph outlines the basic principles of the method in transmission geometry. The second paragraph details the extraction process of thin film optical properties. The last paragraph explains the limitations associated with the present approach. Details of generating and detecting as well as free space beam shaping techniques will be presented in chapter 4.

2.2 TRANSMISSION THz-TDS

Conventional THz-TDS is based on the detection of discretized time domain profile of electric fields. The time scale of the pulse is order of picoseconds (ps).Fig. 2.1 summarizes the measurement principles with time domain pulse associated. The sample measured in Fig. 2.1 is magnesium oxide (MgO) with thickness of 0.5 mm. The frequency domain of the electric field is obtained using the Fourier transform of the time domain data. Therefore, given a discretized temporal waveform amplitude $E(t_\mathrm{j})$ where $t_\mathrm{j} = \mathrm{j}\Delta t$ and Δt is the resolution, the numerical computation of the Fourier transform is performed by the Fast Fourier Transform algorithm:

$$\left.\begin{aligned} E(\omega) &= \textstyle\sum_{\mathrm{j}=1}^{\mathrm{N}-1} E(t_\mathrm{j}) e^{-i\omega t_\mathrm{j}} \\ \varphi(\omega) &= \tan^{-1}\left(\frac{\mathrm{Im}(E(\omega))}{\mathrm{Re}(E(\omega))}\right) \end{aligned}\right\}, \tag{2.1}$$

where N is the length of the signal $E(t_\mathrm{j})$ and $E(\omega)$ is an array of complex number which dependent on the frequency *f*.

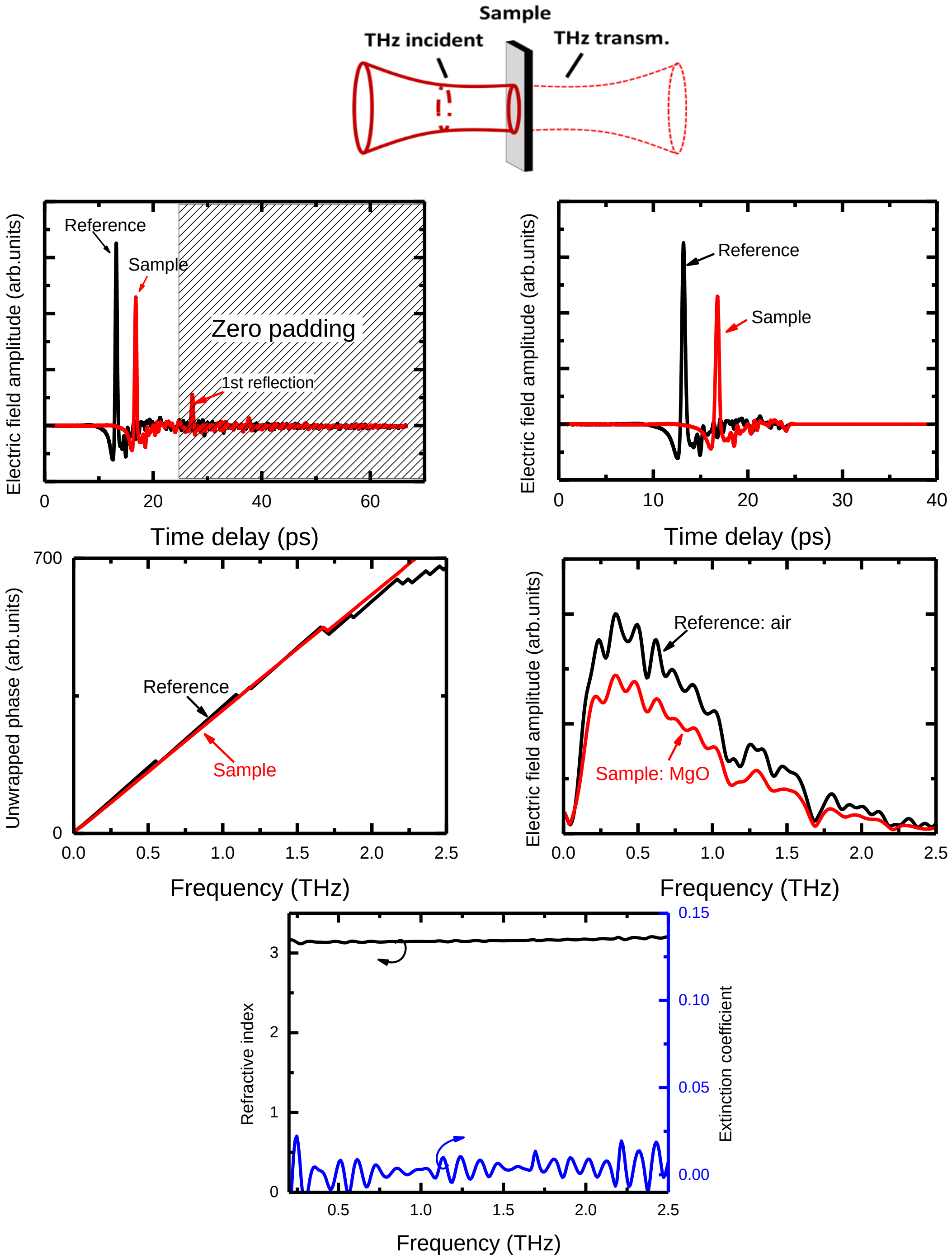

Fig. 2.1. Extraction of dielectric parameters (refractive index and extinction coefficient) in conventional THz – TDS. The reference signal is the THz incident field (air) and the sample is 0.5-mm-thick magnesium oxide. The Time domain signal is zero-padded from the first reflection. After FFT, the amplitude and phases are obtained. The refractive index (n≈3.15) and the extinction coefficient (k ≈ 0) are extracted.

After the FFT, the amplitude of the electric field and the phase are given by $|E(\omega)|$ and $\varphi(\omega)$ respectively. The frequency bandwidth depends on the temporal resolution of the signal from the relation $\Delta f = \frac{2\pi}{N\Delta t}$.

The dielectric function of materials under investigation is deducted from frequency dependent complex –valued transmission function $T(\omega)$ which is the ratio of the electric field detected through the sample $E_{\mathrm{samp}}(\omega)$ to a reference signal $E_{\mathrm{ref}}(\omega)$. In practical, the reference signal is the electric field measured without any sample and then the transfer function is given by:

$$T(\omega) = \frac{E_{samp}(\omega)}{E_{\mathrm{ref}}(\omega)} = \left|\sqrt{T(\omega)}\right| \exp\left[-i\left(\Delta\varphi(\omega)\right)\right]. \tag{2.2}$$

The sample and the reference signal must have the same temporal length and must start at the same time delay position to avoid a random phase difference. $\left|\sqrt{T(\omega)}\right|$ is the amplitude of the transmission function and $\Delta\varphi(\omega)$ is the phase differences between E_{samp} and E_{ref}.

The optical parameters of the sample can be extracted in a straightforward way from the transfer function but it is necessary, above all, to discuss about some conditions required for the THz beam and material samples [3]. The measurements in conventional THz-TDS are performed in the normal incidence, therefore the THz beam is approximated as plane waves propagating normal to the samples surface plane. Samples are supposed to be homogeneous, flat and to possess parallel faces. Samples should be also magnetically isotropic and have linear electromagnetic response. Many literatures have treated nonlinear THz spectroscopy with variety of techniques [4– 6] but we focus here on linear THz-TDS.

Suppose that the reference media is the air, the complex transmitted electric field trough a sample of thickness d can be analytically calculated as [7]:

$$\left.\begin{aligned} E_{\mathrm{samp}}(\omega) &= \frac{4n_{samp}n_{\mathrm{air}}}{\left(n_{samp}+n_{\mathrm{air}}\right)^2}\frac{\exp\left[-i\left(n_{\mathrm{samp}}-n_{\mathrm{air}}\right)\frac{\omega}{c}d\right]}{\mathrm{FP}(\omega)}E_{\mathrm{ref}}(\omega) \\ \mathrm{FP}(\omega) &= 1-\frac{\left(n_{\mathrm{samp}}-n_{\mathrm{air}}\right)^2}{\left(n_{\mathrm{samp}}+n_{\mathrm{air}}\right)^2}\exp(-i2n_{\mathrm{samp}}\frac{\omega}{c}d) \end{aligned}\right\}, \tag{2.3}$$

where FP is the Fabry-Perrot effect due to the multiple reflections inside the sample. n is the refractive index of the media and should be understood as complex value number. n_{air} is the refractive index of air and n_{samp} is the refractive index of the sample. Extracting n_{samp} by Eq. (2.2) and Eq. (2.3), we can calculate the complex relative dielectric constant and the complex conductivity by the following relations:

$$\left.\begin{aligned}\epsilon(\omega) = \epsilon_1(\omega) - i\epsilon_2(\omega) = [n(\omega)]^2 \\ \sigma(\omega) = \sigma_1(\omega) - i\sigma_2(\omega) = \omega\epsilon_0[\epsilon_2(\omega) - i(\epsilon_\infty - \epsilon_1(\omega))]\end{aligned}\right\}, \qquad (2.4)$$

Here, ϵ_0 and ϵ_∞ are the permittivity of the free space and the dielectric constant of the material at enough high frequency, respectively.

However, some constraints are imposed by Eq. (2.3) to properly extract the optical parameters. First, the complex refractive index is not obtained in a straightforward manner due to the FP effect. Then, an optimization process should be performed numerically to solve that issue. An algorithm as Newton-Raphson type or spatially variant moving average filter can greatly improve the parameters' extraction [7]. Second, the phase values in Eq. (2.1) are bounded in [-π,π] while the experimental values of the phase can exceed that interval. The phase has to be unwrapped to stay in the boundary. Some built-in functions like "unwrap" function of MATLAB® can automatically correct the angle jump between two consecutive values.

When the sample is thick enough and the main transmitted pulse and the first echo is temporally well separated, we can use a *windowing* function to eliminate reflection pulses (cf. Fig. 2.1). In that case, the transfer function in Eq. (2.3) is simplified such as:

$$T(\omega) = \frac{4n_{\mathrm{samp}}n_{\mathrm{air}}}{\left(n_{\mathrm{samp}} + n_{\mathrm{air}}\right)^2}\exp\left[-i\left(n_{\mathrm{samp}} - n_{\mathrm{air}}\right)\frac{\omega}{c}d\right]. \qquad (2.5)$$

Here, the complex refractive index can be retrieved directly without optimization process. The phase of the transfer function is directly related to the real part of refractive index and it is easy to calculate the extinction coefficient afterwards.

2.3 THZ-TDS OF THIN CONDUCTIVE FILMS ON SUBSTRATE

Theory of electromagnetic wave propagation normally incident to layered dielectric has been treated in many textbook and literatures [8– 10]. Transmission and reflection coefficients can be obtained straightforwardly using the boundary conditions of electromagnetic fields. However, the calculation is very long and complicated so that we make use of transmission line theory and impedance concept to carry out the problem.

Consider a thin conductive film of thickness d_1 on a substrate of complex refractive index n_{sub} as shown Fig. 2.2. The electric field, after passing through multilayer system, has the form:

$$E_{\mathrm{samp}}(\omega) = t_{0\to1\to2}t_{2\to0}e^{-i\omega\frac{n_2}{c}d_2}E_{\mathrm{ref}}(f), \qquad (2.6)$$

where $t_{0\to1\to2}$ and $t_{2\to0}$ are the amplitude coefficients of the transmission for the wave passing through air region to the substrate and from the substrate to the air, respectively. Here, we make a rough approximation that the film thickness satisfy the condition $n_{t\text{hin film}}\frac{\omega}{c}d_1 \ll 1$ so that the phase factor is negligible. We make use of the transmission line theory to calculate those coefficients. Fig. 2.2 illustrates an equivalent transmission line circuit for a wave propagating from the left to the right. If Z_0, Z_1, Z_2 and Z_L are the impedances of free space, thin conductive film, the substrate and load impedance, respectively, the coefficients of transmission are given by:

$$\left.\begin{aligned} t_{0\to 1\to 2} &= \frac{2Z_\mathrm{L}}{Z_\mathrm{L}+Z_0} \\ t_{2\to 0} &= \frac{2Z_2}{Z_2+Z_0} \end{aligned}\right\}, \tag{2.7}$$

Here, we are only interested in the direct transmitted THz pulse and neglect the reflection from boundary interface. From the definition of electromagnetic wave impedance for a plane wave, we have:

$$Z_\mathrm{j} = \frac{Z_0}{n_\mathrm{j}},\ \mathrm{j} = 0,1,2 \tag{2.8}$$

where n_j is the complex refractive index of the media numbered j. In the film approximation where the thickness is far below the skin depth δ ($d_1 \ll \delta$), the film impedance is obtained by the discontinuity of the magnetic field caused by uniform current density J [8, 9]:

$$Z_1 = \frac{E}{H_0 - H_2} \approx \frac{E}{J} = \frac{1}{\sigma d_1}, \tag{2.9}$$

where σ is the frequency dependent complex conductivity of the film, H_0 and H_2 are the magnetic fields in the region "0" and the region "2". Finally, the load impedance can be found as:

$$Z_\mathrm{L} = \frac{Z_1 Z_2}{Z_1 + Z_2}. \tag{2.10}$$

If the first region is the free space ($n_1 = n_\mathrm{air}$), combining the transfer function of the substrate only in Eq. (2.5) and Eq.(2.6) - (2.10), we obtain the so-called Tinkham formula for thin conductive film [10]:

$$T_{\text{thin film}}(\omega) = \frac{1 + n_\mathrm{Sub}}{1 + n_\mathrm{Sub} + Z_0 \sigma d_1}. \tag{2.11}$$

Therefore, the reference signal is the electric field detected through the substrate, and the sample signal is the electric field transmitted through thin conductive film on substrate. The optical parameters for the substrate are calculated from Eq. (2.5) and the values obtained are inserted into eq. (2.11). Generally, the conductivity of thin film is expressed by surface or sheet conductivity σ_S with unit S:

$$\sigma_S(\omega) = \sigma(\omega)d_1. \tag{2.12}$$

Since $T_{\text{thin film}}(f)$ is a complex - valued function, the determination of the real and imaginary part of sheet conductivity is straightforward.

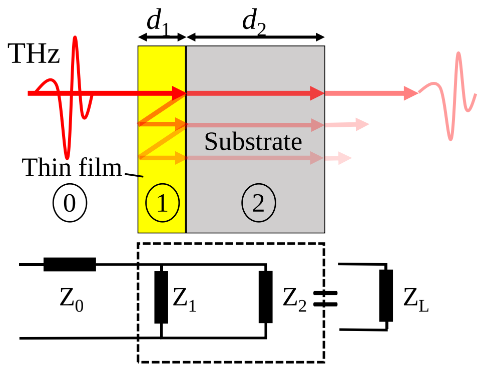

Fig. 2.2 Transmission line equivalence of thin conductive thin on a substrate. The film has a thickness d_1 and the substrate has a thickness of d_2. The electromagnetic field can be described by the impedances in each area. The impedance of the thin film Z_1 and the substrate Z_2 are equal to an equivalent impedance Z_L.

2.4 LIMITATIONS OF CONVENTIONAL THz-TDS IN CONDUCTIVE THIN FILMS CHARACTERIZATION.

Characterization of ultrathin conductive films depends on several parameters of the samples, the extraction procedure and the experimental system itself. Another major factor which influences the success of thin film characterization is the type of analysis to perform. Review on thin film sensing and nanostructure films characterization in THz regime have been reported in previous works [11, 12].The possibilities and challenges are illustrated in those works, but here we focus on the major issues met in ultrathin or two-dimensional (2D) or nanostructure conductive materials.

The dominant challenge in THz-TDS when analyzing very thin films is increasing “sensitivity”. When the interaction of the THz wave with the thin film is extremely weak, improving sensitivity means increasing minimum detectable signal change induced by the samples. However, sensitivity is quite general term which could be a qualitative indication of the performance of the system and depending on the type of analysis. In spectroscopic application, we intend mainly to obtain dynamic information of the thin film properties so that the sensitivity is reflected in the dielectric constant extracted. In numerous examples [12–14], the sensitivity is quantified generally by the minimum and the maximum absorption detected. The parameters involved when determining the sensitivity are the dynamic range (DR) and the signal to noise ratio (SNR) of the system.

Here, we adopt the definition based on [15]:

$$\mathrm{DR} = \frac{\text{mean magnitude of signals amplitude}}{\text{standard deviation of signals amplitude}}$$

$$\mathrm{SNR} = \frac{\text{maximum magnitude of signals amplitude}}{\text{root mean square of noise floor}} \tag{2.13}$$

The quantity DR indicates the maximum calculable signal change while SNR determines the minimum detectable signal change. Both quantities can be time dependent or conversely frequency dependent.

DR and SNR of THz-TDS depend on the performance of each component of the system and the quality/quantity of the thin film samples. If we suppose that those two factors are optimal for the experimental system, one way to increase the sensitivity is to increase the thickness of the samples for example or to process the sample to have a better responses. But then, those process already modify and even alter the *intrinsic* electromagnetic properties of the samples.

Since the ultimate goal of spectroscopic system optimization is to obtain a high quality data with high SNR, in a reasonable time and with the most efficient method possible, conventional THz-TDS analysis is very challenging when:

- the change induced by the thin conductive film samples is not measurable (beyond the SNR of the system).
- the samples are required to be processed in order to improve the interaction.
- obtaining a reasonable quality of the extracted parameters involves a consequent amount of time.

REFERENCES

[1] K. P. Cheung and D. H. Auston, “A novel technique for measuring far-infrared absorption and dispersion,” *Infrared Phys.*, vol. 26, no. 1, pp. 23–27, 1986.

[2] M. Van Exter, C. Fattinger, and D. Grischkowsky, “Terahertz time-domain spectroscopy of water vapor,” *Opt. Lett.*, vol. 14, no. 20, pp. 1128–1130, 1989.

[3] K. Sakai, *Terahertz optoelectronics*, Springer, vol. 97, 2005.

[4] K. Tanaka, H. Hirori, and M. Nagai, “THz nonlinear spectroscopy of solids,” *IEEE Trans. Terahertz Sci. Technol.*, vol. 1, no. 1, pp. 301–312, 2011.

[5] E. Bründermann, H-W Hübers, and M. F. Kimmitt, “Terahertz Techniques,” Springer series in Optical sciences, vol. 151, 2012.

[6] M. C. Hoffmann, N. C. Brandt, H. Y. Hwang, K. Lo Yeh, and K. A. Nelson, “Terahertz Kerr effect,” *Appl. Phys. Lett.*, vol. 95, no. 23, pp. 100–103, 2009.

[7] I. Pupeza, R. Wilk, and M. Koch, “Highly accurate optical material parameter determination with THz time-domain spectroscopy.,” *Opt. Express*, vol. 15, no. 7, pp. 4335–4350, 2007.

[8] S. Ramo, "*Fields and waves in communication electronics*," J. Wiley, 2008.

[9] M. Dressel, G. Gruener, and G. F. Bertsch, “Electrodynamics of Solids: Optical Properties of Electrons in Matter,” *Am. J. Phys.*, vol. 70, no. 12, p. 1269, 2002.

[10] R. E. Glover and M. Tinkham, “Conductivity of superconducting films for photon energies between 0.3 and 40kTc,” *Phys. Rev.*, vol. 108, no. 2, pp. 243–256, 1957.

[11] J. F. O’Hara, W. Withayachumnankul, and I. Al-Naib, “A review on thin-film sensing with terahertz waves,” *J. Infrared, Millimeter, Terahertz Waves*, vol. 33, pp. 245–291, 2012.

[12] W. Withayachumnankul, “Limitation in thin-film detection with transmission-mode terahertz time-domain spectroscopy,” *Opt. Express*, no 22, pp 972 - 986, 2014..

[13] J. S. Melinger, Y. Yang, M. Mandeghar, A. Shutler, and D. Grischkowsky, “THz detection of small molecule vapors over long paths in the atmospheric transmission windows,” *Opt. Express*, vol. 20, no. 6, pp. 6788–6807, 2012.

[14] H.-W. Hübers, M. F. Kimmitt, N. Hiromoto, and E. Bründermann, “Terahertz Spectroscopy: System and Sensitivity Considerations,” *IEEE Trans. Terahertz Sci. Technol.*, vol. 1, no. 1, pp. 321–331, 2011.

[15] M. Naftaly and R. Dudley, “Methodologies for determining the dynamic ranges and signal-to-noise ratios of terahertz time-domain spectrometers.,” *Opt. Lett.*, vol. 34, no. 8, pp. 1213–1215, 2009.

Chapter 3. **DERIVATION OF THE ANALYSIS METHOD FOR THIN CONDUCTIVE FILMS USING PARALLEL PLATE WAVEGUIDE**

3.1 INTRODUCTION

The techniques of guiding wave in the THz regime come mainly from microwave and millimeter wave techniques. Optical waveguides such as dielectric waveguides or photonic crystal waveguides [1] are still in earlier step of development and require further investigations to overcome the relevant challenge to reduce the wave propagation loss. In contrast, metallic waveguides have proven their efficiency in the THz technology and have gained growing interest from many researchers.

The first demonstration of THz wave coupled to a metal tube waveguide was reported by Grischkowsky group in early 2000 [2]. In this work, quasi-optical coupling technique with two hyper hemispherical silicon lenses was used to focus the THz beam to a spot of diameter around 300 µm ($\approx\lambda_{1\mathrm{THz}}$). This coupling method was very efficient and had been extended to several type of waveguides including rectangular waveguide and parallel plate waveguide (PPWG) [3]. Nevertheless, the major issue of some waveguides type having circular or rectangular cross section was the pulse reshaping. When the cross section of the waveguides becomes order of the THz wavelength, the cutoff frequencies shift to higher frequency and results in a large broadening of the output pulses. In other words, the extreme broadening of the pulse is caused by the group velocity dispersion near the cutoff frequency. On the other hand, metal wires [4] and parallel plate waveguide can support transverse electromagnetic mode. While the former waveguide has a promising future in telecommunication applications, the latter one has an outstanding performance in THz spectroscopy [5].

As I will describe in the next section, there is no cutoff frequency in the fundamental TEM mode of PPWG resulting in an undistorted output pulse. Consequently, making use of this mode enables to have a clean broadband spectrum and wavelength focusing guided wave. In THz-TDS applications, a thin dielectric is directly drop casted on the bottom plates of the PPWG. The change in phase and amplitude of transmitted THz pulse induced by the thin film is related to the dielectric constant of the thin layer. For example, a layer of water vapor about 20 nm thick has been successfully characterized by using TEM mode of PPWG [6].

The transverse electric mode can also propagate in the PPWG. If we suppose that the waveguide plate separation is around 300 μm and the medium filling the PPWG is air, the cutoff frequency of fundamental TE_1 mode is 0.5THz. There is no propagation for frequency below 0.5THz, and the transmitted pulse is highly distorted. Therefore, this particular mode did not attract much attention for THz spectroscopy. However, in 2005 R. Mendis and D. Mittleman demonstrated that undistorted THz pulse can be obtained by the use ofTE_1 mode. In addition, the intrinsic propagation loss due to the plate conductivity of TE_1 mode is much lower than that of TEM mode [7]. Shortly after, many applications emerged from TE_1 mode of PPWG including molecular sensing [8].

In this chapter, I derive the main theory of thin conductive film inserted in PPWG and the method to extract optical parameters in THz-PPWG-TDS. The second section describes the general theory of propagating wave in PPWG. In the third section, I establish the dispersion equations of conductive film in PPWG. In the fourth section, I develop the quasi-optical free space coupling method for PPWG. Then, the complex transfer function will be shown in fifth section. The last section summarizes the parameters extraction scheme utilized in this work.

3.2 PARALLEL PLATE WAVEGUIDE

3.2.1 *General Solutions of waveguide*

An ideal PPWG is composed of two parallel perfect conductor planes separated at a distance *d* by a dielectric medium [9]. As long as the dielectric is isotropic and homogeneous, the following analysis is always valid. In this chapter the coordinates system is shown in Fig. 3.1 with the propagation following the *z*-axis. We begin by writing the basic Maxwell's equations:

$$\nabla \cdot \boldsymbol{D} = \rho, \tag{3.1}$$

$$\nabla \cdot \boldsymbol{B} = 0, \tag{3.2}$$

$$\nabla \times \boldsymbol{E} = -\frac{\partial \boldsymbol{B}}{\partial t}, \tag{3.3}$$

$$\nabla \times \boldsymbol{H} = \boldsymbol{J} + \frac{\partial \boldsymbol{D}}{\partial t}, \tag{3.4}$$

where $\boldsymbol{D}$ and $\boldsymbol{B}$ are the electric and magnetic flux densities while $\boldsymbol{E}$ and $\boldsymbol{H}$ are the electric and magnetic field, respectively. ρ and $\boldsymbol{J}$ are the charge and current density, respectively. Bold characters are vectors and normal characters are scalar.

Assume a time variation of the form $e^{-i\omega t}$ with angular frequency ω, the general solutions of Maxwell equation are:

$$\left.\begin{aligned} \boldsymbol{E}(x,y,z,t) &= \boldsymbol{E}(x,y)e^{\pm i\gamma z - i\omega t} \\ \boldsymbol{B}(x,y,z,t) &= \boldsymbol{B}(x,y)e^{\pm i\gamma z - i\omega t} \end{aligned}\right\}. \tag{3.5}$$

Appropriate sign on γ should be chosen to have forward (+) or backward (-) propagating wave. γ is the wavenumber or propagation constant in z direction and is a complex-valued number. We can separate the fields into transverse components and z – components by [10]:

$$\left.\begin{aligned} \boldsymbol{F}_z &= F_z\boldsymbol{z} \\ \boldsymbol{F}_t &= (\boldsymbol{z}\times\boldsymbol{F})\times\boldsymbol{z} \\ \boldsymbol{F} &= \boldsymbol{F}_t + \boldsymbol{F}_z \\ \boldsymbol{\nabla}^2 &= \boldsymbol{\nabla}_t{}^2 + \frac{\partial^2}{\partial z^2} \end{aligned}\right\}, \tag{3.6}$$

where $\boldsymbol{F}$ stands for $\boldsymbol{E}$ or for $\boldsymbol{B}$ and $\boldsymbol{z}$ is an unit vector along the z-axis.

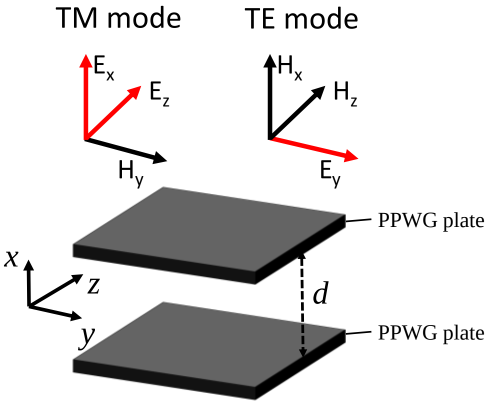

Fig. 3.1 Geometry of parallel plate waveguide with coordinates system. The propagation of wave is in z – axis. The orientation of the electric and magnetic field of TM and TE mode are also shown on the top of the Fig.

Inserting the solutions Eq. (3.5) to Eqs. (3.3) - (3.4) and separating the transverse and longitudinal components of the fields, we obtain for the positive travelling wave and source-free Maxwell's equations:

$$\boldsymbol{\nabla}_t{}^2\boldsymbol{F} = (\gamma^2 - \omega^2\mu\epsilon)\boldsymbol{F}, \tag{3.7}$$

$$\boldsymbol{E}_t = \frac{i\gamma}{(\omega^2\mu\epsilon - \gamma^2)}\left[\boldsymbol{\nabla}_t E_z - \frac{\omega}{\gamma}(\boldsymbol{z}\times\boldsymbol{\nabla}_t B_z)\right], \tag{3.8}$$

$$\boldsymbol{B}_t = \frac{i\gamma}{(\omega^2\mu\epsilon - \gamma^2)}\left[\boldsymbol{\nabla}_t B_z - \frac{\omega\mu\epsilon}{\gamma}(\boldsymbol{z}\times\boldsymbol{\nabla}_t E_z)\right]. \tag{3.9}$$

Eqs. (3.8) - (3.9) hold if both $\boldsymbol{E}_z$ and $\boldsymbol{B}_z$ are not zero simultaneously. We will see below that there is a special case where both $\boldsymbol{E}_z$ and $\boldsymbol{B}_z$ vanish.

The existence and the uniqueness of the solutions are determined by Eq. (3.7) and the boundary conditions that should be satisfied by $\boldsymbol{E}$ and $\boldsymbol{B}$. When the electromagnetic field is enclosed in (transverse directions) perfect electric conductor, $\boldsymbol{E}$and $\boldsymbol{B}$vanish inside the conductor. On the conductor surface, the boundary conditions are:

$$\left.\begin{array}{r}\boldsymbol{n}\times\boldsymbol{E}=0\\ \boldsymbol{n}\cdot\boldsymbol{B}=0\end{array}\right\}. \tag{3.10}$$

The boundary conditions ensure the continuity of tangential electric field and the continuity of normal component of magnetic flux density. Here, $\boldsymbol{n}$ is a unit vector normal to the surface of the conductor (or any interface between two different media). Then, the components E_z and B_z on the surface satisfy:

$$\left.\begin{array}{r}E_z=0\\ \dfrac{\partial B_z}{\partial n}=0\end{array}\right\}, \tag{3.11}$$

where $\frac{\partial}{\partial n}$ is the normal derivative at appoint of the surface. In Eqs. (3.8) - (3.9), we have to solve both E_z and B_z to obtain $\boldsymbol{E}_t$ and $\boldsymbol{B}_t$. However, for each boundary conditions of Eq. (3.11) correspond to different eigenvalues of Eq. (3.7). It is evident that any superposition of those solutions would satisfy also Maxwell's equations. If $\boldsymbol{E}_{t1}$ and $\boldsymbol{B}_{t1}$ is the solutions of Eq. (3.8) - (3.9) with the conditions $E_z = 0$ on the surface and $B_z = 0$ everywhere, and $\boldsymbol{E}_{t2}$ and $\boldsymbol{B}_{t2}$ are the solutions with the conditions $E_z = 0$ everywhere and $\frac{\partial B_z}{\partial n} = 0$ on the surface, it results to [10]:

$$\left.\begin{array}{c}\boldsymbol{E}_1=\boldsymbol{E}_{t1}+E_z\boldsymbol{z},\qquad \boldsymbol{B}_1=\boldsymbol{B}_{t1}\\ \boldsymbol{E}_2=\boldsymbol{E}_{t2},\boldsymbol{B}_2=\boldsymbol{B}_{t2}+B_z\boldsymbol{z}\\ \boldsymbol{E}=\boldsymbol{E}_1+\boldsymbol{E}_2,\boldsymbol{B}=\boldsymbol{B}_1+\boldsymbol{B}_2\end{array}\right\}, \tag{3.12}$$

Since the first equations of Eq. (3.12) has only $\boldsymbol{B}_t$, these equations are the solutions of mode called "*transverse magnetic mode*". Similarly, the second equations are the solutions of mode called "*transverse electric mode*". The existence of particular mode depends on the excitation fields. It is convenient to express the relation between the transverse electric and magnetic field as:

$$\boldsymbol{H}_t=-\frac{1}{Z}(\boldsymbol{z}\times\boldsymbol{E}_t), \tag{3.13}$$

here Z is the wave impedance. The expression of Z is:

$$Z = \begin{cases} \dfrac{\gamma}{\omega\epsilon} \text{ (TM mode)} \\ \dfrac{\omega\mu}{\gamma} \text{ (TE mode)} \end{cases} \tag{3.14}$$

3.2.2 *TM mode and TE modes of PPWG*

As indicated above, TM mode has a non-vanishing E_z component. Additionally, the PPWG is assumed to be in infinite extension in y direction so that the derivations with respect to y coordinate vanish. From Eq.(3.7), the equation of E_z is:

$$\frac{d^2E_z}{dx^2} - (\gamma^2 - \omega^2\mu\epsilon)E_z = 0. \tag{3.15}$$

Applying the boundary conditions $E_z = 0$ on the plate surface at $x = 0$ and $x = d$ (Fig. 3.1), the solutions of Eq. (3.15) is:

$$E_z = A\sin(k_x x), \tag{3.16}$$

with:

$$\begin{gathered} k_x = (\omega^2\mu\epsilon - \gamma^2)^{1/2} = \frac{\mathrm{m}\pi}{d} \\ \mathrm{m} = 0, 1, 2 \ldots \end{gathered} \tag{3.17}$$

For each integer m corresponds to one specific mode. Solving Eq. (3.17) gives the “cutoff frequency” of the mode:

$$f_c = \frac{\mathrm{m}c}{2\sqrt{\epsilon}d} \tag{3.18}$$

where c is the light velocity. When the frequency $f < f_c$, the propagation constant γ is purely imaginary. Then, from Eq. (3.5), the fields are decaying along the guide. The condition of propagation for a specific mode is that $f > f_c$.

The remaining components of the field are obtained by Eqs. (3.8) - (3.9). For TM mode of PPWG, the electromagnetic field is composed by:

$$\left.\begin{aligned} E_z &= A\sin(k_x x) \\ E_x &= \frac{i\gamma}{k_x}A\cos(k_x x) \\ H_y &= -\frac{i\omega\epsilon}{k_x}A\cos(k_x x) \end{aligned}\right\}. \tag{3.19}$$

The first mode, or fundamental mode of TM is TM_0 where m = 0. This is a special case in PPWG where E_z and H_z are simultaneously zero and the cutoff frequency also vanish. The electric and magnetic field lie totally in the transverse plane of the waveguide and have the form:

$$\left.\begin{aligned} E_x &= Ce^{i\gamma z} \\ H_y &= \frac{1}{Z_{TM}} Ce^{i\gamma} \end{aligned}\right\}, \tag{3.20}$$

where C is a constant and Z_{TM} is the TM wave impedance in Eq. (3.14).

By proceeding in the same manner as TM mode, but with $\frac{\partial B_z}{\partial n} = 0$ on the surface of the waveguide plates, the fields in TE mode are:

$$\left.\begin{aligned} H_z &= B\cos(k_x x) \\ H_x &= -\frac{i\gamma}{k_x} B\sin(k_x x) \\ E_y &= \frac{i\omega\mu}{k_x} A\sin(k_x x) \end{aligned}\right\}, \tag{3.21}$$

with the same cutoff frequency expression. However, from Eq. (3.21), the mode with order m = 0 cannot exist. Therefore, the fundamental mode of TE is the TE_1 mode where m = 1.

If the conductor plates have finite conductivity, the current induced by magnetic field on both plates participates to the propagation loss of the waveguide and result in a complex propagation constant:

$$\gamma = \beta + i\alpha. \tag{3.22}$$

One usually compute that attenuation by approximation method, namely by power transfer method [9]. The loss α for TM and TE mode are:

$$\left.\begin{aligned} \alpha_{TM} &= \frac{2\omega\epsilon(\pi\mu_c f/\sigma_c)^{1/2}}{\beta d} \text{ for TM mode} \\ \alpha_{TE} &= \frac{2\pi^2(\pi\mu_c f/\sigma_c)^{1/2}}{\omega\beta\mu d^3} \text{ for TE mode} \end{aligned}\right\}, \tag{3.23}$$

where σ_C and μ_C are the conductivity and permeability of the conductor plates, respectively. The waveguide loss depends on the frequency, the plate separation d and the conductivity of the metallic plates. The conductor plates used for PPWG in THz frequency range are usually aluminum, copper and sometimes coated by thin gold in order to increase the conductivity, thereby minimizes the loss. In THz regime, the bulk conductivities of those metals are nearly flat over the operating frequency bandwidth of the PPWG. Accordingly, it is common to consider the bulk DC conductivity values to compute the loss in Eq. (3.22).

Table 3.1 shows values of bulk conductivity of some metal. These results are calculated in room temperature.

Table 3.1 Bulk conductivity of some metal from Ref. [11]

Metal	Bulk σ_{DC} $(\mu\Omega.m)^{-1}$at 293°K
Aluminum (Al)	37.73
Copper	59.8
Gold	45.16

It should be noted that the attenuation is real valued frequency-dependent. Eq. (3.22) are only valid for $f < f_c$. The loss due to the finite conductivity is termed as "resistive loss". In summary of this section, Fig. 3.2 show the magnitude of electric fields and magnetic fields of TEM, TM_2 and TE_1 mode of PPWG.

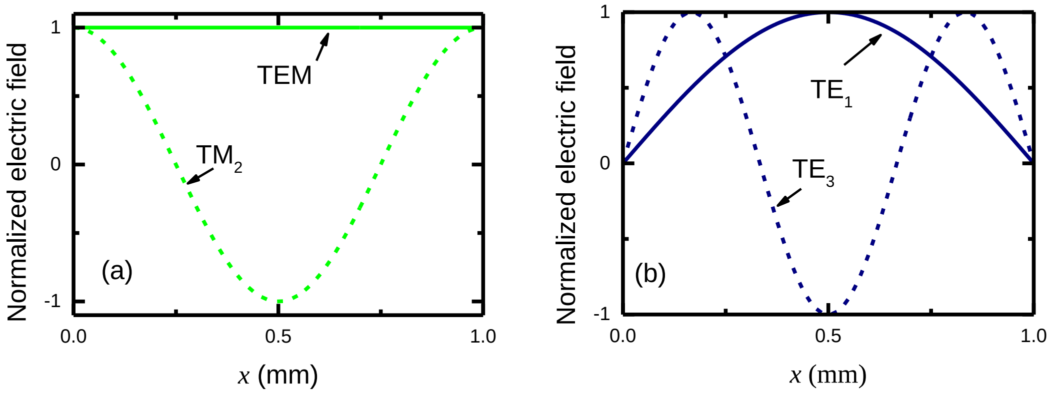

Fig. 3.2 Normalized electric field profile inside the PPWG. (a) The normalized electric field for TEM and TM_2 mode. (b) The normalized electric field for TE_1 and TE_3 modes

3.3 PARALLEL PLATE WAVEGUIDE WITH THIN CONDUCTIVE FILM

The dispersion equation for thin conductive film placed symmetrically inside the PPWG can be determined exactly without any approximation [12]. However, when the thickness of the materials is infinitely thin and far less than the THz wavelength and the skin depth, appropriate boundary conditions can be used. In this paragraph, a rigorous formulation is first provided to obtain the electromagnetic field in the PPWG. Here we limit the equations to TM mode case but TE mode dispersion equation can be easily found by applying the same procedure. The next section details a different approach to derive the dispersion equation by making use of surface current density approximation.

3.3.1 *Fields equations for TM mode*

The geometry model of thin conductive film inside a PPWG is shown in Fig. 3.3. The layer is centrally placed parallel to the waveguide plates. Therefore, the field has no variation in *y*-axis, same as the empty PPWG. The film has a thickness *t*, effective dielectric permittivity ϵ_C, permeability μ_C and conductivity σ_C. The permittivity and permeability of the dielectric medium between the plate and the film are ϵ and μ, respectively.

In the area 1 and 2, the electric and magnetic field expressions are given by Eq. (3.19) for TM mode. With the dimensions and coordinates given by Fig. 3.3 we have:

$$E_{z1} = A_1 \sin\left(k_{x1} \left(\frac{d}{2} \mp x \right) \right) \text{for } |x| > \frac{d}{2}. \tag{3.24}$$

The sign minus is for $x > t/2$ and sign plus is for x < $t/2$. It is also seen that the system presented in Fig. 3.3 has a physical symmetry at $x = d/2$. Therefore, the solutions of Maxwell's equation can be deduced by considering only the region x > 0. Furthermore, the electric field component E_{z1} can be symmetric or antisymmetric relative to *x*-*z* plane.

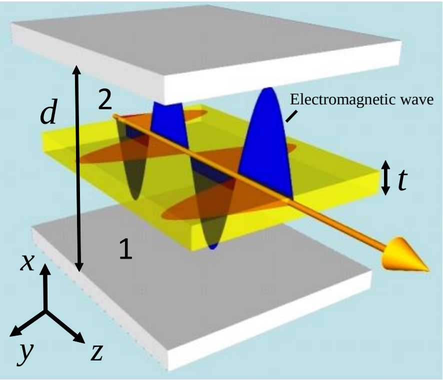

Fig. 3.3 Thin conductive film located halfway between the plates of PPWG. The coordinates system are the same as in Fig. 3.2. The thickness of the film is *t* and the plate separation is *d*. The region 1 and 2 are the substrate area which is the host medium of the film.

For now, there is no assumption concerning the thin conductive film. So, it is considered as dielectric medium in which the guided electromagnetic field is well known [12]. Within the dielectric, the mode profile can be expressed in sine or cosine functions. Then, the tangential electric field in the region 2 is:

$$\left.\begin{aligned} E_{z2} &= A_2 \sin(k_{x2}x) \text{for } |x| < \frac{t}{2} \text{(antisymmetric), or} \\ E_{z2} &= A_2 \cos(k_{x2}x) \text{for } |x| < \frac{t}{2} \text{(symmetric)} \end{aligned}\right\}. \tag{3.25}$$

The remaining fields are obtained by Eqs. (3.8) - (3.9). For x > 0:

$$\left.\begin{array}{l}
\left.\begin{aligned}
E_{x1} &= -\frac{i\gamma}{k_{x1}} A_1 \cos\left(k_{x1}\left(\frac{d}{2}-x\right)\right)\\
H_{y1} &= \frac{i\omega\epsilon}{k_{x1}} A_1 \cos\left(k_{x1}\left(\frac{d}{2}-x\right)\right)
\end{aligned}\right\} \text{for } |x| > \frac{t}{2},\\
\left.\begin{aligned}
E_{x2} &= \frac{i\gamma}{k_{x2}} A_2 \cos(k_{x2}x)\\
H_{y2} &= -\frac{i\omega\epsilon_c}{k_{x2}} A_2 \cos(k_{x2}x)
\end{aligned}\right\} \text{for } \frac{t}{2} > |x| > 0 \text{ (antisymmetric)},\\
\left.\begin{aligned}
E_{x2} &= -\frac{i\gamma}{k_{x2}} A_2 \sin(k_{x2}x)\\
H_{y2} &= \frac{i\omega\epsilon_c}{k_{x2}} A_2 \sin(k_{x2}x)
\end{aligned}\right\} \text{for } \frac{t}{2} > |x| > 0 \text{ (symmetric)}.
\end{array}\right\}. \tag{3.26}$$

The continuity conditions of the tangential fields at *t*/2 leads to two sets of transcendental dispersion equations:

$$\left.\begin{aligned}
\frac{k_{x1}}{\epsilon}\tan\left(k_{x1}\left(\frac{d-t}{2}\right)\right) &= -\frac{k_{x2}}{\epsilon_c}\tan\left(k_{x2}\frac{t}{2}\right) \text{ (antisymmetric)}\\
\frac{k_{x1}}{\epsilon}\tan\left(k_{x1}\left(\frac{d-t}{2}\right)\right) &= \frac{k_{x2}}{\epsilon_c}\cot\left(k_{x2}\frac{t}{2}\right) \text{ (symmetric)}
\end{aligned}\right\}, \tag{3.27}$$

with:

$$\gamma^2 = \omega^2\mu\epsilon - {k_{x1}}^2 = \omega^2\mu_c\epsilon_c - {k_{x2}}^2 \tag{3.28}$$

Eqs. (3.27) - (3.28) provide a complete description of the modes inside the PPWG. Numerical computation can solve these transcendental equations with the complex-valued propagation constant γ as the unknown parameter. Here, the symmetricity of the solution is relative to the *x*-*z* plane (mainly E_z).

Now, if the thickness of *t* of the dielectric is zero, the antisymmetric equation gives $k_{x1} = 2\text{m}\pi/d$ with m = 0, 1, 2…The symmetric equation gives $k_{x1} = \text{m}\pi/d$ with m = 1, 2…Then, with the first equation of Eq. (3.27), we find exclusively the modes of empty PPWG with even index including TEM, TM_2 etc. The first higher order TM1 mode belong to the second equation of Eq. (3.27).

Now, assume that the film is mainly characterized by its conductivity such that $\epsilon_C \approx \sigma_C/i\omega$, and $\mu = \mu_C$. These assumptions will be justified later when we treat the case of extremely thin conductive films. Assume also that the real part of ϵ and ϵ_C are the same order of magnitude and the propagation constant γ does not change much from the propagation constant of empty PPWG. If the film has an appreciable conductivity ($\sigma_C/i\omega\epsilon \gg 1$), then [9]:

$$k_{x2} \approx i\sqrt{i\omega\mu_C\sigma_c} = \frac{i(i+1)}{\delta}, \tag{3.29}$$

where $\delta = 1/\sqrt{\pi f \mu_{\mathrm{C}}\sigma_{\mathrm{C}}}$ is the skin depth of the conductive layer.

It should be noticed that the approximation about the propagation constant is a crude approximation but it is only assumed here to draw a physical insight of Eq. (3.27). Inserting Eq. (3.29) into Eq. (3.27), the first equation gives:

$$k_{x1}\tan\left(k_{x1}\left(\frac{d-t}{2}\right)\right) \approx \frac{(1+i)\epsilon\omega}{\delta\sigma_C}\tan\left(i(i+1)\frac{t}{2\delta}\right), \tag{3.30}$$

Here, the quantity $1/\delta\sigma_C$ is called the surface resistivity. Values of surface resistivity at different frequencies can be widely found in handbooks [11]. Similar equation can be derived for the symmetric case of Eq.(3.27) but with cot function instead of tan function in the right hand side (r.h.s) of the equation.

In this work, we are mainly interested with the case of extremely thin conductive films with the conditions $t/\delta \ll 1$. Then, if the thickness is far below the skin depth, the numerator of the r.h.s in Eq. (3.30) tends toward zero. Consequently, the first eigenvalue of $k_{x1} = 0$. The fundamental mode of PPWG with a very thin conductive film is quasi -TEM mode like in empty PPWG. Also, when $t/\delta \ll 1$ and $\sigma_{\mathrm{C}} \rightarrow \infty$ (perfect electric conductor), then $k_{x1} \rightarrow 0$.

In contrast, when $t/\delta \ll 1$ for the symmetric equation, the propagation constant in the dispersion equation exclusively depends on the conductivity of the thin film. By inserting Eq. (3.29) into Eq. (3.27) and expanding the cotangent function, we have:

$$k_{x1}\tan\left(k_{x1}\left(\frac{d-t}{2}\right)\right) \approx -\frac{(1+i)\epsilon\omega}{\delta\sigma_C}\cot\left(i(i+1)\frac{t}{2\delta}\right) \approx -\frac{2\epsilon\omega}{i\sigma_{\mathrm{C}}t}, \tag{3.31}$$

when $\sigma_{\mathrm{C}} \rightarrow \infty$, the fundamental mode of the waveguide is also TEM mode. When $\sigma_{\mathrm{C}} \rightarrow 0$, the Eq. (3.31) becomes the dispersion equation of higher order TM mode of the empty waveguide.

From Eq. (3.27), it was shown that extracting the propagation constant is complicated without many assumptions. However, for extremely thin film, the continuity conditions for electromagnetic fields can be reduced to boundary conditions. Then, we develop in the following section a convenient approach to compute the dispersion of PPWG conductive films.

3.3.2 *Dispersion Equations for TE and TM mode with zero thickness conductive films*

When the thickness of the materials is infinitely thin and when the material surface can support a current distribution, the current density is reduced to surface density of current [10]. From Ohm's law, the surface current density is:

$$\boldsymbol{J}_{\mathrm{S}} = \sigma_{\mathrm{S}}\boldsymbol{E}, \tag{3.32}$$

where the unit of current density is A/m and the surface or sheet conductivity is defined as :

$$\sigma_{\mathrm{S}} = \sigma_{\mathrm{C}}t, \tag{3.33}$$

where the unit of σ_{S} is S.

Now, the conductive film can be treated as singularity of the general Maxwell's equations for PPWG at $x = 0$. Therefore, rewriting Eq. (3.4) leads to [13]:

$$\nabla \times \boldsymbol{H} = -i\omega\epsilon\boldsymbol{E} + \sigma_S(x)\delta(x)\boldsymbol{E}, \tag{3.34}$$

In Eq. (3.34), $\delta(x)$ is the Dirac distribution and it should not be confounded with the skin depth. It indicates that the sheet conductivity exist only in the *y*-*z* plan at $x = 0$. In TM mode, only E_{x}, E_{z} and H_{y} exist whereas H_{x}, H_{z} and E_{y} exist in TE mode. Since there is no variation in *y*-direction and the surface current density is induced by the electric field parallel to the material surface plane, the fields are decomposed into:

$$\left.\begin{array}{r}\dfrac{\partial E_x}{\partial z} - \dfrac{\partial E_z}{\partial x} = i\omega\mu H_y \\ \dfrac{\partial H_y}{\partial z} = i\omega\epsilon E_x \\ \dfrac{\partial H_y}{\partial x} = -i\omega\epsilon E_z + \sigma_{\mathrm{S}}\delta(x)E_z\end{array}\right\}, \tag{3.35}$$

for TM mode and:

$$\left.\begin{array}{r}-\dfrac{\partial E_y}{\partial z} = i\omega\mu H_x \\ \dfrac{\partial E_y}{\partial x} = i\omega\mu H_z \\ \dfrac{\partial H_x}{\partial z} - \dfrac{\partial H_z}{\partial x} = -i\omega\epsilon E_y + \sigma_{\mathrm{S}}\delta(x)E_y\end{array}\right\}, \tag{3.36}$$

for TE mode.

After some algebra, we obtain the equations for E_{z} and H_{z} for TM and TE mode respectively:

$$\frac{\partial^2 E_z}{\partial x^2} - {k_x}^2 E_z = -\frac{i{k_x}^2}{\omega\epsilon}\sigma_S\delta(x)E_z \text{ for TM mode,} \tag{3.37}$$

$$\frac{\partial^2 H_z}{\partial x^2} - {k_x}^2 H_z = i\omega\mu\sigma_S\delta(x)H_z \text{ for TE mode,} \tag{3.38}$$

with $k_x = \sqrt{\omega^2\mu\epsilon - \gamma^2}$.

The solution of Eq.(3.37) or Eq. (3.38) can be found by looking for the field of guided wave. In the following derivation, we focus on TM mode but the procedure is the same to find the dispersion equation for TE mode.

Let's assume that E_z has the form of guided waves as in empty PPWG such that:

$$E_z(x) = \begin{Bmatrix} E_1\cos(k_x x) + E_2\sin(k_x x) & x > 0 \\ E_3\cos(k_x x) + E_4\sin(k_x x) & x < 0 \end{Bmatrix}. \tag{3.39}$$

The expression of E_z can be combined by applying the boundary condition at $x = 0$ and at $x = d/2$. The continuity of tangential electric fields gives:

$$\left.\begin{matrix} E_z(0^+) = E_z(0^-) \\ E_z(d/2) = E_z(-d/2) = 0 \end{matrix}\right\}, \tag{3.40}$$

and:

$$E_z(x) = E_1\left(\cos(k_x x) \mp \frac{\sin(k_x x)}{\tan\left(\frac{k_x d}{2}\right)}\right). \tag{3.41}$$

The sign "-" is for $x > 0$ and the sign "+" is for $x < 0$ and E_1 is a constant.

Now, let's integrate Eq. (3.37) over a small interval around the singularity $x = 0$:

$$\int_{-\xi}^{+\xi}\frac{d^2E_z(x)}{dx^2}dx - {k_x}^2\int_{-\xi}^{+\xi}E_z(x)dx = \int_{-\xi}^{+\xi} -\frac{i{k_x}^2}{\omega\epsilon}\sigma_S\delta(x)E_z(x)dx, \tag{3.42}$$

where the Dirac δ – function, for any smooth function $f(x)$, implies $\int\delta(x)f(x)dx = f(0)$. When $\xi\to 0$, $\lim_{\xi\to 0}{k_x}^2\int_{-\xi}^{+\xi}E_z(x)dx \to 0$. The remaining terms are:

$$\lim_{\xi\to 0}\frac{dE_x(x)}{dx}\bigg|_{-\xi}^{+\xi} = -\frac{i{k_x}^2}{\omega\epsilon}\sigma_S E_z(0). \tag{3.43}$$

From Eq. (3.41), $E_z(0) = E_1$ and the dispersion equation for TM mode is:

$$\sigma_S = \frac{i2\omega\epsilon}{k_x}\cot\left(\frac{k_x d}{2}\right). \tag{3.44}$$

By performing the same analysis with Eq. (3.38) for TE mode, the dispersion equation is:

$$\sigma_{\mathrm{S}} = \frac{i2k_x}{\omega\mu}\cot\left(\frac{k_x d}{2}\right). \tag{3.45}$$

Eqs. (3.44) - (3.45) express the contribution of the thin conductive film to the complex propagation constant γ in Eq. (3.28). Conversely, if the complex propagation constant is know the sheet conductivity of the material in between the PPWG can be extracted.

Eqs. (3.44) and (3.45) are my main theoretical contribution in this new geometry of ultrathin films inside a PPWG for two-dimensional conductive materials characterization in THz range [14].

In our derivation of the two dispersion equations, the manner we have chosen is not the only way to compute the propagation constant in function of the sheet conductivity. In fact, by applying the discontinuity of magnetic field due to the surface current density such that:

$$\boldsymbol{n} \times (\boldsymbol{H}_1 - \boldsymbol{H}_2) = \sigma_S \boldsymbol{E}, \tag{3.46}$$

where $\boldsymbol{n}$ is an unit vector normal to the conductive layer interface pointing from region 1 to region 2, we end up exactly to the same equations of Eqs. (3.44) - (3.45). Another way to start is also by considering the boundary conditions about the discontinuity of the displacement field Eq. (3.1) and subsequently applying the charge conservation $\nabla \boldsymbol{J}_{\mathrm{S}} + \frac{\partial \rho_{\mathrm{S}}}{\partial t} = 0$.

3.4 QUASI – OPTICAL COUPLING AND COMPLEX TRANSFER FUNCTION

3.4.1 *Quasi-optical coupling*

The technique of quasi-optical coupling has been intensively developed for microwave and millimeter-wave optics. Number of literatures is devoted to that topic especially in Ref. [15] and Ref. [16]. Gallot et *al*. [3] provide detailed description quasi-optical coupling applied to THz waveguides but here, we only develop the general idea and especially applied to PPWG.

It is well known that any incident electromagnetic field and output electromagnetic field from waveguide can be expanded into electric and magnetic fields of the modes [17]. This assumption is based on the orthogonality of guided modes. In general, there are evanescent (non-guided) and guided mode and the orthogonality relation should take account of both modes. However, in practice, only the guided mode solutions of Maxwell's equations are considered. The continuity of the transverse fields at the input face of the waveguide gives [17]:

$$\left.\begin{aligned} \boldsymbol{E}_{\mathrm{t,inc}} &= \textstyle\sum_m (\mathrm{a_m} + \mathrm{b_m})\, \boldsymbol{E}_{\mathrm{tm}} \\ \boldsymbol{H}_{\mathrm{t,inc}} &= \textstyle\sum_m (\mathrm{a_m} - \mathrm{b_m})\, \boldsymbol{H}_{\mathrm{tm}} \end{aligned}\right\}, \tag{3.47}$$

a_m and b_m are the coefficients to be determined, $\boldsymbol{E}_{tm}$ and $\boldsymbol{H}_{tm}$ are the transverse electric and magnetic fields of the guided mode and $\boldsymbol{E}_{t,inc}$ and $\boldsymbol{H}_{t,inc}$ are the electric and magnetic fields of the THz incident fields at the input of the waveguide.

Using the well-known orthogonality of modes in waveguide with perfect conducting wall and the normalization $\int_S (1/Z)\,|\boldsymbol{E}_{\mathrm{tm}}|^2 \mathrm{d}S = 1$ where Z is the wave impedance in Eq. (3.14) for TM or TE mode, we have:

$$\left.\begin{aligned} \mathrm{a_m} + \mathrm{b_m} &= \frac{1}{Z}\int \boldsymbol{E}_{\mathrm{t,inc}}\boldsymbol{E}_{\mathrm{tm}}dS \\ \mathrm{a_m} - \mathrm{b_m} &= \int \boldsymbol{H}_{\mathrm{t,inc}}\boldsymbol{H}_{\mathrm{tm}}dS \end{aligned}\right\}, \tag{3.48}$$

It is also possible to express the output field by expanding the field in normal modes of PPWG. By taking account of mismatch between the impedance of input and output media to the impedance of waveguide modes (TM or TE mode given by Eq. (3.14)), the electric output field is [3]:

$$\begin{aligned} &E_{\mathrm{out}}(\omega, t) \\ &= E_{\mathrm{inc}}(\omega, t)\sum_m \frac{2Z(\omega)}{Z_{\mathrm{inc}} + Z(\omega)}\frac{2Z_{\mathrm{out}}}{Z_{\mathrm{out}} + Z(\omega)} C_{x,\mathrm{in}}\, C_{x,\mathrm{out}} {C_y}^2 e^{i\gamma_m(\omega)z - i\omega t}, \end{aligned} \tag{3.49}$$

Usually the output and input region are the free space so that $Z_{\mathrm{inc}} = Z_{\mathrm{out}} = Z_0$. $E_{\mathrm{inc}}(\omega, t)$ is the time – frequency dependent input field. Here, the coupling coefficients $C_{x,\mathrm{in}}$, $C_{x,\mathrm{out}}$, C_y depend on the normalized mode and the profile of input and output beam. Since the waveguide is uniform in y, the coupling coefficient C_y are the same for the input and the output. If the propagated modes are not much altered at the output, for example in a relatively short waveguide, the input and output coupling coefficients in x are approximately the same, $C_{x,\mathrm{in}} \approx C_{x,\mathrm{out}}$. For THz wave, a good approximation of the spatial input and output beam is a Gaussian spatial profile. For example, suppose a normalized Gaussian input field such as:

$$E_{\mathrm{inc}}(x) = \left(\frac{2}{\pi {\omega_0}^2}\right)^{1/4} e^{-(x/\omega_0)^2}, \tag{3.50}$$

where ω_0 is the beam waist of the incoming THz beam. Here, only the x – dependence is required since the PPWG is uniform in y. The input coupling coefficient with a normalized TM mode of empty PPWG is:

$${C_{x,\mathrm{in}}}^{\mathrm{TM}} = \left(\frac{2}{\pi}\right)^{1/4} (\omega_0 d/2)^{-1/2} \int_0^d e^{-\left((x - {d}/{2})/\omega_0\right)^2} \cos\left(\frac{\mathrm{m}\pi}{d}x\right) dx\,, \tag{3.51}$$

when the mode number is odd (TM_1, TM_3, TM_5…), the integral is zero and then, only the even mode is excited (TEM, TM_2, TM_4…).

For TE mode, the input coupling coefficient is:

$$C_{x,\text{in}}{}^{\text{TE}} = \left(\frac{2}{\pi}\right)^{1/4} (\omega_0 d/2)^{-1/2} \int_0^d e^{-\left(\left(x-{}^{d}/_{2}\right)/\omega_0\right)^2} \sin\left(\frac{\text{m}\pi}{d} x\right) dx, \tag{3.52}$$

Here, only odd modes are excited with the fundamental mode TE_1.

Fig. 3.4 illustrates the coupling coefficients of TM and TE modes as a function of ω_0/d. We can make use of this Fig. to match the beam waist and the PPWG plate separation. In TE mode, when $\omega_0/d = 0.38$, only the fundamental mode TE_1 couple with the input beam and higher modes are not excited. The coupling coefficient reaches 99%. In TM mode, the maximum coupling of appears at $\omega_0/d = 0.5$. The coupling coefficient of TEM mode attains 89%.

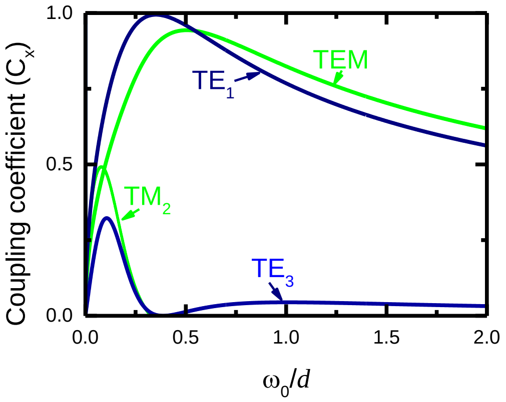

Fig. 3.4 Coupling coefficients in *x*- direction with respect to the ratio between the waist (ω_0) and the plate separation (*d*). The coupling coefficients are calculated from Eqs (3.51) and (3.52)

The coupling coefficients of PPWG with thin conductive film could be also evaluated in the same manner by replacing the expression of electric field of guided mode. In general, Eq. (3.38) dictates the THz free- space coupling to all sort of waveguide.

3.4.2 *Transfer function*

As we saw in Chapter.2, it's the complex time domain electric field that is detected. Then, from the first equation of Eq.(3.5), the electric field at *z* is:

$$e^{-i\omega t}\text{E}(x, y, z, \omega) = E(x, y, 0, \omega)e^{i\gamma(\omega)-i\omega t}. \tag{3.53}$$

The form of Eq. (3.53) is equivalent to the output of linear system similar to conventional THz-TDS where:

$$E_{\mathrm{out}}(\omega) = H(\omega) E_{\mathrm{input}}(\omega). \tag{3.54}$$

If the input electric field is the incoming THz beam, from the field expansion in Eq.(3.49), the transfer function of the empty PPWG is:

$$H_0(\omega) = \sum_{\mathrm{m}}^{\mathrm{TM,TE}} t_{\mathrm{WG,m}}(\omega) C_{\mathrm{WG,m}}(\omega) exp\left(i\gamma_{\mathrm{WG,m}}(\omega)\right), \tag{3.55}$$

where $t_{WG,m}(\omega)$ is the equivalent Fresnel coefficients of PPWG mode and $C_{WG,m}(\omega)$ is the coupling coefficient of mode m to the incoming beam. $\gamma_m(\omega)$ is the complex propagation constant of the mode m indicating the dispersion and the attenuation.
Similarly, the transfer function for a PPWG with ultrathin film is:

$$H_1(\omega) = \sum_{\mathrm{n}}^{\mathrm{TM,TE}} t_{\mathrm{WG+film,n}}(\omega) C_{\mathrm{WG+film,n}}(\omega) exp\left(i\gamma_{\mathrm{WG+film,n}}(\omega)\right). \tag{3.56}$$

From the above equation, we can define the relative transfer function which relates an empty waveguide to the waveguide with thin film:

$$T(\omega) = \frac{\sum_{\mathrm{n}}^{\mathrm{TM,TE}} t_{\mathrm{WG+film,n}}(\omega) C_{\mathrm{WG+film,n}}(\omega) exp\left(i\gamma_{\mathrm{WG+film,n}}(\omega)\right)}{\sum_{\mathrm{m}}^{\mathrm{TM,TE}} t_{\mathrm{WG,m}}(\omega) C_{\mathrm{WG,m}}(\omega) exp\left(i\gamma_{\mathrm{WG,m}}(\omega)\right)}. \tag{3.57}$$

Either Eq. (3.56) or (3.57) can be chosen to compute the propagation constant. However, for experimental convenience, Eq (3.57) will be used.

3.5 PARAMETERS EXTRACTION

In the preceding sections has been described the main theoretical framework about the characterization of thin conductive films inserted in PPWG. The main purpose of the work is nevertheless to extract the optical parameters of the materials. In this section, we attempt to construct a standard parameters extraction for ultrathin conductive films in the frame of THz spectroscopy.

We have seen that for ultrathin conductive layers, the optical parameters are mainly the sheet conductivity. So the first task to conduct is modelling the conductivity of the analyzed samples. That model depends on sample and can be completely different from one to another. But for now, let’s assume that the complex conductivity depends on physical parameters constant p_{i} (i = 1, 2…) such that:

$$\sigma_S(\omega) = f(\omega, p_1, p_2, \dots), \tag{3.58}$$

where p_i are the unknown and can be plasma frequency, time scattering, etc. Here, we assume that the thickness of the film is already known.

The first step in the extraction process is to obtain the experimental complex value of relative transmission similar to that of conventional THz-TDS (Eq. (2.2)). The reference signal is obtained from the empty PPWG and the sample signal from the PPWG with thin film. TM and TE mode analysis is separated since in the experiment TM and TE mode can be excited independently. This experimental result is compared to the theoretical relative transmission Eq.(3.57). The optimization minimizes the difference of both transmission:

$$\begin{aligned} \mathrm{err} &= \sum_{\omega}^{\mathrm{MODE}} \left|T_{\mathrm{Theory}}(\omega) - T_{\mathrm{experiment}}(\omega)\right| \\ &= \sum_{\omega}^{\mathrm{MODE}} \left|\left|T_{\mathrm{Theory}}(\omega)\right| - \left|T_{\mathrm{experiment}}(\omega)\right|\right| \\ &\qquad + \left|\arg\left(T_{\mathrm{Theory}}(\omega)\right) - \arg\left(T_{\mathrm{experiment}}(\omega)\right)\right|. \end{aligned} \tag{3.59}$$

Therefore, given the initial value p_i (0) of the free parameters p_i, we can calculate the complex propagation constant via Eq. (3.27) for TEM mode and via Eqs. (3.44) - (3.45) TM and TE modes, respectively. The transcendental equations have infinite discrete solutions (modes) but the expressions presented in section 3.3 do not reveal that multiplicity of solution. It is convenient to convert the dispersion equations Eq. (3.44) - (3.45) to the following iterative forms [18]:

$$\gamma_{\mathrm{n+1}}{}^{\mathrm{WG+film}} = \left[\omega^2\epsilon\mu - \frac{2}{d}\left[\mathrm{m}\pi - \tan^{-1}\left(\frac{2\sqrt{\omega^2\epsilon\mu - {\gamma_n}^2}}{i\mu\omega\sigma_\mathrm{S}(\omega, p_\mathrm{i})}\right)\right]\right]^{1/2} \text{(TE)}, \tag{3.60}$$

$$\gamma_{\mathrm{n+1}}{}^{\mathrm{WG+film}} = \left[\omega^2\epsilon\mu - \frac{2}{d}\left[\mathrm{m}\pi - \tan^{-1}\left(\frac{2\omega\epsilon}{i\sigma_\mathrm{S}(\omega, p_\mathrm{i})\sqrt{\omega^2\epsilon\mu - {\gamma_n}^2}}\right)\right]\right]^{1/2} \text{(TM)}. \tag{3.61}$$

The expression above is much stable and convenient to implement in numerical computation. For TEM mode, a built-in algorithm as “fsolve” function type in Matlab software is used to find the propagation constant. This built - in function solves non-linear problem and is well adapted for Eq. (3.27). The propagation constant for empty waveguide is calculated by means of Eq. (3.17) with $\gamma^{\mathrm{TEM}} = \omega\sqrt{\epsilon\mu}$.

Once the complex propagation constant of the mode m (either TM or TE modes) of empty PPWG and PPWG with thin film are found, $t_{\mathrm{WG+film,n}}(\omega)$ and $t_{\mathrm{WG,m}}(\omega)$ are computed via Eq. (3.14). Then, the last terms left in $T_{\mathrm{Theory}}(\omega)$ are the coupling coefficient $C_{\mathrm{WG+film,n}}(\omega)$

and $C_{\mathrm{WG,m}}(\omega)$. The incoming THz beam is approximated by Eq. (3.50) with the frequency depend beam waist radius [14]:

$$\omega_0 \approx \frac{2\lambda_{\mathrm{THz}}}{\pi} F, \tag{3.62}$$

where λ_{THz} is the wavelength of THz incident beam and F is F-number of the focusing optics before the waveguide. The F-number parameters depends on the arrangement of optical system that we will discuss in detail in chapter 4.

The generalized form of the coupling coefficients takes the form:

$$C_m = \int_S E_{\mathrm{inc}} E_{\mathrm{Mode}} dS\,, \tag{3.63}$$

with E_{inc} is the normalized electric field of the incident field and E_{Mode} is the normalized electric field of the mode for TM or TE mode in the empty PPWG or in the PPWG with thin film. S is the cross section of the waveguide. The coupling coefficients for empty PPWG are calculated from Eq. (3.51) - (3.52) . The normalized transverse electric fields for PPWG with thin films are derived from Eq. (3.41) for TM mode and similar expression for TE mode, so that:

$$\begin{aligned} E_x &= \sqrt{\frac{d}{4}} \cos\left[k_x\left(\frac{d}{2} \mp x\right)\right] \quad \text{(TM)}, \\ E_y &= \sqrt{\frac{d}{4}} \sin\left[k_x\left(\frac{d}{2} \mp x\right)\right] \quad \text{(TE)}. \end{aligned} \tag{3.64}$$

Now that all parameters of $T_{\mathrm{Theory}}(\omega)$ can be evaluated, the optimization is made through the free parameters p_{i}. Additionally, in some case that will be described later, the waist of the incoming beam cannot be estimated accurately since it is frequency dependent parameters, so ω_0 can be accounted as free parameters.

Fig. 3.5 summarizes the flowchart of the parameters extraction algorithms. The programming code is written in MATLAB software with the built-in Global optimization toolbox.

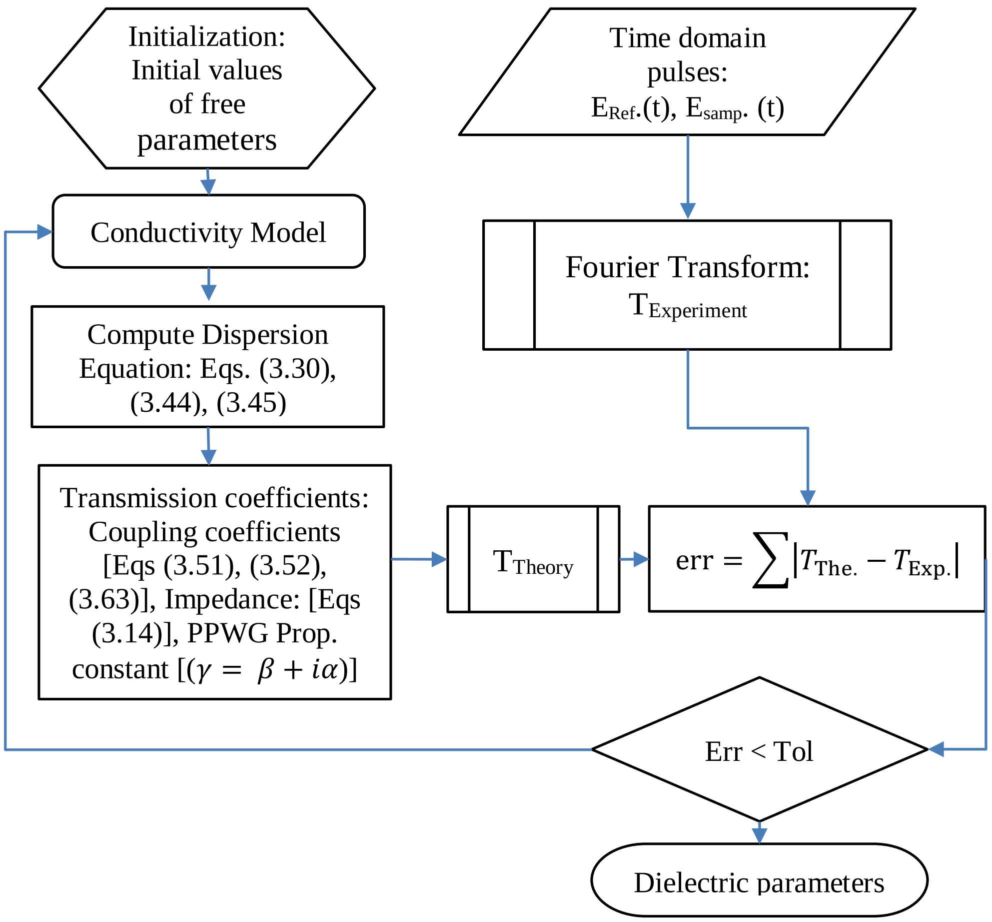

Fig. 3.5 Flowchart of Parameter extraction algorithm. The Program code for computation are written in MATLAB using Global optimization toolbox.

3.6 CONCLUSION

In this chapter, we have developed the theoretical framework of ultrathin conductive film located halfway between the plates of PPWG. Starting from the classical PPWG theory, we derived the dispersion equations, in case of ultrathin conductive film loading symmetrically the waveguide for transverse magnetic and transverse electric mode [14]. These dispersion equations will be used to compute the electromagnetic properties of the samples under investigation by means of the sheet conductivity σ_S.

In case of antisymmetric of longitudinal electric field E_z profile, the derived dispersion equation was expressed by Eq. (3.30):

$$k_{x1} \tan\left(k_{x1}\left(\frac{d-t}{2}\right)\right) \approx \frac{(1+i)\epsilon\omega}{\delta\sigma_C} \tan\left(i(i+1)\frac{t}{2\delta}\right), \tag{3.30}$$

where δ is the skin depth, t is the conductive film thickness and σ_C is the conductivity of the materials. When the thickness is far below the skin depth (t << δ) or the thin film is highly conductive ($\sigma_C \rightarrow \infty$), the dispersion equation Eq. (3.30) becomes the equation for the fundamental TEM mode of empty PPWG. In other words, the contribution of thin film to the propagation of the antisymmetric mode is nearly negligible.

In the case of symmetric electric field component which is parallel to the thin film surface plane (E_z and E_y for TM and TE mode, respectively), we transformed the boundary value problem to homogeneous equations by introducing into the Maxwell's equations the Dirac distribution δ (x) as the singularity representing the ultrathin conductive layer. From that, we derived the dispersions equations for higher order TM and TE modes by Eqs. (3.44) and (3.45):

$$\sigma_S = \frac{i2\omega\epsilon}{k_x}\cot\left(\frac{k_x d}{2}\right), \tag{3.44}$$

$$\sigma_S = \frac{i2k_x}{\omega\mu}\cot\left(\frac{k_x d}{2}\right). \tag{3.45}$$

In THz-PPWG-TDS experiment, the time domain data collected can be converted in a straightforward manner to frequency – dependent transmission amplitude and transmission phase by numerical Fast Fourier Transform algorithm. The amplitude and the phase are related to the complex -valued THz wave propagation constant γ, and thus related to the sheet conductivity. The evaluation of the transmission is relatively simple when single mode propagation (TM or TE mode) is realized. In previous work relating to PPWG in THz range (for example in [6]), one always consider the single mode propagation using TEM mode. Here, we have extended the analysis to multimode propagation of the TM and additionally TE modes in Eq. (3.57) [14]. Then, we developed a generalized optimization algorithm to extract the electromagnetic parameters. In the process, the free parameters are mainly the physical constants in the chosen conductivity model of the samples prototype. The number of propagating modes can be adjusted during the optimization, either for the reference signal (for example THz transmitted through PPWG with only dielectric substrates) or for the sample signal (THz transmitted through PPWG with ultrathin conductive films).

REFERENCES:

[1]. M. Skorobogatiy, “Nanostructured and Subwavelength Waveguides: Fundamentals and Applications,” Wiley, 2012.

[2]. R. W. McGowan, G. Gallot, and D. Grischkowsky, “Propagation of ultrawideband short pulses of terahertz radiation through submillimeter-diameter circular waveguides.,” *Opt. Lett.*, vol. 24, no. 20, pp. 1431–3, 1999.

[3]. G. Gallot, G. Gallot, S. P. Jamison, S. P. Jamison, R. W. Mcgowan, R. W. Mcgowan, D. Grischkowsky, and D. Grischkowsky, “Terahertz waveguides,” *J. Opt. Soc. Am. B.*, vol. 17, no. 5, pp. 851–863, 2000.

[4]. K. Wang and D. Mittleman, “Metal wires for terahertz wave guiding,” *Nature*, vol. 432, pp. 376–379, 2004.

[5]. R. Mendis and D. Grischkowsky, “Undistorted guided-wave propagation of subpicosecond terahertz pulses.,” *Opt. Lett.*, vol. 26, no. 11, pp. 846–848, 2001.

[6]. Zhang and D. Grischkowsky, “Waveguide terahertz time-domain spectroscopy of nanometer water layers.,” *Opt. Lett.*, vol. 29, no. 14, pp. 1617–1619, 2004.

[7]. R. Mendis and D. M. Mittleman, “An investigation of the lowest-order transverse-electric (TE1) mode of the parallel-plate waveguide for THz pulse propagation,” *J. Opt. Soc. Am. B-.*, vol. 26, no. 9, pp. A6–A13, 2009.

[8]. R. Mendis, V. Astley, J. Liu, and D. M. Mittleman, “Terahertz microfluidic sensor based on a parallel-plate waveguide resonant cavity,” *Appl. Phys. Lett.*, vol. 95, no. 17, pp. 1–4, 2009.

[9]. S. Ramo, “Fields and waves in communication electronics,”. J. Wiley, 2008.

[10]. F. Wegner, “Classical Electrodynamics,” *Nature*, vol. 224, pp. 1334–1334, 1969.

[11]. D. R. Lide, “CRC Handbook of Chemistry and Physics,” p. 71, 2005.

[12]. R. E. Collin, “Field theory of guided waves (2nd edition),” Wiley - IEEE press, 1990.

[13]. M. Mithat Idemen, "Discontinuities in the electromagnetic field," Wiley - IEEE press, 2001

[14]. M Razanoelina, R. Kinjo, K. Takayama, I. Kawayama, H. Murakami, D. Mittleman, M. Tonouchi, “Parallel-Plate Waveguide Terahertz Time Domain Spectroscopy for Ultrathin Conductive Films”, *J. Infrared Milli and Terahz Waves* , vol. 36, no. 12, pp 1182-1194, 2015

[15]. J. Lesurf, “Millimetre-wave optics, devices and systems,” CRC Press, 1990.

[16]. K. J. Button, “Quasioptical Techniques at Millimeter and Submillimeter Wavelengths,” *Infrared Millim. Waves V6 Syst. Components*, vol. 6, pp. 277–344,

1983.

[17]. J. C. Slater, “Microwave Electronics,” Rev. Mod. Phys., vol. 18, no. 4, p. 441, 1946.

[18]. R. D. Kekatpure, A. C. Hryciw, E. S. Barnard, and M. L. Brongersma, “Solving dielectric and plasmonic waveguide dispersion relations on a pocket calculator.,” Opt. Express, vol. 17, no. 26, pp. 24112–24129, 2009.

Chapter 4. CONSTRUCTION OF EXPERIMENTAL SYSTEM FOR TERAHERTZ PARALLEL PLATE WAVEGUIDE–TIME DOMAIN SPECTROSCOPY

4.1 INTRODUCTION

Nowadays, commercial conventional THz-TDS systems are widely available and their performance rapidly increases. The experimental techniques of THz-TDS attains certain degree of maturity due to numerous research in this field. However, the principles of the technique remains relatively the same since its first realization[1, 2] .The most used THz-TDS techniques is transmission type in which the THz beam probes the sample by traveling through it. The setup is based on THz emitter, THz detector and an arrangement of optical system for free space coupling to the sample.

THz generation and detection can be done by different methods associated with different physical mechanism. Amidst these approaches, generation and detection of THz by photoconductive (PC) sources [3] and generation by semiconductor surfaces are included [4]. In a standard THz TDS setup, PC antennas generate and detect coherently the pulse signal. However, the THz pulse is polarized with PC antenna while the excitation of TM and TE modes requires different polarization of the incoming beam. Therefore, we use semiconductor surfaces of indium arsenide (InAs) for generation of THz radiation and photoconductive antenna of low temperature grown gallium arsenide (LT-GaAs) for detection. The optical system inherits from the combination of millimeter-wave and optical wave techniques. For example, parabolic mirrors and lenses are used to shape the THz beam. Parabolic mirrors are largely employed in millimeter wave while lenses are more utilized in visible optics. Here, we will make use of parabolic mirrors and silicon lens to collimate and to focus the THz beam in and out of the waveguide and also into the detector.

The outline of this chapter is as follows: section 2 describes the THz emitter employed in the setup. Then section 3 explains the THz detection mechanism with PC antenna. Section 4 provides the detail of the quasi-optical coupling arrangement. Section 5 gives a description of the

PPWG and the process of experimental data recording. The last section concludes this chapter by summarizing the experimental setup used in this work.

4.2 THZ EMISSION

The principles of THz emission from semiconductor surface is based on photoexcitation of carriers by ultrafast optical pulses [5]. When bulk semiconductors surfaces are excited by ultrashort laser pulses, two mechanisms govern the THz generation: nonlinear process or optical rectification and the ultrafast charge transport or ultrafast surface surge-current [6, 7]. The generation of THz pulses originating from the latter optical process includes surface-depletion field and the photo-Dember mechanism. Here, the nonlinear effects are not significant for the crystal orientation of the emitter such that the dominant mechanism is from surge current.

A mode-locked femtosecond laser Mai tai (Spectra Physics, Ti: sapphire laser) delivers a near infrared optical pulses at a wavelength of 800 nm and a repetition rate of 80MHz. The pulse width of the laser is less than 80 fs with a maximum power of 2W. The laser with a power about 90mW is focused on the surface of holes doped (p-type) indium arsenide (InAs) wafer. The penetration depth of the excitation pulse is relatively small (hundreds of nanometers at 800 nm) leading to a large excess of energy of the excited carriers. It is well known that in this situation, the main relevant mechanism for THz generation in narrow-band gap semiconductors is the photo-Dember effect [8]. Fig. 4.1 illustrates the THz-wave generation mechanism near the surface narrow band semiconductor. The photo-Dember field is primarily due to the difference of diffusion of photoexcited carriers into the bulk semiconductor. The difference between the diffusion of electrons and holes in a typical semiconductor create a current or voltage. The orientation of the dipole is normal to the surface of the semiconductors. From the classical definition, the diffuse currents of electron and holes can be expressed as follow [8]:

$$\left.\begin{aligned} J_{\mathrm{e}} &\propto -eD_{\mathrm{e}}\frac{\partial n}{\partial z} \\ J_{\mathrm{h}} &\propto +eD_{\mathrm{h}}\frac{\partial p}{\partial z} \end{aligned}\right\}, \tag{4.1}$$

where e is the electron charge, n and p are the concentration of photogenerated electrons and holes. D_e and D_h are the diffusion coefficient defined by the Einstein relation $D = k_B T\mu/e$ where k_B, T and μ are the Boltzmann constant, the temperature and the carriers mobility, respectively. Since the mobility of electrons are much larger than the mobility of the holes, the diffuse currents of the holes can be neglected. Furthermore, the photo Dember current has a fixed direction and then the polarity of the THz pulses emitted does not depend on the type of doping. The electric field emitted from the surface of InAs is approximately [4]:

$$E_{\mathrm{THz}} \propto \frac{\partial J_{\mathrm{e}}}{\partial t}. \tag{4.2}$$

In order to out-couple the generated THz to free space, the InAs emitter is rotated 45° with respect to the laser beam axis. Fig. 4.2 shows a typical time domain pulse of THz wave generated by p-type InAs detected in the far field. We can monitor the strength of the electric field by changing the power of the excitation laser. To that purpose, a variable neutral density filter is placed before the emitter. The maximum power available for the laser pump pulse is around 110mW in our setup. This power is largely enough for all type of experiment we conduct.

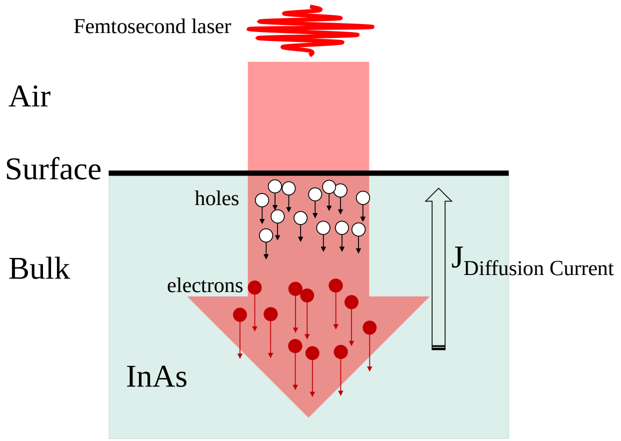

Fig. 4.1 Schematic of photo Dember effect near the interface between airs – InAs. Carriers are excited near the surface, inducing a diffusion current that is responsible for THz generation.

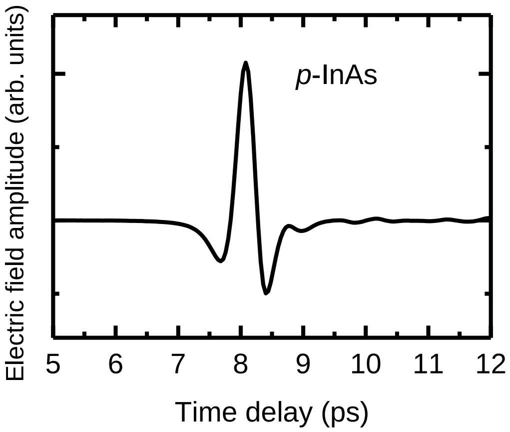

Fig. 4.2 Time domain THz pulse electric field generated by semiconductor p – InAs surface.

4.3 THz DETECTION

The detection of THz radiation is realized by low-temperature grown gallium arsenide (LT-GaAs) photoconductive antenna (PCA). LT-GaAs is usually chosen for the THz detection because of it has a short carrier lifetime (0.3 ps), relative high resistivity (10^6 Ωcm) and relative high mobility (>150 $cm^2/(Vs)$) [4].. Fig. 4.3 show the design of LT-GaAs used in the experimental setup. The PCA structure consists of an electrode antenna structure on a LT-GaAs. The substrate (semi-insulating GaAs: SI-GaAs) and a silicon lens are coupled to focus the THz wave. The electrodes are fabricated in the back of the substrate and are made of gold coplanar line and dipole antenna. The gap between the dipole antennas is about 5 μm. The whole structure is fixed behind a hyperhemispherical silicon lens. The refractive indices of silicon and GaAs are quite similar (~3.42) [9] such that the arrangement minimize the reflection. The shape of the silicon lens decreases the Gaussicity of the beam and increases the sidelobes [10].

The same ultrashort laser from Ti: sapphire illuminates the gap between the dipole with a power about 5.5mW. This laser is optically chopped at 2 kHz for synchronous detection and in order to eliminate background noise. The optical probe beam excites carriers which have generally a lifetime shorter than the THz pulse. When the gap is not illuminated by the laser, there is no current flowing down the transmission line of the antenna. When the laser illuminates the gap, the resistance of LT-GaAs decreases to a minimum resistance. Therefore, when the THz radiations arrive to the detector, the excited carriers are driven by the THz electric field. The photocurrents are proportional to the magnitude of the THz electric field and can be amplified by an external low-noise current amplifier. This current amplifier is subsequently coupled to a lock-in amplifier which is locked to the frequency of the chopper. It should be noticed that the receiver detect only the THz electric field with a polarization perpendicular to the gap.

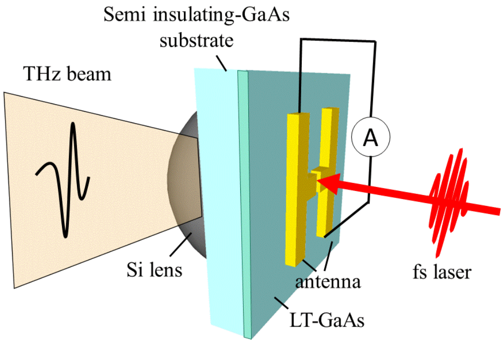

Fig. 4.3 Schematic of dipole-type photoconductive switch for THz receiver. The detector is gated by the same femtosecond laser for the source. The silicon lens focus the THz beam which drives the transient current and subsequently amplified.

The Fig. of merit of our detector can be determined by two factors. The first is the frequency bandwidth that can be detected and the second is the signal to noise ratio. The overall performance of the experimental setup depends mainly on the detector. For example, Fourier transform of the pulse in Fig. 4.1 gives the spectrum in Fig. 4.4. It is shown that the bandwidth can reach 3.6 THz with the system purged with nitrogen atmosphere. We have about 3 order-of-magnitude SNR at the frequency peak of the spectrum.

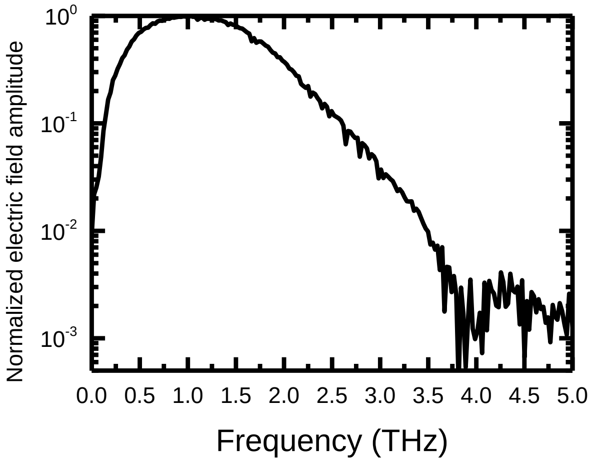

Fig. 4.4 Fourier transform of the THz pulse in Fig. 4.2 detected by PC antenna. The measurement was under nitrogen atmosphere. The spectrum amplitude is in log scale.

4.4 FREE SPACE QUASI OPTICAL TECHNIQUE

4.4.1 *Parabolic mirrors*

In THz-TDS, the most used focusing elements to couple the emitted wave to the free space and to focus it to the detector are off-axis parabolic mirrors. When the samples under analysis are big enough such that small focused beam is not required, only two parabolic mirrors are employed. A first parabolic mirror is to collimate the beam and a second parabolic mirror is focus the beam to the detector. Therefore, the sample can be placed between those two mirrors. When the available samples are small enough, four parabolic mirrors can be combined or alternatively, parabolic mirrors and THz lenses can be utilized. Here, since the PPWG plate separation is about 1 mm (~$3\lambda_{1THz}$), a small incoming beam spot is required in order to efficiently couple the THz wave to PPWG.

In chapter.3, we have already assumed that the THz wave has a spatial Gaussian profile [11]. To take account of diffractions, beam coupling, beam truncation and other effects of complex optical system, higher order beam modes solution should be considered. However, in most of THz-TDS system, the approximation of simple Gaussian profile is sufficient. Then, suppose that a THz Gaussian beam with waist $\omega_{0,1}$ located at a distance L_1 is transformed by a thin lens (or any focusing elements) with a focal length f_1 to a beam with waist $\omega_{0,2}$ at distance L_2 after the lens (Fig. 4.5). The transformation matrix associated with the system is [12]:

$$\mathrm{M} = \begin{pmatrix} 1-\dfrac{L_2}{f_1} & L_1+L_2\left(1-\dfrac{L_1}{f_1}\right) \\ -\dfrac{1}{f_1} & 1-\dfrac{L_1}{f_1} \end{pmatrix} \tag{4.3}$$

The matrix Eq. (4.3) transforms the Gaussian beam and gives the beam waist and the location in the region after the lens:

$$\frac{L_2}{f_1} = 1 + \left(\frac{L_1/f_1 - 1}{{z_c}^2/{f_1}^2 + (L_1/f_1 - 1)^2} \right) \tag{4.4}$$

$$\omega_{0,2} = \frac{\omega_{0,1}}{\left[{z_c}^2/{f_1}^2 + (L_1/f_1 - 1)^2\right]^{1/2}} \tag{4.5}$$

where $z_c = \pi\omega_{0,1}/\lambda_{\mathrm{THz}}$ is called the confocal distance. Therefore, for a beam source situated at $L_1 = f_1$, the output beam with a waist $\omega_{0,2} = f_1\lambda_{\mathrm{THz}}/\pi\omega_{0,1}$ is located at distance $L_2 = f_1$.

For a collimated beam of radius with a radius equal the radius of a parabolic mirror of focal length f_1 and diameter section D, the output beam spot radius is:

$$W_0 = \omega_{0,2} = \frac{\lambda_{\mathrm{THz}} f_1}{\pi(D/2)} = \frac{2\lambda_{\mathrm{THz}}}{\pi} F, \tag{4.6}$$

which is the same as Eq. (3.62) where $F = f_1/D$ is the F-number of the parabolic mirror. Therefore, in order to obtain a small focused beam spot, a focusing element with small F-number should be used.

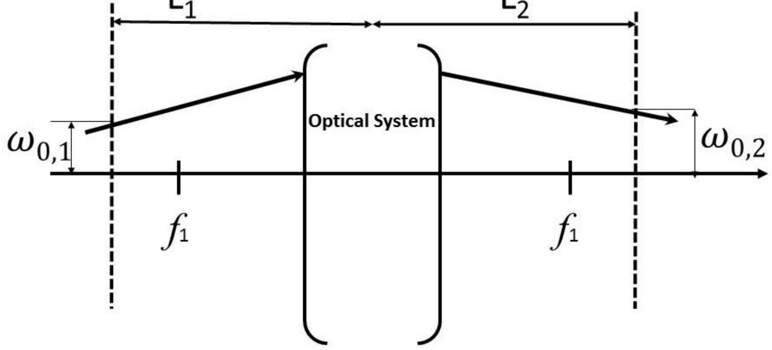

Fig. 4.5 Beam transformation by an optical system.

During the realization of this work, we have fabricated almost similar systems based exactly on the same principle. The difference between the first and the second experimental setup is only the focal length of the focusing parabolic mirrors before and after the PPWG. For example, Fig. 4.6 shows the four parabolic mirrors arrangement in the second experimental setup. All parabolic mirrors have a diameters of 50.8 mm. The first and the last parabolic mirrors have a focal length $f_1 = f_4$=50.8 mm. The first parabolic mirror collimates the beam from the InAs emitter. The emitter is placed at the focal point of the mirror so as to provide a collimated beam with nearly constant radius. This beam is focused by the second parabolic mirror with a focal length f_2 = 152.4 mm. Then the F-number of the second mirror is 3. At the lower frequency of the spectrum, for example $f = 0.1$ THz, the focused beam spot radius is 5.7 mm which is quite large compared to 1 mm plate separation of the PPWG. A third parabolic mirror which has the same characteristics as the second one collimates again the beam to the last mirror. The latter one serves to focus the THz radiation to the detector which is set at the focal point.

For the first experimental system, f_2 = f_3 = 76.2 mm and we can apply the above analysis to calculate the Rayleigh range or the F – number, etc. This first setup has been used for gold ultrathin film and the second setup has been used for the remaining applications.

It should be noticed that, in practice, the most challenging in setting up a THz-TDS system is the alignment of the optical system. An optimized experimental system is a well – aligned system. Since THz is not a visible light, the reflected laser form the surface of the InAs is usually served for a primary alignment. The fine adjustment is done with three dimensional micrometer precision mechanical stage.

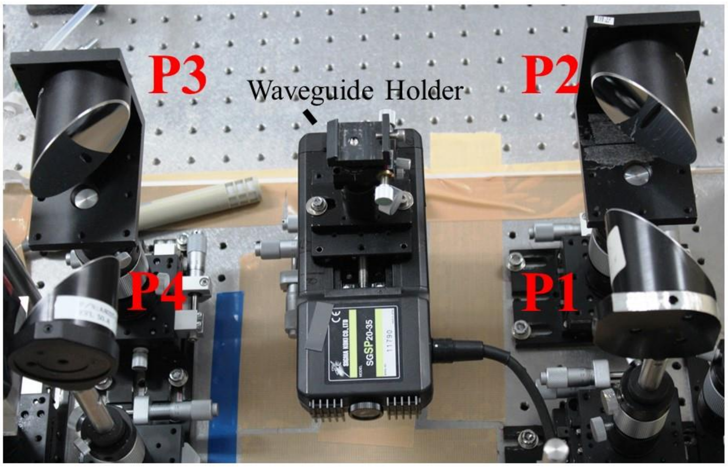

Fig. 4.6 Four parabolic mirror system used in this work. P1 collects the generated THz and P4 focuses it to the receiver. P2 and P3 are used to focus the beam into and out of the PPWG. The translation stage in the center is for the PPWG.

4.4.2 *Wire grid polarizer*

We have seen that the electric field of TM and TE mode of PPWG has different orientation with respect to the plates of the waveguide. The polarization direction of the electric field of the fundamental TEM mode is oriented perpendicular to the PPWG plates while that of the fundamental TE_1 mode is oriented parallel to the waveguide plates. Different electric field polarization is required to excite either TM mode or TE mode. However, the LT-GaAs antenna detects only one polarization which is determined by its dipole antenna orientation. In consequence, we should polarize the THz beam before the waveguide and also transform the beam polarization out of the waveguide. To that purpose, we use THz wire grid polarizers which have a high transmittance in THz range.

As indicated below, the polarization of the excitation beam is controlled by a wire grid $W.G_1$ which is placed directly after the second parabolic mirror. This polarizer is set on a rotating optical mount. For the detection, two polarizers $W.G_2$-$W.G_3$ are mounted together before the detector. The orientation of the one right-before the detector ($W.G_3$) is fixed parallel to the polarization detected by the antenna. The polarizer P_2 is rotated at an angle 45° with respect to the orientation of $W.G_3$. To further understand the mechanism of detection of two different polarization of electric field, Jones matrix train is applied to the polarizers system $W.G_2$-$W.G_3$.

$$E_D = \begin{pmatrix} 1 & 0 \\ 0 & 0 \end{pmatrix}_{\mathbf{W.G2}} \begin{pmatrix} 1/2 & \frac{1}{2} \\ \frac{1}{2} & \frac{1}{2} \end{pmatrix}_{\mathbf{W.G1}} \begin{pmatrix} E_{\mathrm{TE}} \\ E_{\mathrm{TM}} \end{pmatrix} = \begin{pmatrix} \frac{E_{\mathrm{TE}} + E_{\mathrm{TM}}}{2} \\ 0 \end{pmatrix} \qquad (4.7)$$

Therefore, when only TM mode is excited, half of the magnitude of the actual electric field is detected and the same fact occurs for TE mode.

4.5 PARALLEL PLATE WAVEGUIDE AND SIGNAL RECORDING PROCESS

The PPWG is made of two blocks of aluminum with same dimensions. The width, length and thickness of the waveguide are 30 mm, 10 mm and 15 mm respectively. The inside face of waveguide is hand polished with 320 grit sandpapers. Then, the aluminum surfaces are coated with tens nanometer of titanium and subsequently coated with gold of about 200 nm thickness. The coating plays two roles: to avoid roughness and to increase the conductivity of plates.

In this work, substrates are used to simultaneously fill the space between the plates of PPWG and to support the thin conductive films. Then, the thickness of the substrates determines the plate separation. Actually, two substrates of 0.5 mm thickness, 30 mm width and 10 mm length are employed. The ultrathin conductive films are always deposited onto half width (15 mm) of one of the substrate surface. This substrate with half side coated by the samples is first set on the top of the bottom waveguide. Another bare substrate is next placed on top of the half coated substrate. Finally, we put the top plates of the waveguide. A small sample holder is fabricated to align substrates to the waveguide plates (Fig. 4.7). The whole waveguide system is mounted on mechanical stage and placed at the center of the second parabolic and third parabolic mirror. The mechanical stage can be automatically handled outside the THz-PPWG-TDS system.

Since half of the waveguide contains conductive film located between the plate and half-filled solely with substrate, we can set the reference signal and the sample signal. The reference signals are the THz pulses transmitted through PPWG with substrate. The sample signals are the THz pulses transmitted through PPWG with thin films on substrate. The setting we have just described above greatly facilitates the recording of the reference and the sample signals. We first record a number of THz pulses from the reference side. After that, the waveguide is moved perpendicularly with respect to the beam propagation direction. Then, a number of THz pulses are recorded from the sample side.

The alignment of the PPWG is different for TM and TE modes. We have seen in chapter 3 that the maximum of coupling coefficients are different for the fundamental TM and TE modes. The goal of the alignment is to maximize the coupling of free space THz beam to the fundamental mode. It is preferable to avoid higher propagation modes to simplify the analysis. However, the beam spot in the input face of waveguide is quite large and especially frequency dependent. In particular, the presence of thin film inside PPWG can induce higher modes propagation in TM and TE modes. Therefore, for each measurement, we polarize first the beam to excite the desired mode (TM or TE mode) and align the waveguide accordingly. The alignment is performed by improving the maximum intensity of electric field detected by the detector. THz-PPWG-TDS.

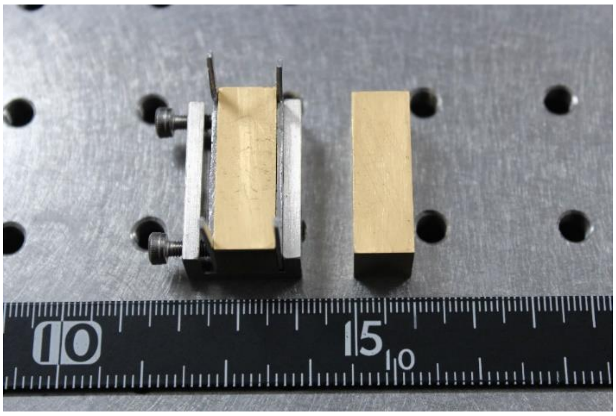

Fig. 4.7 the Parallel plate waveguide employed in this work. The internal faces are coated by gold. In the left side is shown the bottom plate with a homemade samples holder.

Fig. 4.8 shows the main part of the experimental THz-PPWG-TDS. The emitters and the detectors as well as the optical parts for the laser beam path are not represented here. The operation of THz-PPWG-TDS is the same as that of standard transmission THz-TDS. We conclude this chapter by summarizing the overall setup of THz-PPWG-TDS system.

The femtosecond laser is split to a ratio of 80:20 for the emitter and the detector. The 80% beam for emitter is chopped and focused at the InAs semiconductor surface. The weaker laser beam is steered to a mechanical delay stage line and subsequently focused on the dipole antenna via optical lenses. The optical path lengths of the split laser is adjusted to have the same value at the detector position. The delay stage is controlled automatically by a computer and enables to sample the THz pulse for the signal recording. The emitted THz is collimated, polarized and focused onto the input face of the PPWG. After traveling through the waveguide, this output THz beam is collimated, polarized and focused to the detector. The detected current is amplified and sent to a lock-in amplifier which is phase locked to the chopper frequency for the synchronous detection. The electronic detection system and the delay stage controller is synchronized by a LabVIEW computer program. The mechanical stage for waveguide is manually controlled. The THz-PPWG-TDS system is encased inside an acrylic box and purged with nitrogen to minimize the noise due to the water vapor absorption.

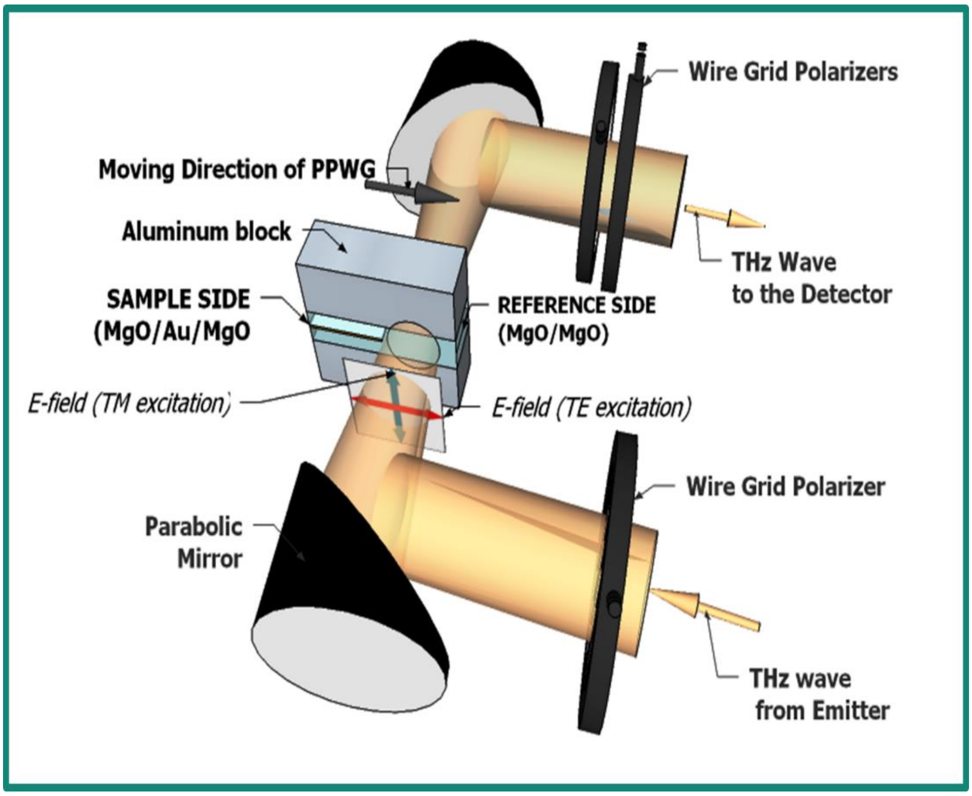

Fig. 4.8 Schematic of the main part of THz-PPWG-TDS. The description is in the main text.

4.6 CONCLUSION

In this chapter, I have presented the experimental setup employed during this work. First, I fabricated a home-made standard transmission-type THz TDS system [13]. The system was manually mounted from the start to the end at our laboratory. Detailed description of the main component in the experimental setup have been outlined. These includes a *p*-type InAs THz emitter and an LT – GaAs dipole antenna receiver. The LT – GaAs was manufactured in our laboratory while the emitter was commercially available. The choice of InAs emitter was imposed by the constraint of THz input beam polarization before the waveguide. In fact, we have control the polarization of the input beam to excite TM or TE modes of the waveguide, respectively. I also designed a combination of wire grid polarizer to detect horizontal and vertical polarization of the electric field. The free space beam shaping consists of four parabolic mirrors as shown Fig. 4.6. Then, I designed a PPWG which is mounted on a moving stage. This configuration simplifies the measurements for reference (THz transmitted through waveguide without thin conductive film) and the sample (THz transmitted through waveguide with thin conductive film) signals.

REFERENCES:

[1]. M. Van Exter, C. Fattinger, and D. Grischkowsky, “Terahertz time-domain spectroscopy of water vapor,” *Opt. Lett.*, vol. 14, no. 20, p. 1128, 1989.

[2]. M. Tonouchi, “Cutting-edge terahertz technology,” *Nat. Photonics*, vol. 1, pp. 97–105, 2007.

[3]. K. P. Cheung and D. H. Auston, “A novel technique for measuring far-infrared absorption and dispersion,” *Infrared Phys.*, vol. 26, no. 1, pp. 23–27, 1986.

[4]. K. Sakai, “Terahertz Optoelectronics,” Springer, 2010.

[5]. T. Dekorsy, H. Auer, H. Bakker, H. Roskos, and H. Kurz, “THz electromagnetic emission by coherent infrared-active phonons,” *Phys. Rev. B*, vol. 53, no. 7, pp. 4005–4014, 1996.

[6]. M. Johnston, D. Whittaker, A. Corchia, A. Davies, and E. Linfield, “Simulation of terahertz generation at semiconductor surfaces,” *Phys. Rev. B*, vol. 65, no. 16, pp. 1–8, 2002.

[7]. P. Gu, M. Tani, S. Kono, K. Sakai, and X. C. Zhang, “Study of terahertz radiation from InAs and InSb,” *J. Appl. Phys.*, vol. 91, no. 9, pp. 5533–5537, 2002.

[8]. S. Kono, P. Gu, M. Tani, and K. Sakai, “Temperature dependence of terahertz radiation from n-type InSb and n-type InAs surfaces,” *Appl. Phys. B Lasers Opt.*, vol. 71, no. 6, pp. 901–904, 2000.

[9]. P. Grenier and J. F. Whitaker, “Subband gap carrier dynamics in low-temperature-grown GaAs,” Appl. Phys. Lett., vol. 70, no. 15, p. 1998, 1997.

[10]. E. Bründermann, H-W Hübers, and M. F. Kimmitt, “Terahertz Techniques,” Springer, 2011.

[11]. Z. Jiang and X. C. Zhang, “2D measurement and spatio-temporal coupling of few-cycle THz pulses.” *Opt. Express,* vol. 5, no. 11, pp. 243–248, 1999.

[12]. K. J. Button, “Quasioptical Techniques at Millimeter and Submillimeter Wavelengths,” *Infrared Millim. Waves V6 Syst. Components,* vol. 6, pp. 277–344, 1983.

[13]. M Razanoelina, R. Kinjo, K. Takayama, I. Kawayama, H. Murakami, D. Mittleman, M. Tonouchi, “Parallel-Plate Waveguide Terahertz Time Domain Spectroscopy for Ultrathin Conductive Films”, *J. Infrared Milli and Terahz Waves* , vol. 36, no. 12, pp 1182-1194, 2015

Chapter 5. APPLICATIONS OF PARALLEL PLATE WAVEGUIDE

5.1 GENERAL INTRODUCTION

This chapter illustrates the applicability of the present method and also shows its limitations. Firstly, we analyze a series of gold ultrathin films having different thickness and compare their TM and TE mode responses. The second target is to demonstrate the effectiveness of this system by investigating on the electronic properties of graphene which is an atomic-thick layer of materials. We present the Fig.-of-merit of the PPWG approach and also compare the results to those obtained with the conventional THz-TDS. The results obtained for graphene clearly show that the waveguide system is a powerful tool to study the electromagnetic properties of two-dimensional conductive materials. The last application is different from the above work since here, we investigate on the magnetic response of metamaterials. In this study, we compare the performance of both normal incidence THz-TDS and THz-PPWG-TDS. In addition, simulation is performed to complete the analysis of the interaction between THz wave and metamaterials and to emphasize the advantages of the PPWG method.

Experimental methods of the samples growth are first described. Then the experimental results are shown. Next, the theoretical framework of the conductivity model are treated and is followed by the experimental data analysis. The last sub-sections are for discussions and interpretations of the data.

5.2 GOLD NANOSTRUCTURES

5.2.1 *Introduction*

Electromagnetic properties of ultrathin metallic films have long been investigated in spectroscopy due to their intriguing behavior in contrast to their bulk counterpart [1]. In a classical point of view, optical property of metallic layer is determined by its skin depth δ which is the characteristic decay length of the applied electromagnetic field [2]. The value of skin depth is usually calculated with the bulk DC conductivity [3]. For example, given the value of DC conductivity of gold in [3], the calculated skin depth at 1THz and at room temperature is about 75 nm. However, this value has been contrasted by Laman et *al* [4] since the DC conductivity of gold layer (thickness of 85 nm and 150 nm) reported in their THz spectroscopic work is less than the handbook value and moreover thickness – dependent. This discrepancy is more relevant with ultrathin gold layer when the thickness of the films become far less than the skin depth and also the operating THz wavelength ($t \ll \lambda_{THz}, \delta$) [5].

The most convenient method to fabricate thin metallic film is thermal evaporation or sputtering deposition to an insulating substrate. At the beginning of deposition process, gold clusters of random shape and nanometer size are formed. As the quantity of deposited gold increases, the irregular metallic islands start to coalesce resulting to a formation of semi continuous film on the substrate. The isolated islands transit to continuous network creating a continuous path for the electrons. At the end of the process, the metallic layer covers the substrate and become a quasi-uniform film with few irregularity [6]. Therefore, it is obvious that the properties of the thin film depends on the density of islands or the average thickness of metallic films deposited on the substrate. At certain critical value of thickness, the film becomes conductive. On the other hand, when the thickness is less than this critical value, the film is insulating. The insulator-metal transition (IMT) phenomenon occurs at this critical value which can be explained by percolation theory [7].

The anomalous electromagnetic properties of metallic films at the IMT thickness have been reported in the past [8] in infrared and far infrared region. Percolation theory have been used to explain the optical behavior of these near-percolating films. In fact, the threshold is characterized by a parameter p_c which can be the critical value of the metallic filling or the surface coverage p of metal clusters. When $p < p_c$, the composite material (substrate and metallic films) remains dielectric and when $p > p_c$, the composite becomes metallic. The DC conductivity σ_{DC} of the structure is expressed in power-law function as $\sigma_{DC} \propto |(p - p_c)/p_c|^r$ while σ_{DC} is zero below p_c [9]. For 2D system, the value of r is nearly equal to 1.3 [9]. The DC dielectric constant ϵ_{DC} can be also expressed in a similar fashion and which diverges at $p = p_c$: $\epsilon_{DC} \propto |(p - p_c)/p_c|^{-s}$ where $s \approx 1.3$ for 2D films.

In far infrared regime, the IMT thickness for gold is about tens of nanometers [8] which is comparable with the characteristic transport length $L(\omega) = (D/\omega)^{0.5}$ in diffuse regime [7]. Also, it has been shown that one can probe the effects of the grain size of gold nanostructures to the carrier dynamics in the THz regime [10]. By using conventional THz-TDS to measure the optical gold conductivity, Walther et *al*. reported that the value of IMT thickness is at $p_c \approx 6.4$ nm [10]. Thus gold nanostructures are appropriate materials to demonstrate the applicability of our THz-PPWG-TDS system in which the interaction of electromagnetic field differs from that of conventional THz-TDS.

Using a series of thin gold films exhibiting a thickness-dependent metal-insulator transition, we investigate the sensitivity of our approach, and apply the formalism for extracting quantitative dielectric parameters of the thin film from our measurements. These dielectric parameters are expected to reveal the nanoscopic properties of the film relating the carrier transport dynamics and the thickness of the ultrathin gold film. Our sample is located at a maximum of the electric field, which optimizes the interaction between the electromagnetic wave and the samples either in the excited odd TE modes (TE_1, TE_3, TE_5,…) or even TM mode (TEM, TM_2, TM_4). The responses of the thin films will be analyzed with respect to the configuration of electric and magnetic field of the THz wave propagating down the PPWG.

This section is outlined as follow: the first sub section describes the gold thin samples preparation by sputtering method. The gold thin films with four different thicknesses are analyzed here: 1 nm, 4 nm, 8 nm, and 180 nm-thick. The next subsection shows the images of the surface morphology of the thin films with atomic force microscopy (AFM). Then, the experimental data obtained by THz-PPWG-TDS will be presented. We firstly analyze the results in the classical Drude theoretical framework and fit the data accordingly. We extend this analysis to generalized Drude – Smith model for the gold thickness at 4 nm. In the last sub-section, we compare our approach to the conventional transmission type THz-TDS.

5.2.2 *Samples preparation*

Gold nanostructure is deposited onto magnesium oxide substrates (MgO (100)). The substrates were supplied by CrysTec Company and polished on both side. The surface dimension of the MgO substrates are the same as the PPWG: 30 mm (*width*) × 10 mm (*length*) × 0.5 mm (*thickness*). The surface of the MgO were observed using AFM and the obtained surface properties are summarized in Table 5.1. We also measure the refractive index and the extinction coefficient of MgO by conventional transmission THz TDS. In the range of 0.1 to 2.2 THz, the refractive index is nearly frequency-independent and has a value of 3.15 ± 0.05 (cf. Fig. 2.1 of chapter 2). Furthermore, THz absorption of MgO is negligible in this spectral range.

Table 5.1 Specific values of surface roughness of MgO measured by atomic force microscopy. The measurement area is (1 μm × 1 μm) with a later control resolution of 0.1 nm. Ra is the average roughness, RMS is the root mean square roughness and P – V is the maximum peak –to – valley range.

Standard specification	Ra	RMS	P-V
Value	<0.5 nm	<0.8 nm	<3.5 nm

The sputtering was performed with our laboratory sputtering machine. One sample was fabricated for each sputtering operation. Before the sputtering operation, half of the MgO (15 mm in width) was covered by a metallic sheet mask to avoid deposition of gold thin films in this side. Then the substrate was placed on a rotating sample holder in order to deposit homogeneous films over the surface. The deposition condition was performed under ultrahigh vacuum. We controlled the thickness of the gold layer by following the trend of Fig. 5.1 . Three samples of thickness of 1 nm, 4 nm and 8 nm were sputtered with deposition rate of 4 nm/min (black solid line with square black dots). The sputtering power was about 20 W. One gold sample with thickness of 180 nm was prepared with deposition rate of 18 nm/min. It was more convenient to control the thickness of the film at lower deposition rate, however deposition of gold with the power less than 20 W was not stable in our case.

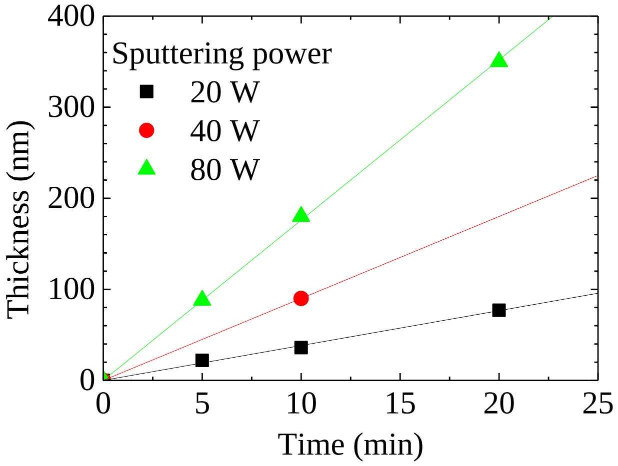

Fig. 5.1 Gold thickness growth in function of sputtering time. The legends inside the figure indicate the sputtering power. The solid lines which connect the triangles, circles and squares are the linear fitting of the deposition rate. The green, red and black solid lines indicate approximated deposition rates of 18 nm/min, 9 nm/min and 4 nm/min, respectively.

5.2.3 *Atomic force microscopy characterization*

After each deposition process, the AFM images of the gold structure were taken with MFP 3D Asylum Research AFM instrument. The condition of the operation was under ambient air in tapping mode. The cantilevers used in the imaging process have a spring constant of ~ 42N/m and a resonant frequency of ~ 300 kHz. The technique of AC mode imaging is nondestructive and allows to image an area up to 90 μm × 90 μm. For comparison, Fig. 5.2 shows the surface morphology of gold nanostructures for 4 nm, 8 nm and 180 nm – thick, respectively. The images size are 500 nm × 500 nm. From the image of gold film with the thickness of 180 nm in Fig.

5.2(c), the formation of big sized particles grain can be seen. At the thickness of 8 nm in Fig. 5.2(b), the size of the gold particles decreases but still connected together with the presence of some voids. Then, we would expect a conductive film in this case. For gold thin film with thickness of 4 nm, the presence of grain particle is not so evident in the AFM image but some clear network path can be seen.

Fig. 5.3 indicates the cross section and the image of gold sample with thickness of 4 nm. The profile curve is extracted from surface covered by gold to surface without gold (black line drawn in the Fig. inset). Here, the length of the line which measures the thickness difference is about 60 μm. The "bump" observed on the curve is due to the cover edge used during the fabrication process, which indicates the surface transition from the non – coated to gold coated surface.

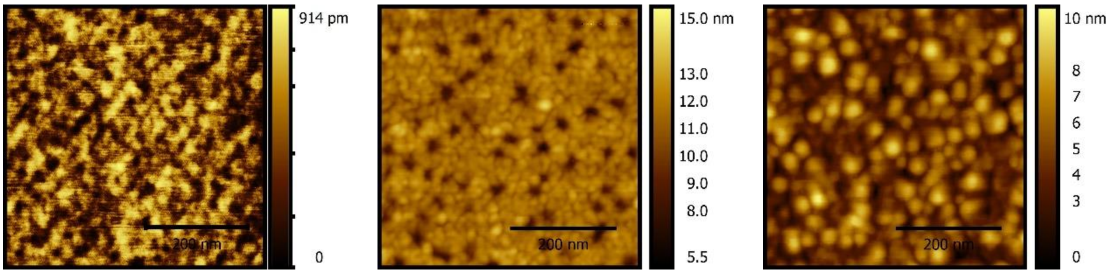

(a) – [Au ~ 4 nm] **(b)** – [Au ~ 8 nm] **(c)** – [Au ~ 180 nm]

Fig. 5.2 AFM characterization of gold nanostructure surface morphology. The scan was done for an area 500 nm x 500 nm.

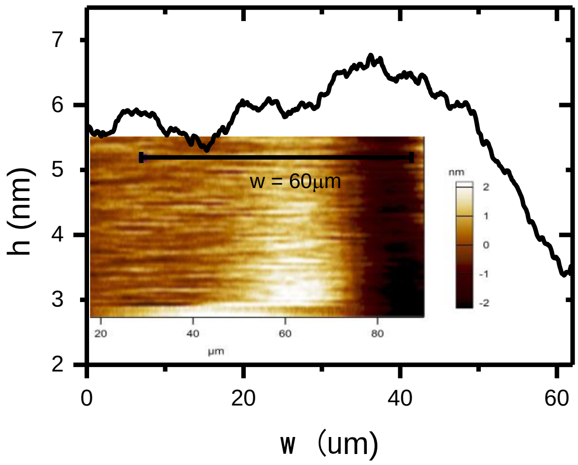

Fig. 5.3 Thickness measurement of 4 nm – thick gold using AFM. h is the thickness and w is the scan width.

5.2.4 *Experimental results in THz-PPWG-TDS*

Firstly, we summarize the experimental procedures for measurement of ultrathin gold films response with the first experimental system we have discussed in chapter 4. Two MgO substrates are inserted in the waveguide which is composed of two flat aluminum plates with 1 mm plate separation, 10 mm length and 30 mm width. Halves of the bottom substrates are coated by gold films and the top substrate is a bare clean MgO. The PPWG is mounted on a stage manually controlled to scan the entire width of the waveguide. The reference pulses (through a waveguide containing only two MgO plates) and sample signals (through a waveguide containing a thin gold film between two MgO plates) pulses are recorded at five different locations each with 1024 data points. The measurement time is 40.92 ps which gives a frequency resolution of 0.0244 THz.

Fig. 5.4 show the averaged THz pulses reference and THz pulses sample for gold 180 nm in TM (left) and TE mode. After Fourier transforming the time domain data, we obtain the frequency domain response of the samples. The time domain pulses as well as the spectra are averaged over five data recorded for each sides (5 for reference and 5 for samples). The error bars indicate the standard deviation. The experimental misalignment effect between successive locations where the signals were recorded are taken into account in the errors bars. In this work, the misalignment of the waveguide is the main factor of the error which limits the signal to noise ratio of the system. In other words, if the THz response of the ultrathin film gold are situated within the error bars in the spectrum, the dielectric parameters cannot be retrieved. As mentioned in previous chapter, this fact is the main limitation of the developed system.

Fig. 5.5 indicate the experimental Fourier transform of the reference (for both TE and TM mode excitation) along with the THz spectra of the sample waveforms at thicknesses 1 nm, 4 nm, and 8 nm. In both cases, the spectrum of reference and sample almost overlap at 1 nm film thickness. This indicates that at 1 nm thickness, the gold thin film behaves like an insulator, and is indistinguishable from MgO response in both configurations. However, as the thickness of the gold film increases, the sample spectra get smaller, indicating the evolution of the dielectric properties of the gold film with increasing thickness.

Since we already had all the experimental data required for the parameters extraction, the next step is to model the conductivity of the ultrathin gold film under analysis.

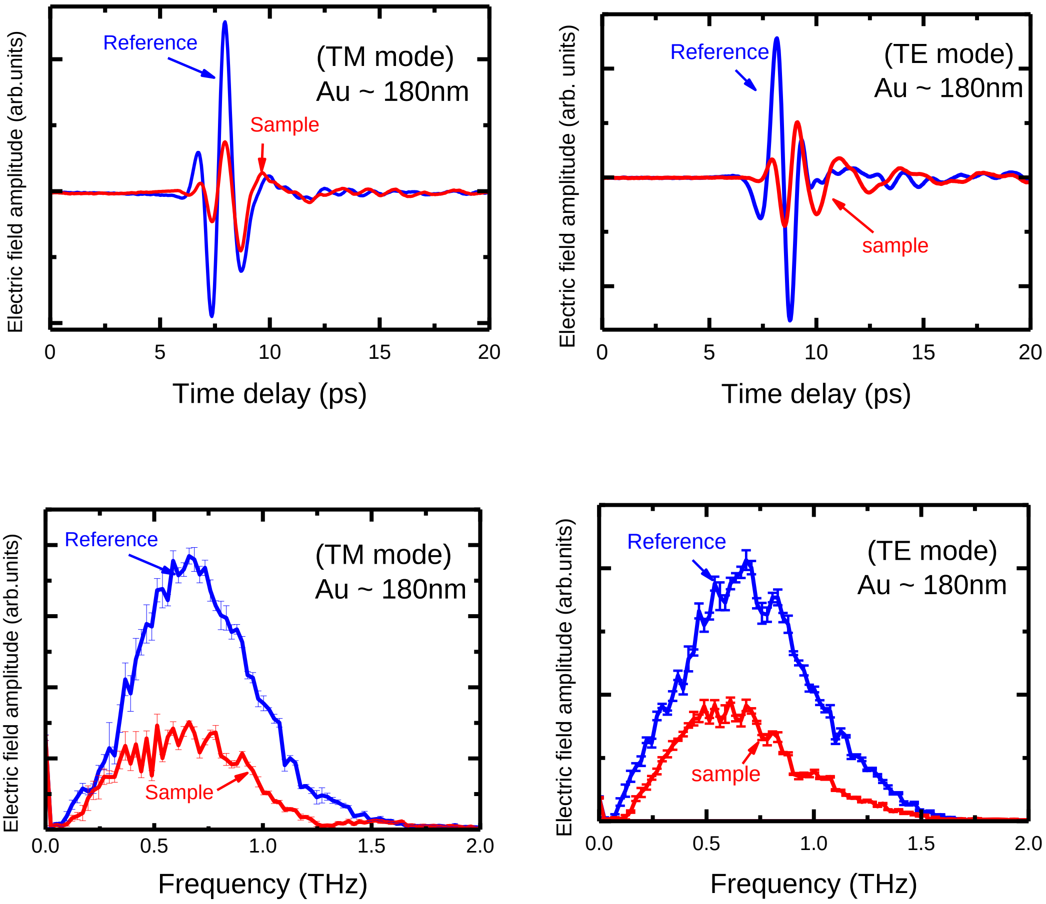

Fig. 5.4 Average of transmitted THz pulses of references and samples for gold sample at thickness of 180 nm. The measurement are performed in TM and TE modes. The spectra are associated with the error bars which are the standard deviation between five recorded for the reference and for the sample, respectively. The axis of the time delay is shorten to 20 ps to emphasize the difference between the reference and the sample signals.

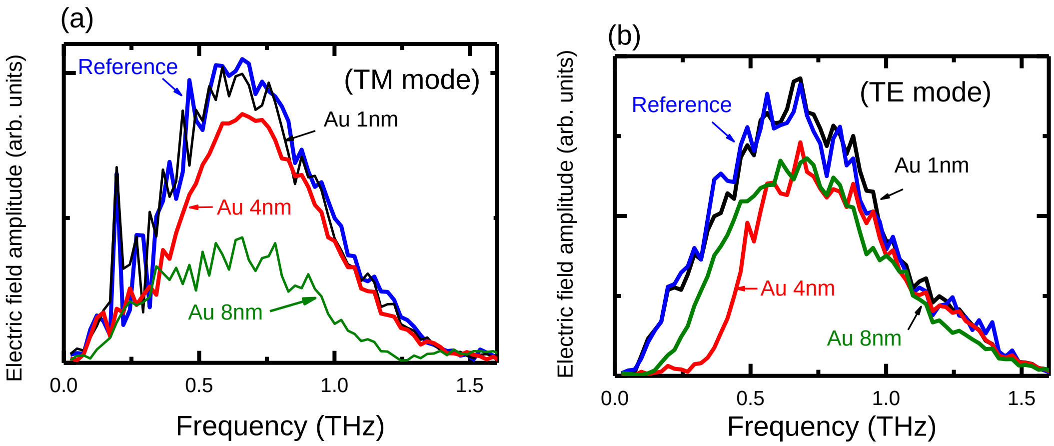

Fig. 5.5 THz spectra of the reference and the gold samples of thickness of 1 nm, 4 nm and 8-nm in (a) TM and (b) TE modes.

5.2.5 *Drude model and parameters extraction*

The Drude model is a classical description of carrier response in a solid within the framework of charge transport dynamic in diffuse regime. This model have long been applied for several type of solid state systems and have produced a good agreement with the experimental data. In THz frequency region, most of metal or meta-like systems can be described as good conductor which satisfy the Drude model approximation [11]. As we investigate on the properties of nanostructure metallic films, we start to fit the experimental data within this classical theory.

In its simplest form, Drude models treat electrons in metal similar to the molecules of a gas which move and collide with one another [12]. Charge carriers are assumed to undergo an isotropic scattering resulting to a complete randomization of momentum. The main assumption of the model is that the relaxation of the system to its equilibrium state is described by an average relaxation time τ. Therefore, the average equation of the electron motion for the momentum is governed by:

$$\frac{\partial \boldsymbol{p}}{\partial t} = -\frac{\boldsymbol{p}}{\tau}, \tag{5.1}$$

where $\boldsymbol{p}$ is the average momentum.

By applying an external time dependent electric field $\boldsymbol{E}_{\text{ext}}(t) = \text{Re}\left(\boldsymbol{E_0} e^{-i\omega t}\right)$, the equation of motion Eq. (5.1) becomes:

$$\frac{\partial \boldsymbol{p}}{\partial t} = -\frac{\boldsymbol{p}}{\tau} - e\boldsymbol{E}_{\text{ext}}, \tag{5.2}$$

where e is the absolute value of the electronic charge. We are looking for a time varying average momentum of the form: $\boldsymbol{p}(\omega)\exp(-i\omega t)$. Thus

$$\boldsymbol{p}(\omega) = -\frac{e\boldsymbol{E}_0(\omega)}{\frac{1}{\tau} - i\omega}. \tag{5.3}$$

If we have a density of charge carrier *N* with an effective mass $m*$, the current density is:

$$\boldsymbol{J} = -\frac{Ne}{m^*}\boldsymbol{p}. \tag{5.4}$$

Inserting Eq.(5.3) into (5.4) and by virtue of Ohm's law, the Drude conductivity is:

$$\sigma(\omega) = \frac{\boldsymbol{J}(\omega)}{\boldsymbol{E}_0(\omega)} = \frac{(Ne^2\tau/m^*)}{1 - i\omega\tau}. \tag{5.5}$$

The quantity $(Ne^2\tau/m^*)$ is the DC Drude conductivity or the conductivity of the metal at zero frequency. From the definition of plasma frequency $\omega_p{}^2 = Ne^2/(\epsilon_0 m^*)$, the conductivity can be rewritten as:

$$\sigma(\omega) = \frac{\omega_{\mathrm{p}}^2 \epsilon_0 \tau}{1 - i\omega\tau}. \tag{5.6}$$

Therefore, in the parameters extraction Eqs. (3.60) – (3.61), the sheet conductivity is to be substituted by $\sigma_{\mathrm{S}} = t\sigma(\omega)$. t is here the thickness of the film (not to confuse with time) and (ω) is obtained from Eq.(5.6). Since the gold thicknesses are known, the free – parameters to retrieve are the plasma frequency ω_{p} and the scattering time τ.

In the data fitting, we have replaced the plasma frequency to the reduced plasma frequency $\omega_{\mathrm{p}}/2\pi$ since the experimental data are directly in function of frequency. The unit of the scattering time is set to femtosecond (fs) and the $\omega_{\mathrm{p}}/2\pi$ in THz. We restrict the parameters to be positive. For the reduced plasma frequency, we upper limit the value to $\omega_{\mathrm{p}}/2\pi = 2500$ THz which is a higher than the reported value for bulk gold (2080 THz [13]).

A rough measurement of the THz input beam waist is performed first at the maximum electric field during the experiment and the beam is estimated to be around 3 mm. Despite the confocal arrangement of the four parabolic mirrors, the high divergence of the generated THz beam supposes that the waist is frequency dependent. That affects the estimation of power coupling as we have seen in the parameter extraction section of chapter 3. Therefore, the THz beam waist in the coupling coefficient equation of Eq. (3.63) is also taken as free parameters and computed following the paraxial beam approximation in Gaussian optics (Eq. (3. 62).

For the following results, the frequency bandwidth over which the optimization is done is 0.4–1.2 THz. The lower frequency is limited by the PPWG cutoff frequency of the reference, and the higher frequency is limited by the PPWG transmission of the reference signal. Since the plate separation of the PPWG is 1 mm and the refractive index of the substrate is 3.15, more than 20 modes can propagate in the waveguide for a cutoff frequency at 1.2 THz. However, only odd TE mode (TE1, TE3) and even TM modes (TEM, TM2) can be excited due to the symmetry of the overlap integral in the coupling coefficients (Eq. (3.51) – (3.52), Eq. (3.63)). Also, the finite conductivity of the aluminum plates in THz range (σ_{Al} =3.5×10^5 S/cm) decreases the transmission of higher order modes. Then, for the reference, we include two waveguide modes (m = 2) in the calculation in Eq. (3.57), while for the sample, we include three modes (n = 3) to account for the measured signals.

5.2.6 *Fitting results with Drude model and discussion.*

5.2.6.1 Fitting with Drude Model

Fig. 5.6(a) shows the experimental transmission of the waveguide with 180 nm thick gold film, along with the theoretical fitting, in TE mode. The error bars are also calculated in the transmission curves. The best value of fitting for the beam waist is at parabolic mirror focal length (or alternatively F-number) around 65 mm in TE mode. Variation of the plasma frequency $\omega_p/2\pi$ between 2000 to 2500 THz yields a similar fit. The scattering time can also change from 10 to 30 fs without changing the fit appreciably. These Drude parameter means that the gold behaves like a bulk solid.

Transmission data and the corresponding theoretical fit for gold 180 nm in TM mode are shown in Fig. 5.6(b). Like in TE mode, the value of the focal length which fits the experimental data is 65 mm. This fit is obtained with a value of $\omega_p/2\pi$ between 2000 to 2500 THz and τ in the range (10 fs, 50 fs). It should be noted that the same fitting process is applied for TE and TM mode with their respective characteristic equations.

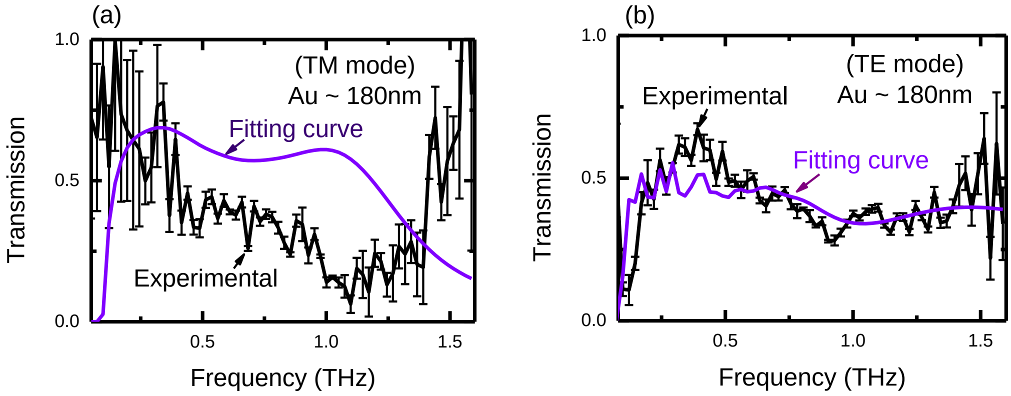

Fig. 5.6 Experimental transmission data and the Drude model fitting curves associated for gold sample 180 nm thickness in (a) TM and (b) TE modes

Fig. 5.7 shows the theoretical fitting for gold at thicknesses of 8 and 4 nm for TE and TM modes. For gold at 8 nm thickness, the values of plasma frequency for the best fitting are around the bulk value either in TE or TM mode. Here, we have already fixed the value of the waist to that of fitted from the case of gold 180 nm. The conductivity can be described by Drude model TE mode fitting. For a 4-nm film thickness, the best fitting values are also completely different for TE and TM mode. The scattering time are quasi-similar for the Drude fitting in TE mode for gold 8 nm and 4 nm as shown Fig. 5.7(b) and (d).

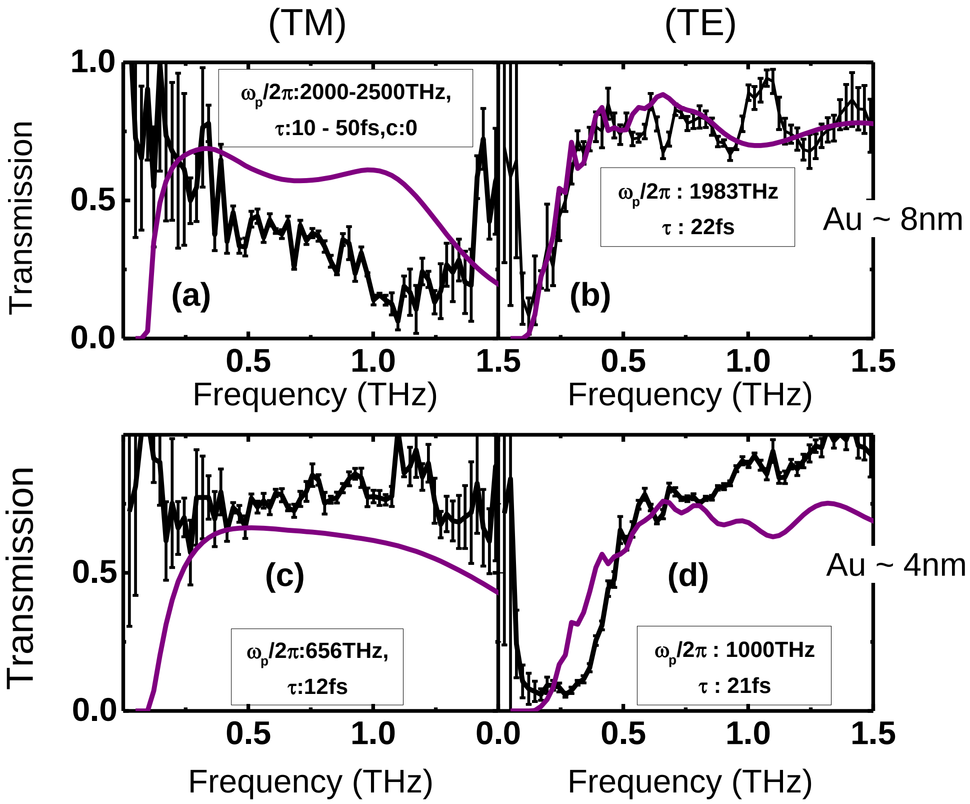

Fig. 5.7 Experimental transmission data with Drude model fitting curves for gold samples of 8 nm and 4 nm thickness. The extracted parameters are indicated inside the figures where ω_p and τ are the plasma frequency and the scattering time, respectively. TM mode transmission and Drude model fitting curves for gold samples of (a) 8 nm and (c) 4 nm thickness. TE mode transmission and Drude model fitting curves for gold samples of (b) 8 nm and (d) 4 nm thickness.

5.2.6.2 Discussion

To provide a clear physical interpretation of the results, it is worthwhile to examine the dispersion equations given by Eqs. (3.44) and (3.45). When the interface conductivity $\sigma_S \rightarrow \infty$, it is easy to see that the dispersion equations reduce to the results for two independent layered PPWGs. The perfectly conductive film partitions the waveguide into two isolated waveguides with half the plate spacing. The phase-matching condition (unique z-propagation constant) at the interface is no longer valid so that the tangential electric fields across the conductive interface are not continuous. This leads to decoupled equations for two PPWGs. Then, the total electric field detected consists of all possible combinations of excited modes in the lower and upper PPWG, superposed.

In the present work, we can assume that the thickest gold film (t = 180 nm) has the value of crystalline bulk conductivity [13]. Accordingly, the thickness of the film is nearly three times the skin depth at 1 THz. In this case, the gold thin film could be approximated as a perfect electric conductor and the above mentioned arguments would apply to the data of Fig. 5.6. In TE mode, the electric fields of the waveguide containing gold thin film (180 nm) are linear combination of modes which are symmetrical with respect to the plane $d/2$ with cutoff frequency $f_c = \frac{mc}{2n_{\mathrm{MgO}}(^{d}/_{2})}$ (m = 1, 2, 3, …)The dominant mode in each region of the waveguide is also TE_1 with theoretical cutoff frequency $f_{\mathrm{c}} = 0.095$ THz. In the fitting process, different gold conductivities near the bulk value give the same f_{c} for the dominant and high-order TE modes. It means that the propagation loss is not influenced by the dielectric properties of the gold (which can be considered as perfectly conductive) but only by the THz wave coupling into and out of the waveguide. Therefore, the only free parameter which determines the fit is the frequency-dependent THz beam waist. The value of parabolic mirror focal length extracted for the waist calculation (65 mm) is reasonable since the actual focal length of the mirrors in the first experimental setup is 76.2 mm. In particular, the optimized distance between the focusing mirror and the waveguide input cross section is 65 mm and it does not coincide with the actual focal length. Also, three modes of the PPWG with the gold thin film are enough to have a good fit (Fig. 5.6) since the higher modes coupling coefficients are very small compared to that of the fundamental TE_1 mode.

For the case of TM mode, the presence of a thin metal film extremely perturbs the field distribution relative to the PPWG reference. From Fig. 5.7(b), the fitting curve and the experimental result do not exactly agree. The first reason is that the power coupling of THz input beam to the guided wave of the PPWG with the metallic film is less efficient in TM mode than in TE mode. In addition to the fundamental TEM mode, the presence of important ripples in the transmission curve suggests that many higher TM modes could be excited. In fact, many higher propagating modes induce interferences in the frequency domain data and cause a substantial dispersion loss. Therefore, the fitting process cannot satisfy the condition required since we only take account of three first higher modes for the sample. We could insert in the analysis model more combination of possible mode excited to fit the experimental data, but the increasing number of fit parameters renders the analysis less valuable.

When the thickness of the gold film is extremely small ($t \ll \delta, \lambda$), the waveguide mode of the upper and lower halves of the waveguide can couple with each other in a symmetric and antisymmetric way. These facts result in hybridization of modes, as described by the dispersion equations. Only modes which satisfy the phase-matching condition propagate down the waveguide. In addition, as in the PPWG reference, the antisymmetric mode cannot couple with the Gaussian input beam due to the symmetricity of the overlap integral in the coupling coefficient calculation.

Despite the fact that gold film which has a thickness of 8 nm satisfies the above condition ($t \ll \delta, \lambda$), TE mode again yields a better fit to the analysis than TM mode. In fact, the dispersion equation for TM case is based on the presence of longitudinal E_z field component. In the case of thin metallic sample with finite conductivity, the fundamental mode excited is still the TEM mode that has essentially a vanishing E_z component. The longitudinal current flowing in the film is very small which yields a very low dissipation loss. As a result, the transmission loss is mainly due to the free space coupling to the waveguide at the input and output facets, rather than the propagation loss due to the thin film. This idea is validated by the similarity of the experimental transmission loss for the thin (8 nm) and thick (180 nm) films.

According to Fig. 5.7, experimental transmission and the TE mode fitting are in good agreement with the conductivity parameters from reference [10]. Here, the dominant transverse electric fields give two main advantages. First, the distribution of fields remains continuous at the film interface. Even though the conductivity of the gold is still high, a strong coupling through the film keeps the waveguide modes coupled. Second, the concentration of fields in the thin gold layer results in a larger current through the film. A higher energy loss translates into stronger attenuation and thus a larger difference between sample and reference data. Unlike in TM mode, the loss in transmission is mainly due to the propagation, not the input and output coupling. Consequently, we can extract spectroscopic information related to the gold film.

In the case of gold thickness at 4 nm, the curve fitting of the transmission in TE and TM modes suggests that the materials response shows different behavior from Drude model. In the introduction of this section, it was indicated that there is a critical thickness (IMT) at which the conductivity and dielectric constant develop singularity. Since at thickness 1 nm, the gold film is an insulator (in our case), we make the assumption that gold of 4 nm-thick is within the range of IMT. As result, the classical Drude model may not be relevant for the analysis and a more general formalism should be considered.

5.2.6.3 Drude – Smith model

The Drude – Smith model has been developed by Smith [14] to describe the optical response of liquid metal and quasicrystal. One year after the publication of Ref. [14], Schmuttenmaer group successfully describe the experimental transient photoconductivity of dye-sensitized titanium dioxide in THz range by utilizing this model [15]. Since then, the name “Drude – Smith” conductivity model has gained popularity to study nanomaterials [16], IMT system [17], and disordered materials exhibiting carriers localization or dominated by carriers back scattering phenomenon in THz regime.

The Drude –Smith model is based on the current response of the electron system to a δ -function impulse of electric field at t = 0. From the definition of current density, one has the relation:

$$\boldsymbol{J}(\omega) = \sigma(\omega)\boldsymbol{E}(\omega). \tag{5.7}$$

If at t = 0, an unit impulse of electric field δ (t) is applied to the system, the frequency dependent conductivity can be seen as the Fourier transform of the current such as:

$$\sigma(\omega) = \int_0^\infty J(t)e^{i\omega t}dt. \tag{5.8}$$

Starting from the assumption that the scattering events are independent of each other (no memory about the previous collision) and obey to Poisson distribution, the current can be written as [14]:

$$J(t) = J(0)e^{-t/\tau}, \tag{5.9}$$

where τ is the is characteristic relaxation time of the system to return to the equilibrium state [14]. $J(0) = Nep(0)/m^* = (Ne/m^*)\int eE(t)dt = Ne^2/m^*$.
Inserting Eq. (5.9) into Eq. (5.8), the Drude model conductivity is retrieved [14]:

$$\sigma = \frac{Ne^2\tau/m^*}{1 - i\omega\tau} \tag{5.10}$$

Now, suppose that the carriers undergo collisions with an average time interval τ between two scattering events, as within Drude framework. Between a time interval (0, t), Poisson distribution gives the probability of n scattering events to occur:

$$P_n(0,t) = \left(\frac{t}{\tau}\right)^n \frac{e^{-t/\tau}}{n!} \tag{5.11}$$

In his paper [14], Smith introduced a “memory function” about the previous scattering that has the function of “persistence of velocity”. After n$^{\text{th}}$ scattering event, the preserved velocity of carriers is reduced by a factor c_n to its initial value. Therefore, the current takes the form:

$$J(t) = J(0)e^{-t/\tau}\left[1 + \sum_{n=1}^{\infty} c_\text{n}\frac{(t/\tau)^n}{n!}\right] \tag{5.12}$$

From Eq. (5.8), the complex frequency – depend conductivity reads:

$$\sigma = \frac{Ne^2\tau}{m^*(1 - i\omega\tau)}\left[1 + \sum_{n=1}^{\infty}\frac{c_n}{(1 - i\omega\tau)^n}\right] \tag{5.13a}$$

The main finding of Smith is that Eq. (5.13a) reproduces very well experimental results of anisotropic as well as isotropic scattering. In fact, if the scattering is independent to each other, the factor $c_n = c_1{}^n$ and Eq. (5.13a) gives the Drude equation. In general, c_n is proportional to the expectation value of cos (ϕ) for elastic scattering. ϕ is the angle between the initial and the n-th velocity. Therefore, if the ϕ angle is less than $\pi/2$, the value of c_n is positive and in the interval [0, 1]. In contrast, if the scattering angle is more than $\pi/2$, c_n is negative ([-1, 0]) and a preferential backscattering is observed.

The predominance of backscattering event have been observed in nanostructure crystal including metallic and silicon nanostructures [10].In practice, only the first term $c_1 = c$ is retained to fit experimental data and its value is set to be in the interval [-1, 0]. This choice is justified by the fact that the material response can be tuned continuously between isotropic scattering (Drude response with $c = 0$) to a carriers localization ($c = -1$). Therefore, we change the Drude model in the experimental data fitting of gold 4 nm to Drude – Smith model with the additional free parameters $c \in [-1, 0]$:

$$\sigma = \frac{Ne^2\tau}{m^*(1 - i\omega\tau)}\left[1 + \frac{c}{1 - i\omega\tau}\right] \tag{5.13b}$$

The curve fitting of the transmission in TE and TM modes are in good agreement with the experimental data with parameters values in the Fig. 5.8. The value of $c \approx -0.9$ indicates that the predominance carrier transport is the backscattering. This result is consistent with that of Ref. [10]. The backscattering event might originate from the reflection of carriers from gold grain boundary, and then a geometrical effect of the thin film surface morphology at IMT. The large value of scattering time τ ≈ 50 fs is also in agreement with reported value [10].

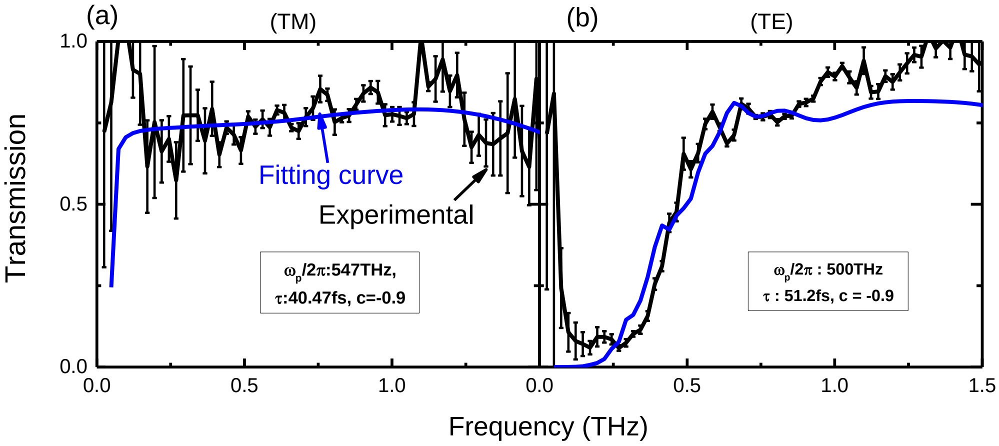

Fig. 5.8 Experimental transmission data and Drude-Smith fitting curves with fitting parameters shown inside the figures in (a) TM mode and (b) TE mode for gold sample of 4 nm thickness.

The sensitivity of TE mode has been explained in the preceding paragraph and confirmed in the present case. But interestingly, the TM mode analysis also produces a good fit. An explanation for this is that the gold thin film at a thickness of 4 nm induces a very small perturbation of the PPWG reference-dominant TEM mode. Consequently, the power coupling coefficient of the PPWG reference and that of PPWG with thin film is nearly similar. Thus, the optical parameters of the gold could be extracted from the experimental transmission data.

5.2.7 *Comparison of conventional THz-TDS and THz- PPWG-TDS*

We have also performed conductivity measurements of our samples with the well-established transmission THz–TDS. In summary, the main difference between the THz- PPWG-TDS and the standard transmission THz–TDS lies in the fact that the former has a parallel incidence and long wave–sample interaction path, whereas the latter has a normal incidence and very short THz interaction path with the sample. An experimental setup as described in [10] is used for the measurements. The parameters extraction of normal THz-TDS has been explained in chapter 2 and is applied here. Table 5.2 shows the extracted parameters for optical conductivity with PPWG method and transmission THz–TDS. The TE mode analysis and the transmission THz–TDS reveal that our gold sample at a thickness of 8 nm has a Drude-like conductivity behavior. In normal THz–TDS, this high conductivity makes the measurement challenging as shown in Fig. 5.9**.**. The low signal to noise ratio for the experimental values induces a large uncertainty in the measurement. However, the agreement between values given by two methods reinforce that TE mode excitation provides the desirable spectroscopic information for conductive thin films.

Finally, a very interesting comparison for both methods is the case of gold thin film at 4 nm. Fig. 5.10 shows the time domain pulse of THz transmitted through MgO coated by 4 nm gold thin film in normal incidence. The suppression of the first reflection pulse indicates that gold thin film behaves as a THz antireflection coating. This has been investigated by Thoman et *al*. [5]. Following the same argument as in Ref. [5] we can draw a simple physical picture to explain the values of conductivity derived for our sample. The antireflection condition is expressed by the following impedance matching $\sigma_s Z_0 = n_{\mathrm{MgO}} - 1$. As above, σ_s is the sheet conductivity of gold thin film, while Z_0 is the free space impedance and n_{MgO} is the refractive index of MgO. Since the substrate has negligible extinction coefficient and $n_{\mathrm{MgO}} = 3.15$, the impedance matching condition is satisfied if $\sigma_S = 0.0057$ S (the imaginary part of the conductivity is zero). If we arrange the expression of conductivity (Eq.(5.13b)) in real and imaginary part and setting $\mathrm{Im}(\sigma_S) = 0$, the value of Drude-Smith conductivity parameters which fulfill the impedance matching condition (with gold thickness 4 nm) are theoretically: $c \approx -0.55$ and with DC conductivity $\sigma_0 = \varepsilon_0 \omega_p{}^2 \tau \approx$

$2.5810^6\ \mathrm{S/m}$. In both transmission and waveguide-based THz TDS, the plasma frequency and scattering time (cf. Table 5.2) satisfy approximately the preceding theoretical relation.

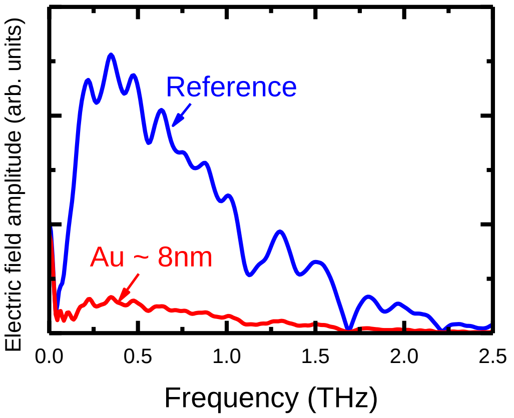

Fig. 5.9 Spectra of gold sample of 8 nm thickness. The measurements were performed with conventional THz-TDS. The reference is the transmitted THz wave through the MgO substrate and the sample signal is the transmitted THz wave through Au/MgO

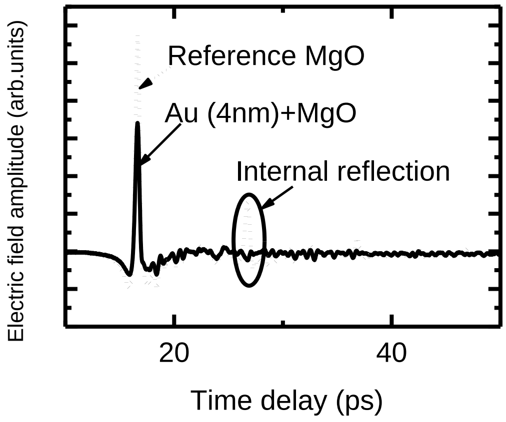

Fig. 5.10 THz time domain response of gold 4 nm in conventional THz-TDS

Table 5.2 Comparison Table of conductivity extracted from Drude-Smith model in TE and TM mode and Standard Transmission THz-TDS

Drude-Smith parameters	TE Mode			TM mode			Transmission THz-TDS	
Gold Thickness	4 nm	8 nm	180 nm	4 nm	8 nm	180 nm	4 nm	8 nm
$\omega_p/2\pi$ (THz)	500	1983	[2000, 2500]	547	-	-	341	1629
τ (fs)	51.2	22	[10, 30]	40.4	-	-	70	10
c	-0.9	0	0	-0.9	-	-	-0.35	0

5.2.8 *Conclusion*

In summary, we have analyzed the capability of PPWG to characterize ultra-thin film of conductive material in THz range. First, it was demonstrated that TE mode excitation offers better sensitivity due to strong transverse electric field which has its maximum in the middle of the waveguide. Second, a good agreement of the optical parameters extracted by TE mode PPWG method and the conventional THz TDS method has been found.

It should be noted that for thin poorly conductive films, TM mode excitation can also be used for a sample located in middle of PPWG. The requirement is that the thin film does not disturb deeply the electric field distribution of the mode so that perturbation method or the dispersion equation could be employed. However, due to the plasmonic nature of TM mode [18], we should be careful on the derivation of the right analysis. In addition, a small misalignment or a small air gap between the dielectric slab and the metallic waveguide plates has a drastic effect in the transmission pulse [19].

5.3 SINGLE ATOMIC LAYER: GRAPHENE

5.3.1 *Introduction*

Currently, there is much interest in atomically thin, layered materials, including graphene [20], hexagonal BN [21], transition metal dichalcogenides (e.g., MoS_2, WSe_2) [22, 23], III-VI layered semiconductors (e.g., InSe, GaSe) [24, 25], and black phosphorous [25]. These novel materials host two-dimensional (2D) carriers with unconventional properties that are promising for a wide range of applications in electronics, photonics, and optoelectronics. However, many of these emerging materials have rather low conductivities, which require high-sensitivity techniques in order to reveal their basic characteristics and provide insight into their novel band structure.

In the terahertz frequency regime, the complex conductivity, σ, of charge carriers can be conveniently determined without any contacts by using THz-TDS [26]. However, when applied to 2D materials, conventional THz-TDS usually requires tremendous efforts to detect finite signals because of the small interaction between the THz radiation and the material. Namely, since these materials are atomically thin, a normal incident beam in a standard transmission THz spectroscopy system experiences a very short-length interaction with the material.

One of the widely used methods to increase the response of 2D materials to THz radiation is by increasing the carrier density through “gating”, i.e., by applying an external electric field in a transistor configuration [27, 28]. However, this is not always possible for general 2D materials and, more importantly, requires gate electrodes. One would also have to consider possible influences of gate-induced carriers in the substrate. A more convenient approach is to integrate graphene in a planar waveguide geometry. Demonstrations have been reported about the efficiency of such a geometry in the infrared/visible range for waveguide modulators [29, 30] and in graphene-based transistors and microcavities [31, 32]. Such an approach is particularly attractive because the long interaction length inside a waveguide provides a high sensitivity. The achievable interaction length is just limited by the waveguide length. Furthermore, waveguide geometries allow one to readily probe the response of a 2D material to different electromagnetic polarizations (electric field parallel or perpendicular to the 2D surface) through waveguide mode control.

Here, we describe a sensitive, non-destructive, and versatile method for characterizing the conductivities of atomically thin materials in the THz range using a parallel-plate waveguide (PPWG). In the present study, we successfully probed and characterized low-density carriers in a single atomic layer of graphene. The graphene layer was sandwiched between two MgO substrates and inserted into the PPWG. In this configuration, the interaction of the transverse electric (TE) mode to the graphene layer was optimal, leading to a substantial (~30%) change in transmission even for a sheet carrier density as low as 2×10^{11} cm^{-2}. On the other hand, conventional normal-incidence transmission THz-TDS failed to detect any signal for this carrier density. Furthermore, the transverse magnetic (TM) mode did not show any sign of interaction with the graphene monolayer because the electric field in this mode is perpendicular to the 2D layer.

This section is outlined as follow: we first present the experimental technique of graphene growth and Raman characterization. Then, the experimental THz results obtained by conventional THz- TDS and THz-PPWG-TDS are compared. Here, we emphasize the main advantage of our technique compared to the existing method for probing carriers in single atomic layer. A theoretical section is dedicated to charge carriers transport in graphene and the conductivity model used for data fitting. Finally the extracted conductivity is discussed with the reported values in literatures.

5.3.2 *Experimental technique*

The samples used in this study were provided by Ajayan's group of Rice University. Two graphene samples (Samples A and B) are grown using chemical vapor deposition (CVD). A copper foil was placed in the deposition chamber and annealed at a temperature of 1000°C in a hydrogen/argon gas at a pressure of 1 Torr for 20 min. Methane was introduced into the chamber with a flow rate of 4 standard cubic centimeters per minute (sccm) for 10 min. The sample was cooled for 20 min in a hydrogen/argon gas. The grown graphene layer was then transferred onto two MgO (100) substrates, which were transparent in the THz frequency range. The dimensions of the MgO substrate were also 30 mm (width) × 10 mm (length) × 0.5 mm (thickness). Half of the substrate was covered by CVD graphene.

Raman spectroscopy characterization provides an insight of graphene properties in versatile way and nondestructive fashion. Raman measurements allow, amongst other, ascertaining the quality of the samples (quality of growth and transfer in our case). Further detail of interpretation of Raman spectra can found in Ref. 33. Here, we only focus on the basic operation and measurements in Raman spectroscopy. In brief, the so-called G–mode spectrum and 2D-mode spectrum are used to characterize graphene (single or multi layers) in Raman spectroscopy. G–mode is 2D–mode originate from in-plane vibrational mode of graphene. The peak intensity ratio I_{2D}/I_G indicates the layer number of graphene. A single layer graphene yields at least a ratio more than 1.5 [33]. Here, Raman spectroscopy Xplora One was used to probe the sample at different spots. The intensity ratio of the G mode to the 2D mode in Raman spectra in Fig. 5.11 confirm that monolayer graphene was grown.

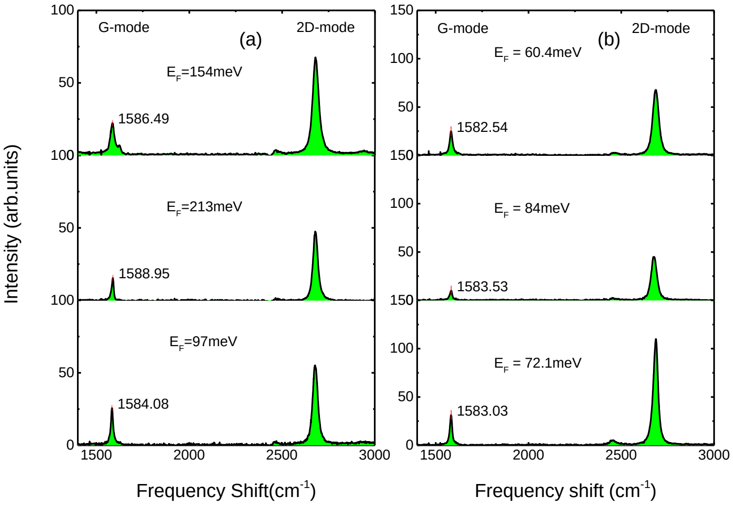

Fig. 5.11 Raman Spectra of graphene sample and the Fermi energy associated. Each Raman spectrum is measured in one spot of the substrate side with graphene. The frequency positions of G-mode peaks are also shown. The difference in intensities is due to the difference of the laser pump power used in Raman spectroscopy. The unit of the frequency shift of the figures is cm^{-1}. (a). Raman spectra of sample A before annealing. (b). Raman spectra of sample A after annealing.

From Raman spectra, the Fermi energy of the samples can be also retrieved. The Fermi energy, E_F, of the grown sample is calculated from the G-mode peak position, ω_G, using the formula ω_G (cm^{-1}) = 1580 (cm^{-1}) + $|E_F|$ (eV) × 42 (cm^{-1}eV^{-1}) [34].

5.3.3 *Comparison between conventional THz TDS and THz-PPWG-TDS*

The measurements procedures in THz-PPWG-TDS has been already described previously. Here we use the second experimental setup which has a different parabolic mirror focal length. Characterization measurements of each graphene sample were performed in two steps. First, we characterize the samples using PPWG and conventional THz-TDS systems. Then, we annealed the sample at 445 K under a pressure of ~10^{-7} Torr in a cryostat for one hour [28, 35]followed by cooling for about four hours in the vacuum chamber, after which we immediately measured the sample again with both systems. The purpose of sample annealing is to obtain a pristine graphene which is free of impurities.

Before embarking in detailed discussion, we first compare spectra taken by conventional transmission THz- TDS with those taken in TE mode of THz-PPWG-TDS in Fig. 5.12. The sample characterized in this Fig. is the graphene after annealing (almost pure graphene). The comparison of both spectrum already indicates that it is challenging to measure the optical properties of pristine graphene in conventional method. The spectrum of the reference MgO and graphene/MgO almost overlap over the entire range of frequency. In contrast, an obvious amplitude difference occurs in TE mode of PPWG spectrum.

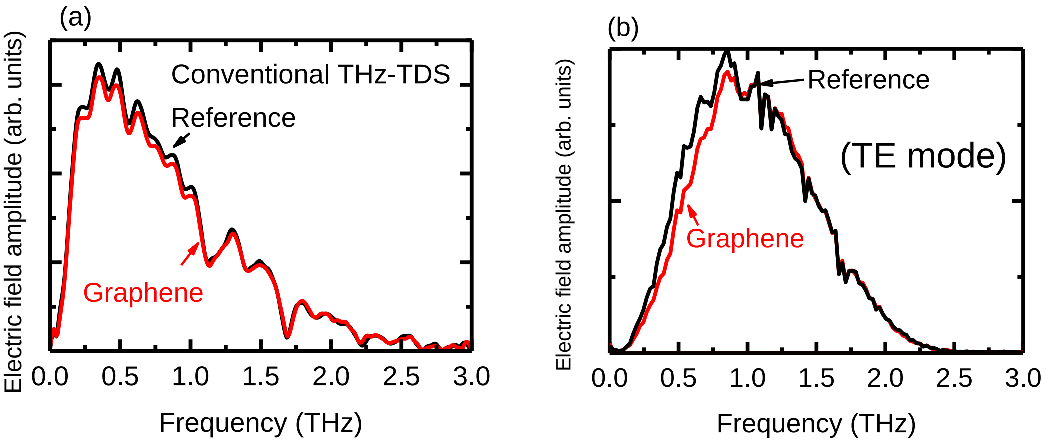

Fig. 5.12 Comparison of spectra measured using (a) conventional THz- TDS and (b) by THz-PPWG-TDS in TE mode.

Now, I emphasize here one of the main finding of this work. To further confirm the advantage of PPWG, Fig. 5.13 shows the transmittance spectra for Sample A taken by means of both methods. In the case of conventional THz-TDS, the spectra are nearly flat over the entire frequency range (0.1 THz-1.8 THz) for the sample before and after annealing, with transmittance ~95% and ~98%, respectively. It should be noted that each transmission data collected using conventional THz-TDS was averaged over 20 spectra. In the case of -THz-PPWG-TDS, the transmittance clearly shows some frequency dependence. The transmittance value is ~60% (~70%) before (after) annealing in the low-frequency region while it increases to ~95% at the high-frequency end of the spectra.

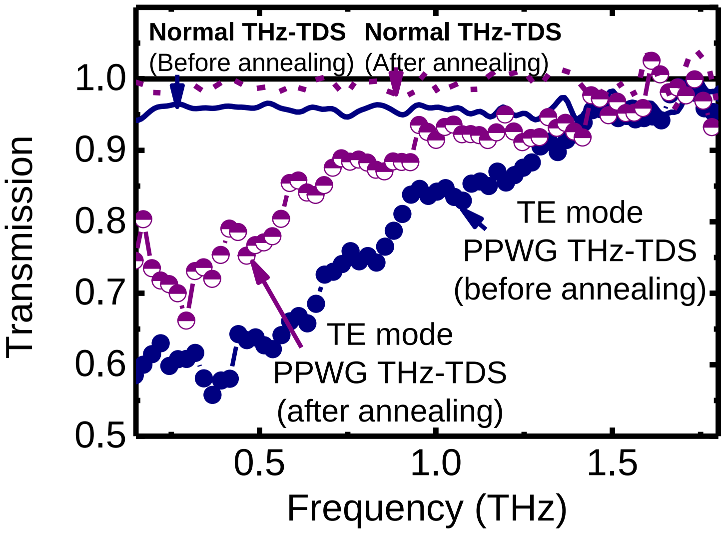

Fig. 5.13 Comparison of frequency dependent transmission data taken with normal-incidence transmission THz-TDS and THz- PPWG-TDS in TE mode. (Sample A before and after annealing). The upper quasi-flat curves are averaged transmittance data taken with THz-TDS. The blue solid curve is for non-annealed graphene on MgO and the purple dashed curve is for annealed graphene on MgO. The same sample is analyzed with TE waveguide mode, leading to a frequency-dependent transmittance represented by blue solid circles for Sample A before annealing and by purple solid circles for after annealing.

The spectrum of TE–mode of PPWG (Fig. 5.12) suggests from the absence of interferences that single-mode propagation is realized. Then, in the frequency (f) domain, the complex-valued transmission coefficient (Eq. (3.57) is simplified to:

$$T(f) = \frac{E_{\mathrm{MgO/Graphene/MgO}}}{E_{\mathrm{MgO/MgO}}} = |T|e^{i\Delta\varphi} \approx e^{i\Delta\gamma L}, \tag{5.14}$$

where $E_{\mathrm{MgO/Gr/MgO}}$ is the complex frequency-dependent electric field detected through the waveguide with graphene, $E_{\mathrm{MgO/MgO}}$ is the electric field detected through the waveguide without graphene, $\Delta\varphi$ is the experimental phase difference between the reference and the sample pulses, $\gamma \equiv \Delta\beta - j\Delta\alpha$, β is the propagation constant of the PPWG mode under consideration (TE or TM mode), and α is the propagation loss. The length of the waveguide, L, is 10 mm. In Eq. (5.14), the coupling coefficient and the impedance matching are assumed to be the same for the reference and sample signal. Note that Eq. (5.14) works only for single-mode propagation, either in the TE mode or TM mode.

If the fundamental TE mode (TE_1) of the bare PPWG does not change much in the presence of graphene, a perturbation method [36] simplifies Eq.(5.14). In this case, the waveguide loss is expressed by the dissipation loss α which is:

$$\alpha = \frac{\sigma_S}{4P} \iint_S |E(x, y)|^2 \, dS, \tag{5.15}$$

where P is the power transmitted without graphene (reference side), E is the electric field in Eq. (3.19) and the integral is performed over the waveguide cross section. If W is the width of the PPWG, the power transmitted is:

$$P = \frac{W}{2} \int_0^d E_x H_y^* dx = \frac{W d \omega \mu \beta}{4k_x^2} A^2 \, . \tag{5.16}$$

After computing the integral in Eq. (5.15), we have:

$$\alpha \approx 2\pi f \mu \sigma_S / 2\beta \tag{5.17}$$

For a special case where the propagation constant β doesn't differ much from $2\pi f n_{MgO} \sqrt{\mu \varepsilon_0}$ (plate separation d >> λ_{THz} or the frequency cutoff is situated in the lower limit of the system frequency bandwidth, which is the actual case), the propagation loss is directly proportional to the conductivity: $\alpha \propto \sigma_S$. Then, the amplitude of transmission (Eq. 5.14) is $|T| \approx e^{-C.\sigma_S.L}$. From this expression, we see two important features of THz-PPWG-TDS. First, a longer waveguide yields exponentially stronger absorption and thus a higher sensitivity. Second, the transmission decreases exponentially with increasing sheet conductivity; thus, even a very small difference in conductivity can produce a substantial difference in transmission. These advantages of THz- PPWG-TDS are clearly demonstrated in Fig. 5.13.

From the perspective of mode propagation, we can consider the TE mode as a propagating plane wave bouncing between the waveguide plates with polarization parallel to the layer surface [37]. Due to the frequency cutoff of the TE_1 mode ($f_c \approx 0.06$ THz), the free-space THz pulse is reshaped when traveling through the waveguide, and with the phase and group velocities strongly frequency dependent. Lower-frequency components of the THz wave traverse the waveguide more slowly than higher-frequency components and hence experience a larger number of bounces. An increase in the number of bounces yields stronger absorption by the sample. Therefore, this dispersive nature of TE_1 mode provides a more efficient approach to the study of weakly conducting material. This fact is counterintuitive in THz spectroscopy since it is usually common to avoid such dispersion.

We also performed TM mode analysis of graphene in a PPWG. The two spectra of reference and sample (Fig. 5.14.) overlap each other over the entire frequency range. Namely, the system is not capable of separating the sample absorption of the THz wave from other sources of uncertainty (e.g., misalignment, SNR of the detector). In fact, in a real 2D material like graphene, the electrons are confined in the sample plane. Consequently, when an electric field perpendicular to the surface (TM mode) is applied to the sample, there is no current induced, and thus, there is no THz absorption. The conductivity is zero in that direction.

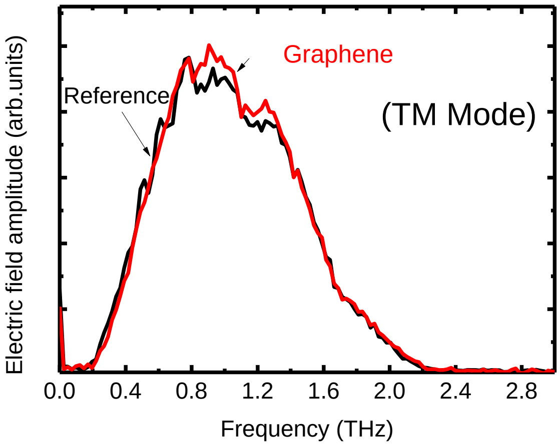

Fig. 5.14 Typical THz frequency domain spectra of Transverse magnetic mode of PPWG. The black curve is the THz spectrum of reference averaged over ten spectra. The red curve is the THz spectrum of sample also averaged over 10 spectra.

5.3.4 *Theory*

As shown in Fig. (5.15), graphene is made of carbon atoms arranged in honeycomb lattice. The energy band structure of graphene has been investigated extensively [38, 39] and we just adopt here the simplest treatment of electronic properties of graphene. The primitive vectors of the structure are $\boldsymbol{a_1} = a\,(1,0)$ and $\boldsymbol{a_2} = a\,(-1/2, \sqrt{3/2})$. The vectors which connect the nearest neighbor carbon are given by $\boldsymbol{l_1} = a\,(0,1/\sqrt{3})$, $\boldsymbol{l_2} = a\,(-\frac{1}{2}, -1/2\sqrt{3})$ and $\boldsymbol{l_3} = a\,(\frac{1}{2}, -1/2\sqrt{3})$. Therefore, the reciprocal lattice vectors are $\boldsymbol{a_1^*} = 2\pi/a\,(1,1/\sqrt{3})$ and $\boldsymbol{a_2^*} = 2\pi/a\,(0,2/\sqrt{3})$. In graphene physics, the most two important points of Brillouin zone are the corners K and K' located at $\mathbf{K} = 2\pi/a(-2/3,0)$ and $\mathbf{K'} = 2\pi/a(2/3,0)$.

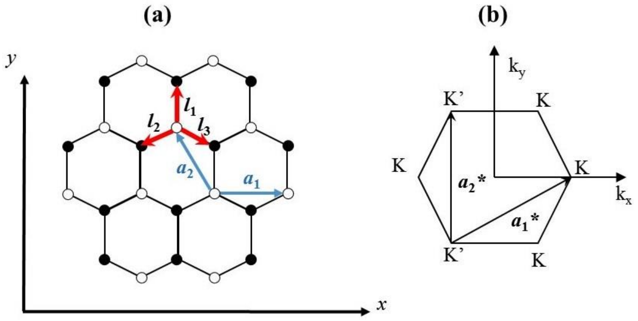

Fig. 5.15 schematic of (a) graphene lattice structure with the primitive vectors a_{i} (i = 1, 2)and the vectors l_{j} (j = 1, 2, 3) which connect the nearest neighbor;(b) The first Brillouin zone with the reciprocal lattice vector a_{i}^{*} (i = 1, 2)

In planar honeycomb carbon structure, three orbitals 2s, 2p$_x$ and 2p$_y$ hybridize into sp^2 orbital to constitute the σ-band [40] and the orbital 2p$_z$ form independently the π-band. Only the latter orbital plays role in the carrier transport of graphene. By applying tight binding method to the system with the atomic orbital of 2p$_z$, the energy dispersion is given by:

$$E_{\pm}(\mathbf{k}) = \pm|h(\mathbf{k})|. \tag{5.18}$$

with:

$$h(\mathbf{k}) = -t\sum_{s=1}^{3} e^{-i\mathbf{k}\boldsymbol{l}_s} \tag{5.19}$$

where t is the hopping integral and **k** is the wave vector [40]. At K and K' points, the energy is zero and the negative and positive energy bands intersect each other. Close to these points, the energy equation can be expanded to [40]:

$$E_{\pm}(\mathbf{K}+\mathbf{k}) = E_{\pm}(\mathbf{K}'+\mathbf{k}) \approx \pm\hbar v_F|\mathbf{k}|. \tag{5.20}$$

Here $v_F\ \approx 1.10^6\ \mathrm{m/s}$ is the Fermi velocity.

K and K' are known as Dirac point from the similarity of dispersion equation Eq. (5.20) to that of massless Fermions in Dirac – Weyl equation.

Microscopically, the optical response of graphene in the THz range is mainly dominated by intraband free-carrier absorption, describable with the Drude formula [41–44]:

$$\sigma_S = \frac{iD}{(2\pi f + i\Gamma)}, \tag{5.21}$$

where Γ is the scattering rate and the Drude weight D is given by [41-44]

$$D = \frac{e^2 k_{\mathrm{B}} T}{\pi \hbar^2} \ln\left(2\cosh\left(\frac{E_F}{2k_{\mathrm{B}}T}\right)\right). \tag{5.22}$$

Here, e is the electronic charge, $\hbar$ is the reduced Planck constant, k_{B} is the Boltzmann constant, and T is the temperature. Therefore, the Fermi energy can be also extracted from the experimental conductivity of graphene. The carrier density and Fermi energy are related by [41-44]

$$E_F = \hbar v_F \sqrt{\pi N}. \tag{5.23}$$

Since the conductivity of graphene is Drude – like, the DC conductivity and the mobility can also be calculated.

5.3.5 *Conductivity results*

In contrast to the multimode propagation fitting in the gold nanostructures case, the conductivity of graphene is calculated directly from the dispersion equation Eq. (3.44) – (3.45). Fig. 5.16 shows the real and imaginary parts of the sheet conductivity for Sample A and B before and after annealing, together with fitting curves using the Drude formula. The conductivity is expressed in units of σ_0, where $\sigma_0 = \pi e^2/2h \approx 6.1 \times 10^{-5}$ S is the universal interband conductivity of graphene [24, 26, 27]. From the relation between E_F and the carrier concentration N [27], we found that $N = 1.07 \times 10^{12}$ cm^{-2} for Sample A and $N = 1.01 \times 10^{12}$ cm^{-2} for Sample B before annealing. The scattering rate obtained were $\Gamma = 3.39\ 10^{12}$ s^{-1} for Sample A and $\Gamma = 4.2\ 10^{12}$ s^{-1} for Sample B. These values are comparable with the values reported for CVD-grown graphene on different substrates [27, 45–47]

Table 5.3 shows the fitting parameters of the Drude model extracted from the experimental data for both Sample A and Sample B: the DC conductivity(S), scattering rate, Γ (s^{-1}), carrier density, N (cm^{-2}), Fermi Energy, E_{F} (meV) and the mobility (cm-^{2}V^{-1}s^{-1}). It has been experimentally observed that adsorption of water and oxygen molecules dramatically changes the electromagnetic properties of graphene [45, 48]. In fact, transport measurements [49] revealed that charge transfer occurs between adsorbed molecules and graphene. Vacuum annealing described in the experimental section removes these adsorbed molecules [50, 51] and additionally reduces PMMA residues and other impurities. It can indeed be seen in Table 5.4 that the annealing process reduces the carrier density ($N = 2.3 \times 10^{11}$ cm^{-2} for Sample A and $N = 2.2 \times 10^{11}$ cm^{-2} for Sample B). These small numbers of densities were determined by the THz-PPWG-TDS method while normal THz-TDS could not detect any THz absorption after annealing, as also shown in Table 5.3 for Sample A.

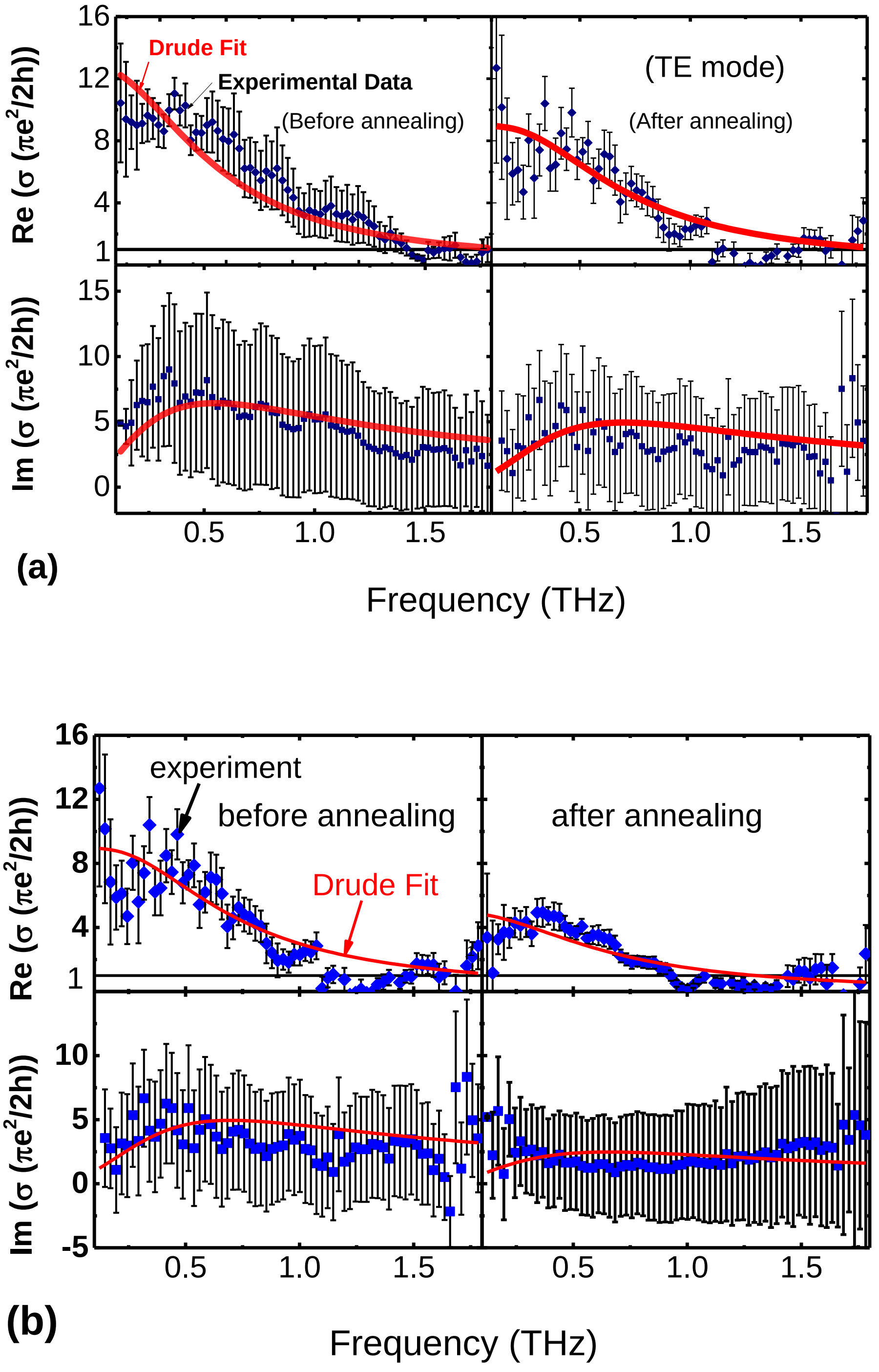

Fig. 5.16 Experimental data of graphene conductivity and the Drude model fitting curves normalized by the universal conductivity of graphene ($\pi e^2/2h$). (a) Results for Sample A and (b) results for Sample B. The error bars indicate the standard deviation of the experimental data. The red curve is the theoretical Drude fit while the frequency range used for the fitting process was set to be 0.1-1.8 THz

Table 5.3 Drude fitting parameters extracted for Samples A and B before and after annealing using parallel-plate waveguides (PPWG) and conventional THz-TDS.

	Sample A			Sample B	
	Before annealing		After annealing	Before annealing	After annealing
	PPWG	THz-TDS	PPWG	PPWG	PPWG
σ_0 (10^{-4}S)	7.8	8.65	3.67	7.1	3.62
Γ (10^{12} s^{-1})	3.39	5.84	2.6	4.2	4.08
N (10^{12} cm^{-2})	1.07	1.94	0.23	1.01	0.22
E_F (meV)	133	179	62.1	129	61
μ(cm-^{2}V^{-1}s^{-1})	3750	1972	8105	4393	10200

5.3.6 *Conclusion*

In summary, we have demonstrated that parallel-plate waveguide based THz spectroscopy is a powerful technique for characterizing 2D materials, using graphene as an example. This method has particular advantages at low frequencies due to longer interaction paths between the propagating THz wave and the 2D material, leading to a better sensitivity than the conventional THz spectroscopy techniques. Using this waveguide approach, we observed a substantial (~30%) change in transmission even for a sheet carrier density as low as 2×10^{11} cm^{-2} whereas conventional normal-incidence transmission THz spectroscopy did not produce any signal for this low density.

5.4 MAGNETIC RESONANCE OF METAMATERIALS

5.4.1 *Introduction*

Electromagnetic properties of metamaterials have been intensively studied in the terahertz (THz) regime [52–54]. Their exotic electromagnetic response has enabled novel applications, e.g., tunable THz modulators [55], THz device sensors [56], THz quarter wave plates [57, 58]etc. Generally, metamaterials are based on split ring resonators (SRR) arranged in periodic structures [59]. These structures respond electrically and magnetically to incident electromagnetic field resulting in electric, magnetic or magneto-electric resonance with respect to the direction of the THz wave propagation. Various designs have been proposed to suppress the magneto-electric coupling of the structure, in order to further control the behavior of the metamaterials, and to facilitate a more precise characterization of their electromagnetic properties [60]. While the electric coupling mechanism is well understood using a normal THz incidence beam geometry, experimental study of magnetic response have met some practical limitations [55, 61]. In conventional THz-TDS, the electric and magnetic fields lie in the plane of the surface structure, thus resulting in a negligible coupling to the magnetic excitation field.

Introducing an oblique angle of incidence for the THz wave remedies this issue [62]. The samples are rotated about an axis parallel to the SRR surface, and the maximum magnetic field amplitude is expected at a rotation angle of 90°. However, for expediency, the experiments were usually limited by the incident angle of 45°. Another possibility to study the magnetic resonance could be by using the THz-TDS in attenuated total reflection configuration [63]. In such a measurement, the THz incident beam is coupled to the sample using a plastic prism [64]. The leaking evanescent waves from the prism couple to a planar metamaterials at certain angles and can induce electric or magnetic resonances. However, the experimental implementation here suffers from limited injection angles. Additionally, evanescent waves have a very weak free space coupling, further reducing the interaction strength between the electromagnetic radiation and the samples.

While the above-mentioned methods to study the THz properties of metamaterials have been used widely in the past, the waveguide-based techniques have garnered less attention. Previously, we found that the PPWG geometry with ultrathin conductive films located halfway between the plates provides an optimized interaction between the electromagnetic wave and the sample. Here, we apply this technique to study the magnetic response of the ultrathin symmetric electric SRRs (eSRRs) that have pure electrical response in the case of normal incidence of the THz beam. Thin metamaterial samples reside half way between the PPWG plates, where the intensity of the electromagnetic field is maximal. Unlike previous works for characterization of magnetic resonance of THz SRRs, we take advantage of: (i) the well-defined directions of the electric and magnetic fields in TM and TE) modes of PPWG; and (ii) multiple reflections inside the waveguide to enhance the coupling strength.

Here, we report on the experimental study of the electromagnetic response of eSRRs in TM and TE modes of a PPWG. Due to the particular profile of PPWG TE mode [37, 65], we have observed a strong magnetic resonance of eSRRs in far field measurements. This magnetic resonance is strongly distinct from the electric resonance. Simulations has been carried out to interpret the experimental results.

5.4.2 *Experiment*

We employ the same THz-PPWG-TDS setup as in the graphene investigation described above. However, the substrates in this work were changed to high resistive silicon having a THz refractive index of 3.45 at 1THz and negligible extinction coefficient. The dimensions of the Si substrate are identical to the dimension of MgO for gold and graphene. Fig. 5.17 shows a sketch of PPWG geometry and metamaterials studied here.

Our metamaterials have the form of a square array of eSRRs spaced with 70 μm periodicity, manufactured by a standard photolithography process. A unit cell of eSRR is composed of two rectangular SRR made of 80 nm thick gold, sharing a middle arm at the center. One eSRR has a side length of 50 μm, line width of 6 μm, and a gap of 6 μm. This design is typical for the use in THz frequency range [66]. Fig. 5.17 (b) shows the dimensions of the structure as well as the lattice parameters. For convenience, two samples with different eSRRs orientations were fabricated.

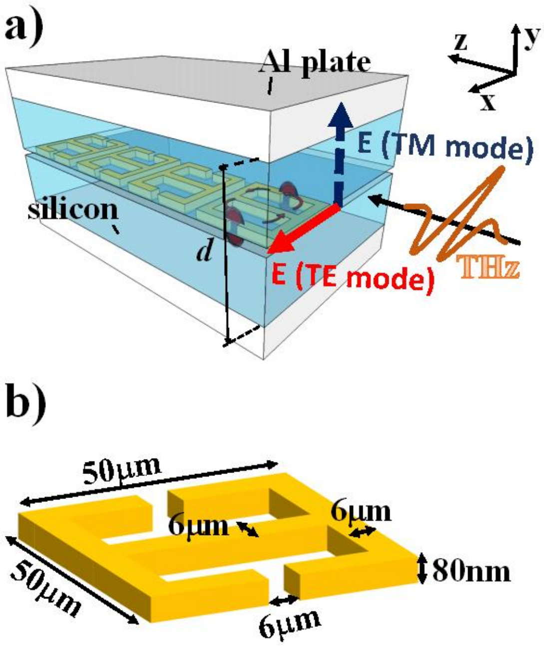

Fig. 5.17 (a) Geometry of thin metamaterials in parallel plate waveguide. The electric field for TM and TE modes excitation are shown. (b) Unit cell dimension of electric split ring resonator. The metal is gold ultrathin film having a thickness 80 nm. The periodicity of the metamaterial is 70 μm

Six sets of experimental measurements were performed in this work: two with standard normal incidence transmission THz TDS, and four with THz-PPWG-TDS. In standard THz TDS experiments, the first and the second measurements were made with the electric field of the incoming THz beam parallel and perpendicular to the gap-bearing sides of the eSRRs, respectively. The complex-valued THz transmission coefficients in frequency domain were obtained by dividing the complex-valued electric field amplitudes detected through the sample (substrates and metamaterials) by the electric field of the reference signal (substrate) as explained in chapter. 2. In the waveguide experiments, the four measurements included: two measurements in TM mode (electric field parallel and then perpendicular to the gap sides), and two measurements in TE mode. The THz wave transmitted through PPWG with metamaterials was the sample signal, and the wave transmitted through the PPWG without metamaterials was our reference. Time domain THz pulses with 2048 points were recorded for both the standard TDS and the PPWG TDS experiments. However, the multiple-reflection pulses in a standard THz TDS measurement were eliminated by zero padding the temporal signal from the temporal position of the first reflection.

In this work, we have also simulated the thin film metamaterials response with a finite difference time domain (FDTD) – based on commercial software Lumerical. The first simulation was performed with normal beam incidence, and the second simulation corresponded to the PPWG geometry similar to Fig. 5.18 (a). In PPWG experiments, the plate separation is around 1 mm, the gold thickness is 80 nm, and the propagation length is 10 mm. As result, the scaling between the gold thickness and the cross-section of the entire waveguide amounts to four order of magnitude, which required a substantial memory and time resources. Therefore, the thickness t was increased to 4 μm, at which the condition that $t << \lambda_{\mathrm{THz}}$, where λ_{THz} is a THz wavelength, is still satisfied. One column of four unit cells was included in the PPWG simulation with periodic conditions in the x-axis (Fig. 5.17 (a)). The source was set to excite fundamental mode of the waveguide. Two orientations of the SRRs were simulated and compared with the experimental data.

5.4.3 *Results and discussion*

The response of the metamaterials was first studied in normal-incidence THz TDS experiment. The electric and magnetic fields were parallel to the metamaterials surface plane in both measurements. Fig. 5.18 displays the transmission amplitude and the corresponding phases (angle of the transmission) with electric field parallel and perpendicular to the resonator gap bearing side. The propagation of the electromagnetic field is shown in the Fig. insets. The black curves are the experimental data, which agree well with the simulations results (blue curve). The spectral features in the transmission curves are as expected for the metamaterials of such designs, measured at normal incidence [61]. The N-shaped phases of the complex transmission coefficients are typical for the Lorentzian-type resonances. All spectral dips in Fig. 5.18 are the resonances related to the coupling of incident electric field to the eSRRs. The first resonance appearing at 0.44 THz in Fig. 5.18 is the fundamental LC resonance of the equivalent LC oscillator of the structure [52, 60, 61, 67]. The second resonance at 1.66 THz in Fig. 5.18(a), as well as the single broad resonance at 0.91 THz in Fig. 5.18(b), originate from the electric resonance due to half-wave resonance of the SRR sides [68, 69]. To further understand the resonance mechanisms, the surface current densities were calculated for the three observed resonances. The surface current densities shown in Fig. 5.18(c) and (d) are associated with the resonance in Fig. 5.18(a). The arrows inside indicate the current direction. Here, the magnetic field is parallel to the plane of metamaterials with the direction of propagation normal to it. As a result, the magnetic resonance should not occur. Furthermore, the design of eSRRs eliminates a far field coupling of the magnetic resonance for the following reason. From Fig. 5.18(c), the first resonance, in case of the electric field parallel to the eSRRs gap, arises from the circulating current with opposite directions in both parts of the structure. Therefore, the magnetic dipoles induced on both sides are also point in opposite directions, and these effects are observable solely with near field measurements [70]. The second resonance emerges from the current flowing in parallel in both arms of the eSRR as shown in Fig. 5.18(d). We have similar situation in case of Fig. 5.18(e) which corresponds to the resonance in Fig. 5.18(b). These half wave resonances are related to the plasmonic oscillations along the sides of the eSRRs [68, 69].

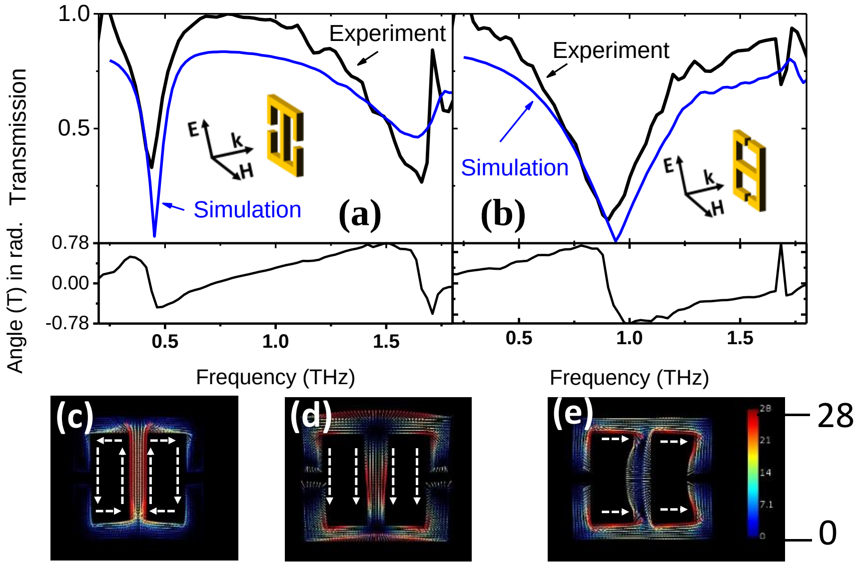

Fig. 5.18 Transmission amplitudes and corresponding angles in normal beam incident THz-TDS. The black lines are the experimental data and the blue lines are the simulation results. The beam direction and eSRRs orientations are shown in the figures. insets with: (a) the electric field parallel to the gap-bearing sides, (b) with the electric field perpendicular to the gap bearing sides; (c)- (d) Surface current densities simulated corresponding to the resonances Fig. 5.18.(a); (e) Surface current densities simulated corresponding to the resonance in Fig. 5.18. (b). The maximum of the intensity is shown in red color and the minimum of the intensity is shown in blue color. The white arrows indicate the current direction.

The experimental results displayed in Fig. 5.19(a) - (b) (black solid lines with black dots) were obtained with the PPWG excited in TE mode. The corresponding simulation results are shown by the blue curves. Here, the electric field component at the PPWG center lies in the eSRRs surface plane, while the magnetic component is normal to that plane.

When the electric field is parallel to the gap (Fig. 5.19(a)), two resonances are observed in the experiment and the simulation. The first resonance appears at the frequency around $f_1 = 0.3$ THz, followed by some small oscillations. A second resonance appears at a frequency around $f_2 = 0.6$ THz. According to the simulations studies performed at infrared frequencies[23] the first resonance could be assigned to the coupling of an incident electric field to the eSRRs. In short, similar to the normal incidence case, the electric field drives currents in opposite directions forming a so-called “antibonding mode” [71] from which the electric resonance originates. Following the same logic, the second resonance might be a magnetic resonance due to a circulating current along the eSRR arms induced by the external field. It should be noticed that symmetry of the system eliminates the cross coupling and the electric and magnetic resonances should occur at different frequencies. In other words, the eSRRs should not exhibit bianisotropic properties [57]. However, care must be taken here for several reasons. First, we have seen in normal-incidence THz measurements above that the dipole resonance can be excited with electric field perpendicular to the gap sides of SRRs. Second, far field measurements cannot distinguish unambiguously the electric or magnetic resonances, without retrieving the effective permittivity and effective permeability of the metamaterials.

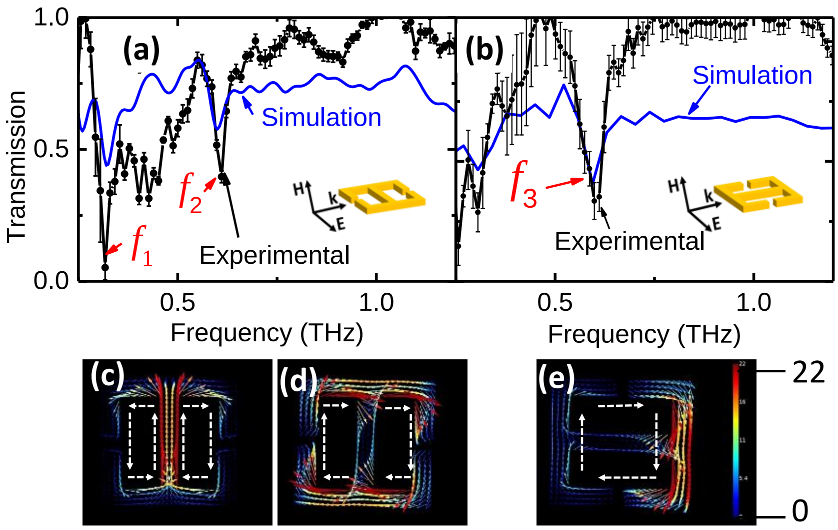

Fig. 5.19 Transmission amplitude of metamaterials inside PPWG in TE mode with indicated resonance frequencies. The black dots connected with black solid lines are the experimental data and the blue lines are the simulation results for: (a) Electric field parallel to the gap sides; (b) Electric field parallel with the no-gap sides; (c)- (d) Surface current densities simulated corresponding to resonance f_1 and f_2; (e) Surface current densities simulated corresponding to resonance f_3. The maximum of the intensity is shown in red color and the minimum of the intensity is shown in blue color. The white arrows indicate the current direction.

In combination with the simulated transmission curve (Fig. 5.19(a)), the corresponding surface current densities are also calculated as depicted in Fig. 5.19(c) – (d). For the resonance at f_1, current circulating in opposite directions takes place within the SRRs. This mechanism is the same as that of normal incident (Fig. 5.19(c)) beam in which the middle arm acts as wire and the gaps are the capacitive elements. The resonance frequency is red shifted due to the effective medium permittivity for the capacitance since the metamaterials inside the PPWG are sandwiched into two silicon substrates. In contrast, in the case of the normal-incidence THz beam measurements, the metamaterials are located between air and silicon substrate. To further confirm this observation, we have simulated the response of the metamaterials in normal incidence where the eSRRs structures are embedded in silicon (see Fig. 5.20). Indeed, the electric resonance frequency redshifts from 0.44 THz to 0.35 THz as a result of such a modification of the dielectric environment.

More intriguing results can be deducted from the resonance at f_2. In fact, the resonance f_2 is located at the same frequency position as f_3 of the Fig. 5.19(b). By inspecting the current densities in Fig. 5.19(d) (for f_2) and Fig. 5.19(e) (for f_3), circulating current over the whole structure occurs irrespective of the shared middle arms. These circulating currents produce a magnetic field with the direction opposite to the incoming field. As a result, a strong magnetic coupling occurs [60]. When the electric field is parallel to the gap bearing side (Fig. 5.19(e)), there are no apparent electric modes. The dipole-type resonances with symmetric current polarizations in both arms perpendicular to the beam are not excited here. Based on the simulation results, we can, therefore, confirm that the pronounced resonances at frequency around 0.6 THz in both orientations of SRRs are the magnetic resonances. However, while the current density is equally shared by both arms in Fig. 5.19(d), there is asymmetric distribution in Fig. 5.19(e). This fact have been pointed out in a previous theoretical investigation [71]. This asymmetry in the opposite arms might result from the electric field orientation which can enhance or weaken the current depending on its direction.

The TM mode measurements have been also performed in the THz-PPWG-TDS configuration, and no significant resonance was observed in the transmission data in both orientations of the eSRRs (Fig. 5.21). In the TM mode of the PPWG, the electric field has a transverse component normal to the metamaterials surface plane, whereas the magnetic field is parallel to that plane. Here, we suppose that the energy of the propagating wave is carried by the fundamental TEM mode in which the longitudinal electric field vanishes. As a result, neither electric nor magnetic field coupling to the SRRs was expected.

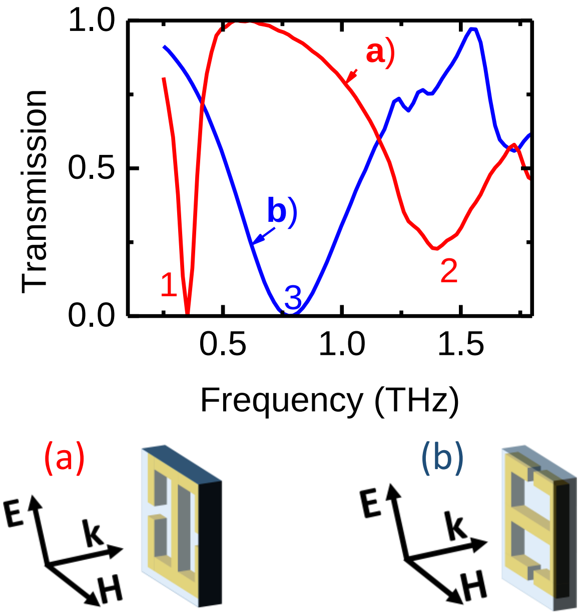

Fig. 5.20 Simulated transmission curve of metamaterials embedded in silicon substrates in conventional THz-TDS. (a) Simulation of the transmitted THz radiation when the electric field is parallel to the gap sides. The first frequency numbered 1 in the red curve is f = 0.35THz. The second frequency numbered 2 in red curve is f = 1.3 THz. (b) Simulation of the transmitted THz radiation when the electric field is perpendicular to the gap sides. The frequency numbered 3 in blue curve is f = 0.78 THz.

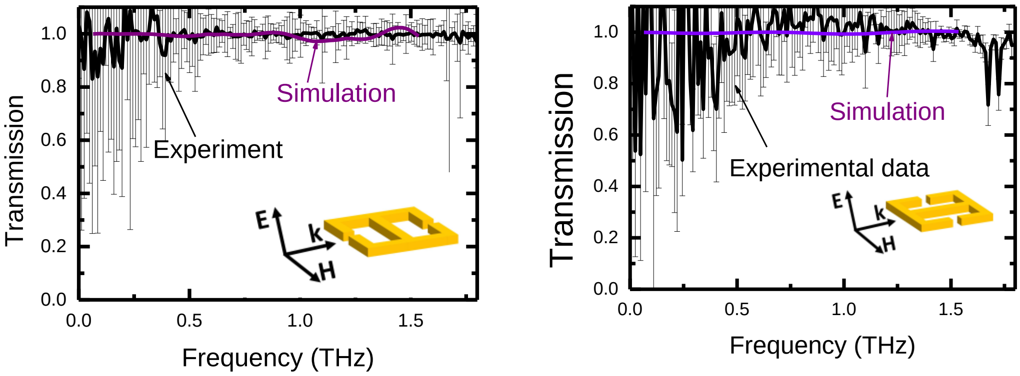

Fig. 5.21 TM mode measurement of metamaterials. The error bars in the figures shows that the data measured in TM mode are very noisy, in particular at the lower frequency range (0.1-1THz).

5.4.4 *Conclusion*

In summary, we have investigated the electromagnetic responses of electric SRRs in parallel incidence using PPWG and found strong magnetic coupling of the incoming THz wave with single layer planar metamaterials in TE mode. When the electric field was parallel to the gap bearing sides of the eSRRs, one electric resonance and one magnetic resonance were distinctly observed. On the other hand, only the magnetic resonance is excited when the electric field is perpendicular to the gap bearing sides. The location of the magnetic resonance was independent of the eSRRs orientation. The particular electric and magnetic field distribution of the fundamental TE1 mode and the location of the metamaterials halfway between the PPWG plates optimized the interaction between the structure and the THz wave. Simulation of the surface charge densities have confirmed our observation and have further explained the resonance mechanism of eSRRs in a PPWG.

5.5 GENERAL CONCLUSION

We conclude this chapter by summarizing our three fundamentals findings during the entire period of this work. The two first experiments were related to the evaluation of basic electronic properties of two-dimensional materials and the last experiment was concerning one important domain of THz devices which is the metamaterials.

The first results we obtained with gold ultrathin films were a demonstration of the PPWG performance to characterize nanostructures metallic films. In particular, we reported that the TE mode provides better sensitivity than the TM mode. Our results are comparable with the reported values [10]. Here, the use of PPWG to investigate on the thin conductive film properties is the new aspect of this work. Furthermore, we have found a new opportunity of using PPWG TE mode in addition to its capability in THz communication and THz sensing.

Based on the gold thin films results, we also probed the electronic properties of atomic-thick layer using PPWG TE mode. To the best of our knowledge, this work was also the first investigation on graphene by utilizing PPWG. While the standard and THz-PPWG-TDS provided nearly the same optical parameters for non-annealed samples, only the PPWG approach succeeded to characterize the low conductive annealed samples, as shown Fig. 5.13. Compared to the standard method, the THz-PPWG-TDS provide much better sensitivity (30% absorption for annealed samples), and then provides a very good signal to noise ratio. This part of the work is essential for future investigation of any atomic-thick layers in THz since most of those materials are extremely low conductive.

Finally, we studied the coupling of magnetic excitation field to the THz metamaterials. Nowadays, research on the magnetic resonance of THz metamaterials is still a burgeoning fields. Here, we found that PPWG offered an alternative way to overcome some of the practical limitations in such investigations. Here, a strong magnetic resonance was revealed by making use of the PPWG TE mode.

REFERENCES:

[1] A. K. Sarychev and V. M. Shalaev, “Electrodynamics of Metamaterials,” World Scientific, 2007.

[2] M. Dressel, G. Gruener, and G. F. Bertsch, “Electrodynamics of Solids: Optical Properties of Electrons in Matter,” *Am. J. Phys.*, vol. 70, no. 12, p. 1269, 2002.

[3] D. R. Lide, “CRC Handbook of Chemistry and Physics (95th edition),” CRC, 2005.

[4] N. Laman, S. S. Harsha, D. Grischkowsky, and J. S. Melinger, “High-resolution waveguide THz spectroscopy of biological molecules.,” *Biophys. J.*, vol. 94, no. 3, pp. 1010–1020, 2008.

[5] A. Thoman, A. Kern, H. Helm, and M. Walther, “Nanostructured gold films as broadband terahertz antireflection coatings,” *Phys. Rev. B - Condens. Matter Mater. Phys.*, vol. 77, no. 19, pp. 1–9, 2008.

[6] A. Sarychev, D. Bergman, and Y. Yagil, “Theory of the optical and microwave properties of metal-dielectric films,” *Phys. Rev. B*, vol. 51, no. 8, pp. 5366–5385, 1995.

[7] P. F. Henning, C. C. Homes, S. Maslov, G. L. Carr, D. N. Basov, B. Nikolić, and M. Strongin, “Infrared Studies of the Onset of Conductivity in Ultrathin Pb Films,” *Phys. Rev. Lett.*, vol. 83, no. 23, pp. 4880–4883, 1999.

[8] Y. Yagil, P. Gadenne, C. Julien, and G. Deutscher, “Optical properties of thin semicontinuous gold films over a wavelength range of 2.5 to 500 μm,” *Phys. Rev. B*, vol. 46, no. 4, pp. 2503–2511, 1992.

[9] P. Keblinski and F. Cleri, “Contact resistance in percolating networks,” *Phys. Rev. B - Condens. Matter Mater. Phys.*, vol. 69, no. 18, pp. 1–4, 2004.

[10] M. Walther, D. G. Cooke, C. Sherstan, M. Hajar, M. R. Freeman, and F. A. Hegmann, “Terahertz conductivity of thin gold films at the metal-insulator percolation transition,” *Phys. Rev. B - Condens. Matter Mater. Phys.*, vol. 76, no. 12, pp. 1–9, 2007.

[11] N. Laman and D. Grischkowsky, “Terahertz conductivity of thin metal films,” *Appl. Phys. Lett.*, vol. 93, pp. 1–3, 2008.

[12] N. W. Ashcroft, N. D. Mermin, “SolidStatePhysics,” Thomson Learning, 1976.

[13] A. J. Gatesman, R. H. Giles, and J. Waldman, “High-precision reflectometer for submillimeter wavelengths,” *J. Opt. Soc. Am. B*, vol. 12, no. 2, p. 212, 1995.

[14] N. Smith, “Classical generalization of the Drude formula for the optical conductivity,” *Phys. Rev. B*, vol. 64, no. 15, pp. 1–6, 2001.

[15] G. M. M. Turner, M. C. Beard, C. A. Schmuttenmaer, C. A. M.C. Beard, and J. Schmuttenmaer, “Carrier localization and cooling in dye-sensitized nanocrystalline

titanium dioxide," *J. Phys. Chem. B,* vol. 106, no. 45, pp. 11716–11719, 2002.

[16] F. A. Hegmann, D. G. Cooke, and M. Walther, "The Nature of Terahertz Conductivity in Nanomaterials," *Opt. Terahertz Sci. Technol.*, p. TuA1, 2007.

[17] T. Brandt, M. Hövel, B. Gompf, and M. Dressel, "Temperature- and frequency-dependent optical properties of ultrathin Au films," *Phys. Rev. B,* vol. 78, no. 20, p. 205409, 2008.

[18] J. Liu, R. Mendis, and D. M. Mittleman, "The transition from a TEM-like mode to a plasmonic mode in parallel-plate waveguides," *Appl. Phys. Lett.*, vol. 98, no. 23, pp. 128–130, 2011.

[19] R. Mendis, "Nature of subpicosecond terahertz pulse propagation in practical dielectric-filled parallel-plate waveguides.," *Opt. Lett.*, vol. 31, no. 17, pp. 2643–2645, 2006.

[20] K. S. Novoselov, A. K. Geim, S. V Morozov, D. Jiang, Y. Zhang, S. V Dubonos, I. V Grigorieva, A. A. Firsov, "Electric Field Effect in Atomically Thin Carbon Films," *Science* , vol. 306, no. 5696, pp. 666–669, 2004.

[21] C. R. Dean, a F. Young, I. Meric, C. Lee, L. Wang, S. Sorgenfrei, K. Watanabe, T. Taniguchi, P. Kim, K. L. Shepard, and J. Hone, "Boron nitride substrates for high-quality graphene electronics.," *Nat. Nanotechnol.*, vol. 5, no. 10, pp. 722–726, 2010.

[22] M. Chhowalla, H. S. Shin, G. Eda, L.-J. Li, K. P. Loh, and H. Zhang, "The chemistry of two-dimensional layered transition metal dichalcogenide nanosheets," *Nat. Chem.*, vol. 5, no. 4, pp. 263–275, 2013.

[23] K. F. Mak, C. Lee, J. Hone, J. Shan, and T. F. Heinz, "Atomically thin MoS2: A new direct-gap semiconductor," *Phys. Rev. Lett.*, vol. 105, no. 13, p. 136805, 2010.

[24] S. Lei, L. Ge, Z. Liu, S. Najmaei, G. Shi, G. You, J. Lou, R. Vajtai, and P. M. Ajayan, "Synthesis and photoresponse of Large GaSe Atomic Layers," *Nano Lett.*, vol. 13, no. 6, pp. 2777–2781, 2013.

[25] X. Ling, H. Wang, S. Huang, F. Xia, and M. S. Dresselhaus, "The renaissance of black phosphorus," *Proc. Natl. Acad. Sci.*, vol. 112, no. 15, pp. 4523–4530, 2015.

[26] P. U. Jepsen, D. G. Cooke, and M. Koch, "Terahertz spectroscopy and imaging - Modern techniques and applications," *Laser Photon. Rev.*, vol. 5, no. 1, pp. 124–166, 2011.

[27] J. Horng, C. F. Chen, B. Geng, C. Girit, Y. Zhang, Z. Hao, H. a. Bechtel, M. Martin, A. Zettl, M. F. Crommie, Y. R. Shen, and F. Wang, "Drude conductivity of Dirac fermions in graphene," *Phys. Rev. B - Condens. Matter Mater. Phys.*, vol. 83, no. 16, pp. 1–5, 2011.

[28] L. Ren, Q. Zhang, J. Yao, Z. Sun, R. Kaneko, Z. Yan, S. Nanot, Z. Jin, I. Kawayama, M. Tonouchi, J. M. Tour, and J. Kono, "Terahertz and infrared spectroscopy of gated large-

area graphene.," *Nano Lett.*, vol. 12, no. 7, pp. 3711–5, 2012.

[29] C. Qiu, W. Gao, R. Vajtai, P. Ajayan, J. Kono, and Q. Xu, "Efficient Modulation of 1.55 µm Radiation with Gated Graphene on a Silicon Micro-ring Resonator," *Nano Lett.*, vol. 14, no. 12, pp. 1–5, 2014.

[30] H. Li, Y. Anugrah, S. J. Koester, and M. Li, "Optical absorption in graphene integrated on silicon waveguides," *Appl. Phys. Lett.*, vol. 101, no. 11, p. 111110, 2012.

[31] M. Furchi, A. Urich, A. Pospischil, G. Lilley, K. Unterrainer, H. Detz, P. Klang, A. M. Andrews, W. Schrenk, G. Strasser, and T. Mueller, "Microcavity-Integrated Graphene Photodetector," *Nano Lett.*, vol. 12, no. 6, pp. 2773–2777, 2012.

[32] M. Engel, M. Steiner, A. Lombardo, A. C. Ferrari, H. V. Löhneysen, P. Avouris, and R. Krupke, "Light–matter interaction in a microcavity-controlled graphene transistor," *Nat. Commun.*, vol. 3, no. May, p. 906, 2012.

[33] A. C. Ferrari, "Raman spectroscopy of graphene and graphite: Disorder, electron-phonon coupling, doping and nonadiabatic effects," *Solid State Commun.*, vol. 143, no. 1–2, pp. 47–57, 2007.

[34] C.-F. Chen, C.-H. Park, B. W. Boudouris, J. Horng, B. Geng, C. Girit, A. Zettl, M. F. Crommie, R. A. Segalman, S. G. Louie, and F. Wang, "Controlling inelastic light scattering quantum pathways in graphene," *Nature*, vol. 471, no. 7340, pp. 617–620, 2011.

[35] P. Chiu, "Graphene Annealing : How Clean Can It Be ?," *Nano Lett.*, vol. 12, no. 1, pp. 414–419, 2012.

[36] R. E. Collin, "Field theory of guided waves (2nd edition)," Wiley - IEEE press, 1990..

[37] R. Mendis and D. M. Mittleman, "Investigation of the lowest-order TE mode of the parallel-plate metal waveguide for terahertz pulses," *2008 33rd Int. Conf. Infrared, Millim. Terahertz Waves*, vol. 26, no. 9, pp. 1–4, 2008.

[38] T. Ando, "The electronic properties of graphene and carbon nanotubes," *NPG Asia Mater.*, vol. 1, no. 1, pp. 17–21, 2009.

[39] A. H. Castro Neto, N. M. R. Peres, K. S. Novoselov, and A. K. Geim, "The electronic properties of graphene," *Rev. Mod. Phys.*, vol. 81, no. 1, pp. 109–162, 2009.

[40] P. R. Wallace, "the Band Theory of Graphite," *Phys. Rev.*, vol. 71, no. 9, pp. 622–634, 1947.

[41] N. H. Shon and T. Ando, "Quantum Transport in Two-Dimensional Graphite System," *J. Phys. Soc. Japan*, vol. 67, no. 7, pp. 2421–2429, 1998.

[42] Y. Zheng and T. Ando, "Hall conductivity of a two-dimensional graphite system," *Phys.*

Rev. B, vol. 65, no. 24, pp. 1–11, 2002.

[43] T. Ando, Y. Zheng, and H. Suzuura, “Dynamical Conductivity and Zero-Mode Anomaly in Honeycomb Lattices,” *J. Phys. Soc. Japan*, vol. 71, no. 5, pp. 1318–1324, 2002.

[44] N. M. R. Peres, F. Guinea, and A. H. C. Neto, “Electronic Properties of Disordered Two-Dimensional Carbon,” *Phys. Rev. B*, vol. 73, no. 12, p. 125411, 2005.

[45] L. Ren, Q. Zhang, J. Yao, Z. Sun, R. Kaneko, Z. Yan, S. Nanot, Z. Jin, I. Kawayama, M. Tonouchi, J. M. Tour, and J. Kono, “Terahertz and infrared spectroscopy of gated large-area graphene.,” *Nano Lett.*, vol. 12, no. 7, pp. 3711–5, Jul. 2012.

[46] C. Lee, J. Y. Kim, S. Bae, K. S. Kim, B. H. Hong, and E. J. Choi, “Optical response of large scale single layer graphene,” *Appl. Phys. Lett.*, vol. 98, no. 7, p. 071905, 2011.

[47] J. Y. Kim, C. Lee, S. Bae, K. S. Kim, B. H. Hong, and E. J. Choi, “Far-infrared study of substrate-effect on large scale graphene,” *Appl. Phys. Lett.*, vol. 98, no. 20, p. 201907, 2011.

[48] Y. Sano, I. Kawayama, M. Tabata, K. A Salek, H. Murakami, M. Wang, R. Vajtai, P. M. Ajayan, J. Kono, and M. Tonouchi, “Imaging molecular adsorption and desorption dynamics on graphene using terahertz emission spectroscopy.,” *Sci. Rep.*, vol. 4, p. 6046, 2014.

[49] F. Schedin, A K. Geim, S. V Morozov, E. W. Hill, P. Blake, M. I. Katsnelson, and K. S. Novoselov, “Detection of individual gas molecules adsorbed on graphene.,” *Nat. Mater.*, vol. 6, no. 9, pp. 652–655, 2007.

[50] L. G. Booshehri, C. H. Mielke, D. G. Rickel, S. A. Crooker, Q. Zhang, L. Ren, E. H. Hároz, A. Rustagi, C. J. Stanton, Z. Jin, Z. Sun, Z. Yan, J. M. Tour, and J. Kono, “Circular polarization dependent cyclotron resonance in large-area graphene in ultrahigh magnetic fields,” *Phys. Rev. B - Condens. Matter Mater. Phys.*, vol. 85, no. 20, pp. 1–8, 2012.

[51] Z. H. Ni, H. M. Wang, Z. Q. Luo, Y. Y. Wang, T. Yu, Y. H. Wu, and Z. X. Shen, “The effect of vacuum annealing on graphene,” *J. Raman Spectrosc.*, vol. 41, no. 5, pp. 479–483, 2009.

[52] X. Z. T.J. Yen, W.J. Padilla, N. Fang, D.C. Vier, D.R. Smith, J.B. Pendry, D.N. Basov, “Terahertz magnetic response from artificial materials,” *Science.*, vol. 303, no. 5663, pp. 1494–1496, 2004.

[53] W. J. Padilla, M. T. Aronsson, C. Highstrete, M. Lee, A. J. Taylor and R. D. Averitt, “Electrically resonant terahertz metamaterials: theoretical and experimental investigations,” *Phys. Rev. B - Condens. Matter Mater. Phys.*, vol. 75, no. 4, pp. 1–4, 2007.

[54] A. K. Azad, A. J. Taylor, E. Smirnova and J. F. O'Hara, "Characterization and analysis of terahertz metamaterials based on rectangular split-ring resonators," *Appl. Phys. Lett.*, vol. 92, no. 1, pp. 2008–2010, 2008.

[55] H.-T. Chen , W. J. Padilla, J. M. O. Zide, A. C. Gossard, A. J. Taylor and R. D. Averitt, "Active Terahertz metamaterial devices," *Nature*, vol. 444, no. 7119, pp. 579–600, 2006.

[56] T. Driscoll, G. O. Andreev, D. N. Basov, S. Palit, S. Y. Cho, N. M. Jokerst, and D. R. Smith, "Tuned permeability in terahertz split-ring resonators for devices and sensors," *Appl. Phys. Lett.*, vol. 91, no. 6, pp. 22–25, 2007.

[57] C. Debus and P. H. Bolivar, "Frequency selective surfaces for high-sensitivity terahertz sensors," *Appl. Phys. Lett.*, vol. 91, p. 184102, 2007.

[58] A. C. Strikwerda, K. Fan, H. Tao, D. V Pilon, X. Zhang, and R. D. Averitt, "Comparison of birefringent electric split-ring resonator and meanderline structures as quarter-wave plates at terahertz frequencies.," *Opt. Express*, vol. 17, no. 1, pp. 136–149, 2009.

[59] R. A. Shelby, "Experimental Verification of a Negative Index of Refraction," *Science*, vol. 77, no. 2001, pp. 77–79, 2014.

[60] W. J. Padilla, "Group theoretical description of artificial electromagnetic metamaterials.," *Opt. Express*, vol. 15, no. 4, pp. 1639–1646, 2007.

[61] W. J. Padilla, A. J. Taylor, C. Highstrete, M. Lee, and R. D. Averitt, "Dynamical electric and magnetic metamaterial response at terahertz frequencies," *Phys. Rev. Lett.*, vol. 96, p. 107401, 2066.

[62] T. F. Gundogdu, I. Tsiapa, a. Kostopoulos, G. Konstantinidis, N. Katsarakis, R. S. Penciu, M. Kafesaki, E. N. Economou, T. Koschny, and C. M. Soukoulis, "Experimental demonstration of negative magnetic permeability in the far-infrared frequency regime," *Appl. Phys. Lett.*, vol. 89, no. 8, pp. 1–3, 2006.

[63] Y. Minowa, M. Nagai, H. Tao, K. Fan, A. C. Strikwerda, X. Zhang, R. D. Averitt, and K. Tanaka, "Extremely thin metamaterial as slab waveguide at terahertz frequencies," *IEEE Trans. Terahertz Sci. Technol.*, vol. 1, no. 2, pp. 441–449, 2011.

[64] H. Hirori, K. Yamashita, M. Nagai, and K. Tanaka, "Attenuated Total Reflection Spectroscopy in Time Domain Using Terahertz Coherent Pulses," *Jpn. J. Appl. Phys.*, vol. 43, no. No. 10A, pp. L1287–L1289, 2004.

[65] R. Mendis and D. M. Mittleman, "Comparison of the lowest-order transverse-electric (TE_1) and transverse-magnetic (TEM) modes of the parallel-plate waveguide for terahertz pulse applications," *Opt. Express*, vol. 17, no. 17, p. 14839, 2009.

[66] C. M. Watts, X. Liu, and W. J. Padilla, "Metamaterial electromagnetic wave absorbers.," *Adv. Mater.*, vol. 24, no. 23, pp. OP98–120, OP181, 2012.

[67] J. B. Pendry, a. J. Holden, D. J. Robbins, and W. J. Stewart, “Magnetism from conductors and enhanced nonlinear phenomena,” *Trans. Microw. Theory Tech.*, vol. 47, no. 11, pp. 2075–2084, 1999.

[68] S. Linden, C. Enkrich, M. Wegener, J. Zhou, T. Koschny, and C. M. Soukoulis, “Magnetic Response of Metamaterials at 100 Terahertz — Supporting Online Material,” *Science*, vol. 306, no. 5700, pp. 1351–1353, 2004.

[69] N. Katsarakis, T. Koschny, M. Kafesaki, E. N. Economou, and C. M. Soukoulis, “Electric coupling to the magnetic resonance of split ring resonators,” *Appl. Phys. Lett.*, vol. 84, no. 15, pp. 2943–2945, 2004.

[70] N. Kumar, A. C. Strikwerda, K. Fan, X. Zhang, R. D. Averitt, P. C. M. Planken, and A. J. L. Adam, “THz near-field Faraday imaging in hybrid metamaterials.,” *Opt. Express*, vol. 20, no. 10, pp. 11277–87, 2012.

[71] R. S. Penciu, K. Aydin, M. Kafesaki, T. Koschny, E. Ozbay, E. N. Economou, and C. M. Soukoulis, “Multi-gap individual and coupled split-ring resonator structures.,” *Opt. Express*, vol. 16, no. 22, pp. 18131–18144, 2008.

Chapter 6. **CONCLUSIONS**

6.1 SUMMARY

Many new types of 2D - materials have emerged in recent years, including graphene, hexagonal boron nitride, transition-metal dichalcogenides, and black phosphorous. These atomically thin, layered materials host 2D electrons that respond to long-wavelength light in extraordinary manners, which can revolutionize optics and photonics in the terahertz (THz) frequency range. Unfortunately, their conductivities are low (due to either low densities or low mobility), making it challenging to probe their THz properties with conventional methods. Throughout this dissertation, new parallel plate waveguide – based THz-TDS technique for ultrathin or 2D - materials has been developed in detail. Our motivation was driven by some criterions, presented in the introduction, which are essential for a successful THz characterization. Each of these requirements has been addressed in this work, which resulted to simple, low cost and powerful method for the investigation of carrier dynamics in these ultrathin conductive materials.

First, we have investigated on theoretical framework of ultrathin conductive materials placed halfway between the waveguide plates. As result, we have provided the equations for parameters extraction which is the most important part of the analysis. In summary, two equations has been derived for transverse magnetic and transverse electric modes:

$$\sigma_S = \frac{i2\omega\epsilon}{k_x}\cot\left(\frac{k_x d}{2}\right) \tag{3.44}$$

$$\sigma_S = \frac{i2k_x}{\omega\mu}\cot\left(\frac{k_x d}{2}\right) \tag{3.45}$$

where σ_S is the complex valued surface or sheet conductivity of the sample under investigation. The wave vector k_x is related to the complex propagation constant of the PPWG containing thin film by: $k_x = \sqrt{\omega^2\epsilon\mu - (\beta + i\alpha)^2}$. These two equations represent the propagation of THz wave with symmetric electric field component which is parallel to the thin film surface plane (E_z and E_y for TM and TE mode, respectively). Only the symmetric modes contribute to the propagation constant and propagation loss of the THz waves traveling through PPWG containing thin conductive films. The dispersion equations above are related to the amplitude and the phase of the complex -valued THz wave propagation constant γ, or the propagation constant β and the propagation loss α. If single mode propagation is realized, the parameters β and α can be extracted easily from experimental data leading to a direct calculation of the optical conductivity σ_S. In contrast, if higher modes are excited in the waveguide, we have to use a multimodal analysis by means of Eq. (3.57). One generalized transmission function which included single mode or multimode propagation was derived to that purpose. Then we, defined an algorithm to properly extract the optical parameters. The algorithm we have developed here was coded in Matlab software using Global Optimization toolbox which compute the global solution of a function containing several minima and maxima. Therefore, we have satisfied the requirement which consist to develop a proper parameters extraction formalism in order to obtain relevant spectroscopic information of the sample.

After developing the theory, we have fabricated the THz-TDS experimental set-up used for different prototype of samples. A home-made transmission-type THz TDS system based on *p*-type InAs emitter and an LT – GaAs dipole antenna receiver was set. The emitter and the detector was illuminated by an ultrashort laser at a wavelength of 800 nm and 80MHz repletion rate from Ti: sapphire. Descriptions of the main component in the experimental setup were outlined in chapter 4 which included the THz emission mechanism of a *p*-type InAs and the detection mechanism of the LT – GaAs dipole antenna. We chose the InAs emitter to obtain any THz input beam polarization before the waveguide. A combination of wire grid polarizer was designed to detect horizontal and vertical polarization of the electric field since the dipole antenna detect only one polarization. The free space beam shaping consists of four parabolic mirrors. Then, we have design a PPWG which is mounted on a moving stage. We have shown that the PPWG device is very simple to manufacture and can be made of any ordinary metallic materials. We also established a protocol to collect experimental data. Therefore, we also accomplished one of the criterion that the system should be compatible with any standard system.

In the first experiment we have conducted, our approach has been validated by the study of gold nanostructure. Here, we have found that the location of the sample in the middle of the PPWG provides a stronger interaction for odd TE modes electric field. Consequently, TE-mode excitation gives results which are more sensitive to the dielectric properties of the thin film, and are therefore in better agreement with the expected behavior of this prototype thin film system. The purpose of this particular investigation on gold thin films was the demonstration of the capability of PPWG approach in THz spectroscopy.

For the second set of experiment, we investigated on the sensitivity of PPWG approach by comparing with conventional THz-TDS using graphene as a sample. Here, we have employed THz parallel-plate waveguides to study monolayer graphene with low carrier densities. We demonstrated that a carrier density of ~2 × 10^{11} cm^{-2}, which induces less than 1% absorption in conventional THz transmission spectroscopy, exhibits ~30% absorption in our waveguide geometry. The amount of absorption exponentially increases with both the sheet conductivity and the waveguide length. Therefore, the sensitivity of this waveguide system can be increased by simply increasing the length of the waveguide along which the THz wave propagates, which enables us to detect low-conductivity carriers in 2D materials. We think that this part of the work is the most important finding since it opens up a new way to further investigate on the electromagnetic properties of atomic-thick layers in THz. Most of those materials are extremely low conductive and PPWG offers an alternative to the standard THz spectroscopy method.

Finally, we investigated on the coupling of external magnetic field to the THz metamaterials by means of PPWG. As it has been shown in this work, the interaction of the electromagnetic field and the samples is optimized by placing the materials under analysis hallway between the waveguide plates. Here, we reported that a strong magnetic resonance was revealed by the PPWG TE mode. In conclusion, PPWG offered an alternative way to overcome some of the practical limitations on the investigations on magnetic resonance of THz metamaterials

6.2 FUTURE WORK

In the burgeoning field of 2D materials science, measurements methods are being sought for elucidating their electronic properties rapidly, non-destructively, and sensitively. We have shown that PPWG combined with THz-TDS is a powerful technique to study such materials. Our perspective is to extend the potential of our method to some newly available techniques. One of the possibilities we consider is a combination of PPWG with optical pump – THz probe spectroscopy system. The basic principle of the setup is presented in Fig. 1. Graphene is again a good example of application. In the optical and infrared region, the carrier dynamics of the graphene is dominated by interband transition [1]. The optical pump creates pairs electron – holes and the THz pulse can be used to investigate on carrier relaxation and recombination dynamics [2]. This approach could be even more powerful for any 2D semiconductors materials. We have the advantage of high sensitivity and time resolved spectroscopy.

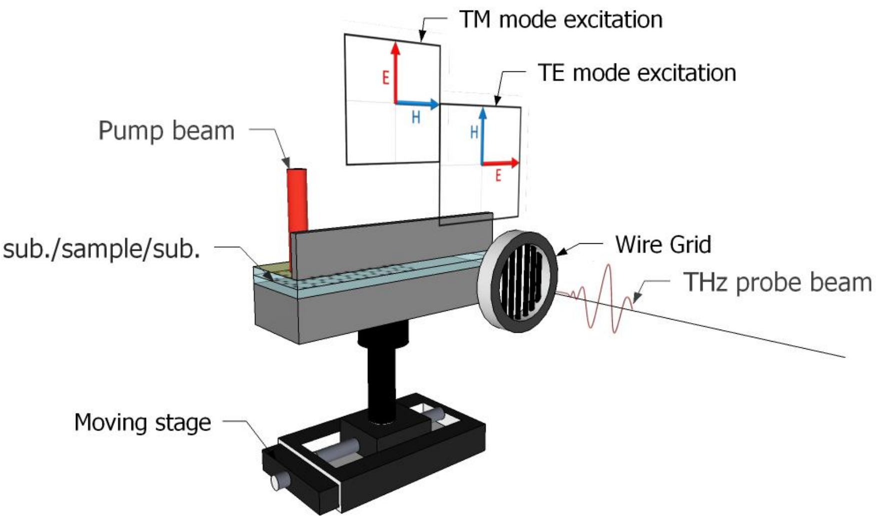

Fig. 6.1 Principle of optical pump THz probe PPWG system. The sample is still sandwiched between substrate but the top substrate is coated by an optically transparent materials (e.g., ITO). The top plate of the waveguide could be replace by a razor blade to block the THz probe to propagate along the surface of the top coated substrate. The operation to perform is the same as normal THz-PPWG-TDS reported in this work.

REFERENCES:

[1] L. Ren, Q. Zhang, J. Yao, Z. Sun, R. Kaneko, Z. Yan, S. Nanot, Z. Jin, I. Kawayama, M. Tonouchi, J. M. Tour, and J. Kono, “Terahertz and infrared spectroscopy of gated large-area graphene.,” *Nano Lett.*, vol. 12, no. 7, pp. 3711–5, 2012.

[2] P. A George, J. Strait, J. Dawlaty, S. Shivaraman, M. Chandrashekhar, F. Rana, and M. G. Spencer, “Ultrafast optical-pump terahertz-probe spectroscopy of the carrier relaxation and recombination dynamics in epitaxial graphene,” *Nano Lett.*, vol. 8, no. 12, pp. 17–20, 2008.

ACHIEVEMENTS

Papers:

1. Published: M. Razanoelina, R. Kinjo, K. Takayama, I. Kawayama, H. Murakami, D. M. Mittleman, and M. Tonouchi, "Parallel-Plate Waveguide Terahertz Time Domain Spectroscopy for Ultrathin Conductive Films," *J. Infrared Millim. Terahertz Waves* **36**(12), 1182-1194 (2015)
2. Accepted: M. Razanoelina, F. R. Bagsican, I. Kawayama, X. Zhang, L. Ma, H. Murakami, R. Vajtai, P. M. Ajayan, J. Kono and Masayoshi Tonouchi "Probing low-density carriers in a single atomic layer using terahertz parallel-plate waveguides" in *Optics Express*
3. Accepted: M. Razanoelina K. Serita, Eiki Matsuda, I. Kawayama, H. Murakami and M. Tonouchi. "THz metamaterials magnetic resonance studies by THz parallel plates waveguide" in *Applied Physics Express* (APEX)

International Conferences:

1. M. Razanoelina, R.Kinjo, K. Takayama, I. Kawayama, H. Murakami, Daniel M. Mittleman and M. Tonouchi, "Characterization of ultrathin conductive film by terahertz parallel plate waveguide", Teranano2015, (2015.7.2, Okinawa, Japan)
2. M. Razanoelina, R. Kinjo, K. Takayama, I. Kawayama, H. Murakami, and M. Tonouchi, "Parallel plate waveguide terahertz – time domain spectroscopy performance for gold nanosheet characterization", OTST15, (2015.3.8, San Diego, USA)
3. M. Razanoelina, R. Kinjo, K. Takayama, I. Kawayama, M. Murakami, M. Tonouchi, "Terahertz conductivity of gold nanosheet using parallel plate dielectric waveguide" , ISSS7 , 6PN-91, (2014.11.6, Matsue, Japan)
4. M. Razanoelina, I. Kawayama, H. Murakami, M. Tonouchi, "Characterization of terahertz parallel waveguide", Teranano2014, (2014.3.14, Osaka, Japan)

Local conferences in Japan:

1. M. Razanoelina, R. Kinjo, K. Takayama, I. Kawayama, H. Murakami, M. Tonouchi, "Terahertz waveguide for gold nanosheet analysis", The 18th SANKEN International Symposium, PA-56, (2014.12.10 , Osaka, Japan)
2. M. Razanoelina, R Kinjo, K. Takayama, I. Kawayama, H. Murakami, M. Tonouchi, "characterization of gold thin film by parallel plate waveguide terahertz time domain spectroscopy", The 18th JSAP autumn meeting, 19p-c6-13, (2014.9.19, Hokkaido, Japan)